Zur Homepage der Dissertation

Optoelectronic properties of size-selected silicon nanocrystals

Bei der Fakultät für Mathematik und Naturwissenschaften der Carl von Ossietzky Universität
Oldenburg zur Erlangung des Grades und Titels eines

Doktors der Naturwissenschaften (Dr. rer. nat.)

angenommene Dissertation

von Dipl.-Phys. Felix Voigt

geboren am 02.06.1973 in München.

Gutachter:
Prof. Dr. G. H. Bauer
Zweitgutachter:
Prof. Dr. F. Huisken
PD. Dr. habil. A. Kittel

Tag der Disputation: 21.10.05

Hiermit bestätige ich, dass ich die vorliegende Arbeit selbständig verfasst habe und nur die angegebenen Hilfsmittel verwendet habe.

Contents

Wissenschaftliche Forschung kann durch Förderung des kausalen Denkens und Überschauens den Aberglauben vermindern. Es ist gewiß, daß eine mit religiösem Gefühl verwandte Überzeugung von der Vernunft bzw. Begreiflichkeit der Welt aller feineren wissenschaftlichen Arbeit zugrunde liegt.

(Albert Einstein)

Die Wiegen von Wissenschaft und von Religion liegen im Staunen, im Suchen und Fragen, in der schöpferischen Neugier.

(in Anlehnung an Einstein und andere)

Wahrheit ist wie eine endlos sich windende Spirale, deren oberstes Ende wir nicht erkennen können.

(frei aus dem Kopf unter dem Einfluss bisheriger Erlebnisse und Worte anderer Menschen)

Abstract

Thin films of silicon nanocrystals (Si-nc) were produced by laser pyrolysis of SiH_4 and accumulated on various substrates. Layer growth, optical properties, charge transport, photoluminescence (PL) and electroluminescence (EL) were investigated on these porous layers.

A stick-ball model for layer growth of porous Si-nc films was developed and implemented by Monte-Carlo computer simulations. Therefrom a value $P(\infty) = 0.86$ for the bulk porosity of the layers was calculated in the limit of infinitely large volume.

Charge transport during layer growth could qualitatively be explained by percolative transport near interfaces and in the bulk respectively. The experimentally observed exponent $\overline{B_{exp}} \approx 1.5$ in the power law dependence of the electric conductance on the Si-nc layer areal density was fairly well reproduced by further Monte-Carlo simulations based on the stick ball model.

Current-voltage characteristics of oxidized Si-nc layers were reproduced by a model assuming tunnelling through oxide shells between adjacent Si-nc and from these fits the number of oxide barriers between the two contacts on the sample was determined. This number turned out to be a factor $1.5 \ldots 12$ larger than the calculated number of Si-nc in a straight line between the contacts, which can be attributed to the existence of percolation paths. Experimentally severe instabilities in charge transport measurements were detected, which I mainly attribute to the large surface to volume ratio of the porous Si-nc layers and therefore extreme sensitivity to gases or water vapour.

Optical transmission was evaluated to obtain the absorption coefficient of Si-nc layers. By application of a one-oscillator model to the evaluated real part of refractive index curves band gaps $E_{g,opt} \approx E_0/2$ were estimated as approximately half the resonance energy E_0, which agree well with the band gaps determined from measurements of PL.

EL was achieved from p-type crystalline silicon / Si-nc / metal structures. The dependence of EL on the current through the devices could be reproduced by an approach based on Shockley-Read-Hall recombination in competition with radiative recombination. In most of the measurements spectral distributions of EL and PL agree. For theses measurements I propose radiative recombination *via* quantum confined states as origin. For some measurements, however, EL is significantly blue-shifted compared to PL, which I explain by recombination *via* silicon oxide related states for the EL in contrast to the PL originating from transitions between quantum confined states.

Abbreviations and symbols

Abbreviations

AFM	atomic force microscope / microscopy
c-Si	bulk crystalline silicon
EL	electroluminescence
p-Si	p-type c-Si
PL	photoluminescence
PSi	porous silicon
RT	room temperature
S-Eq	Schrödinger-equation
SCR	space charge region
Si-nc	silicon nanocrystal(s)

Symbols

d	diameter of a Si-nc or number of dimensions
D	areal density of Si-nc or electronic density of states
d_c	number of confined space directions
g	degeneracy
E_F	Fermi-level
E_g	energy gap of semiconductor
E_g^*	separation energy of nanocrystals (analogue to E_g)
$f(E)$	Fermi-distribution $f(E) = \frac{1}{exp(\frac{E-E_F}{kT})+1}$
h	layer thickness
L	macroscopic extension in non-confined spatial direction
L_{quant}	mesoscopic extension in confined spatial direction
λ_{PL}	PL peak wavelength
m^*	effective mass
m_{1l}^*	longitudinal effective mass in x_1-direction
m_{it}^*	transversal effective mass in x_i-direction, i=2, 3
m_{dc}^*	**d**ensity of states effective mass of **c**onduction band $m_{dc}^* = (m_{1l}^* m_{2t}^* m_{3t}^*)^{1/3}$
P	porosity
T	temperature

Fundamental constants

Bohr-radius a_B	$0.53 \cdot 10^{-10} m$
Boltzmann-constant k	$8.6 \cdot 10^{-5} \frac{eV}{K} = 1.38 \cdot 10^{-23} \frac{J}{K}$
electrical field constant ε_0	$8.85 \cdot 10^{-12} \frac{As}{Vm}$
elementary charge e	$1.6 \cdot 10^{-19} As$
free electron mass m_e	$9.1 \cdot 10^{-31} kg$
magnetic field constant $\mu_0 = \frac{1}{\varepsilon_0 c_0^2}$	$1.26 \cdot 10^{-6} \frac{Vs}{Am}$
Planck-constant $\hbar$	$1.05 \cdot 10^{-34} Js$
velocity of light in vacuum c_0	$\approx 3.00 \cdot 10^{8} \frac{m}{s}$

Introduction

Since the stimulating talk of R. P. Feynman, “There’s Plenty of Room at the Bottom”, in 1959 [13] there has been tremendous effort in down-scaling physical devices and machines. Starting mainly with the aim to make machines like motors smaller and smaller, this trend has reached a point, where novel physical effects appear, especially at lengths of a few *nm*. This field of research can be described as *nanoscience* in contrast to *nanotechnology*, the mere down-scale of well-known devices to smaller lengths, while the physics behind stays the same as for their macroscopic counterparts.

Silicon nanocrystals (Si-nc), produced by laser pyrolysis of SiH_4, are composed of a crystalline Si core surrounded by an Si oxide shell and show effects belonging to the field of nanoscience. Due to quantum confinement the separation between conduction and valence band-like states is increased in comparison to the bulk band gap of crystalline silicon (c-Si). Thus photoluminescence (PL) of Si-nc is visible to the human eye (PL peak wavelengths $\lambda_{max} \gtrsim 700$ nm) in contrast to the PL emitted from c-Si, which lies in the infrared range ($\lambda_{max} = 1100$ nm). This main feature of Si-nc makes them a very interesting material for opto-electronic investigations. As PL had been already thoroughly investigated prior to the start of my work, this thesis relies on these results and expands investigations in other directions.

Most of the results presented in this thesis can be allocated to fundamental research, e. g. layer growth, charge transport and optics of thin layers composed of Si-nc. One chapter explores applications of Si-nc dealing with electroluminescence (EL). EL is encountered in everyday life in form of light emitting diodes (LEDs), indicating e. g. if an electric device is turned on or off, or which is the current mode of operation. EL has been investigated already with Si nanocrystals produced by other techniques like recrystallized Si-ion implanted SiO_2 layers [25]. Nevertheless it has not yet been reported for Si-nc deposited by laser pyrolysis. To investigate, if EL is achievable by devices incorporating these Si-nc, was one of the main tasks of the thesis. However silicon suffers from one severe disadvantage compared to some other semiconductors, which is its indirect band gap. There have been speculations that due to carrier confinement the band gap becomes partially direct. PL experiments have shown, however, that lifetime of excited carriers in Si-nc is still long compared to direct band gap semiconductor nanocrystals. (E. g. average PL decay times $\tau_{PL} \approx (100 \ldots 500)$ μs of Si-nc with diameters $d \approx 3.4$ nm [18] are more than a factor 5000 larger than average PL decay times $\tau_{PL} \approx 20$ ns of CdSe quantum dots with core diameters of 3.4 nm [6] at RT.) This hints to a predominance of indirect transitions in Si-nc. After the claim of [34], to have discovered optical gain in Si nanocrystals, the highly desired silicon laser, seemed to be feasible in near future. But up to now the results of [34] are still very controversially discussed [46], and the above mentioned rather indirect character of the Si-nc band gap makes me doubt if a laser built on the basis of Si nanocrystals will be realized soon or ever.

1 Deposition and samples

1.1 Deposition

Layers of Si-nc have been produced by CO_2 laser induced decomposition of SiH_4 (laser pyrolysis, Fig. 1). As a detailed description of the set-up has been published earlier [12], I will summarize only the main features. By pulsed CO_2 laser radiation a stretch-bond vibration in SiH_4 molecules is excited and they are decomposed into smaller compounds. These fragments agglomerate to Si-nc, which are extracted by a nozzle into vacuum. After passing a second nozzle (skimmer) they are collected on a substrate and build porous thin layers of circular shape with a spot diameter $\approx$ 7 mm. The Si-nc stick on the substrate and on each other due to intermolecular forces, which are large enough to counteract gravity. In the interaction volume of the CO_2 laser with the SiH_4 flow Si atoms start to agglomerate and in direction of the gas flow the agglomeration continues and Si-nc grow larger and larger. Therefore one can choose Si-nc of the desired size distribution by adjusting the nozzle at the right position, or as done here by variation of the CO_2 laser beam position. If the sample is removed, the Si-nc diameter distribution can be measured by a time of flight mass spectrometer (TOF). This measurement is performed during the adjustment of the CO_2 laser beam. Helium gas is used to confine the SiH_4 gas flow and to keep a laminar flow extending as far as possible below the the tube outlet. The substrate is kept at room temperature (RT) and the pressures in each of the chambers during deposition are indicated in Fig. 1. One has to note that the pressures are significantly increased, because gas is escaping from the flow reactor. Gas leaks through the nozzle into the left big chamber and through the skimmer into the middle chamber. The pressures measured without gas flow are relevantly lower, which means that the vacuum is cleaner from undesired gas species than the mentioned pressures suggest. For further size selection a mechanical chopper can be used, which by phase adjustment relative to the CO_2 laser pulse selects only a fraction

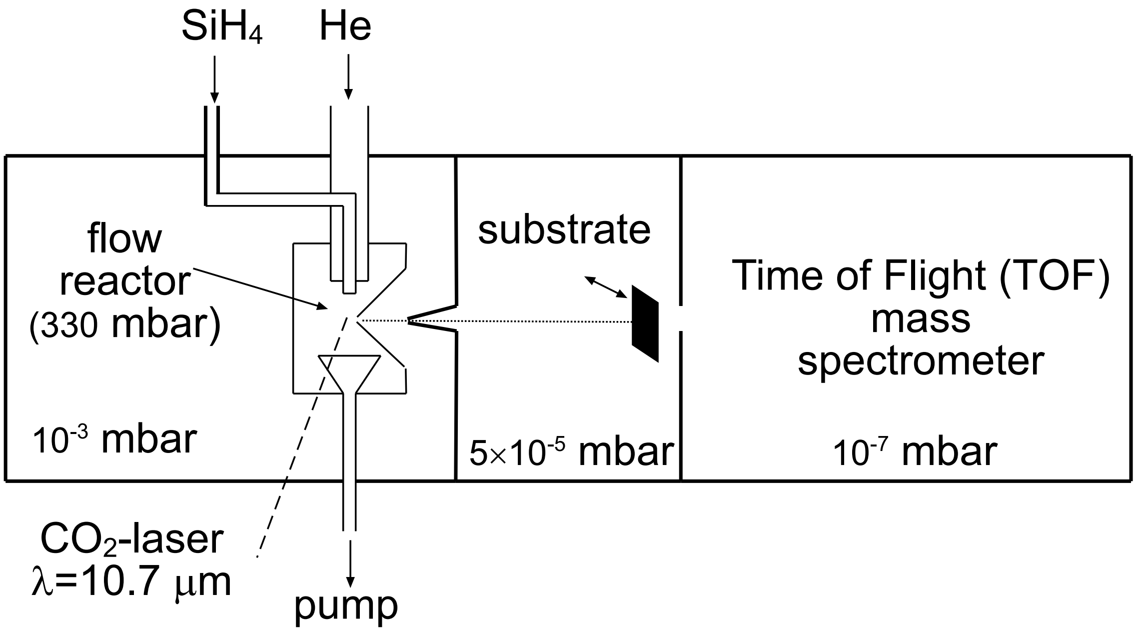

Figure 1: Sketch of apparatus designed for the deposition of Si-nc layers by laser pyrolysis.

of each Si-nc particle cloud. This size selection is possible, because Si-nc with smaller masses have higher velocities than Si-nc with larger masses. Size selection has not been used for any of the here treated samples, because it would further reduce the anyway low ($\approx 10 \ldots 1000$ nm/h) deposition rates .

1.2 Samples

Characteristic parameters of samples, which I report on in this thesis, are listed in Tab. 1.

Sample	layers	$h_{Si\text{-}nc}$ (nm)	λ_{PL} (nm)	d_{PL} (nm)
GO_10	quartz/partly Au/Si-nc	104 ± 9	771	4.7
GO_11A	p-Si/Si-nc/Pt	372 ± 15	823	5.6
GO_11B	p-Si/Si-nc/SiO_2/Pt	”	”	”
GO_14	glass/ZnO:Al/Si-nc	320 ± 8	884	7.4
GO_36B	p-Si/Si-nc/SiO_2/Pt	324 ± 12	811	5.4
GO_52	quartz/interdigital Au/Si-nc	490 ± 30	828	5.8
GO_54	”	530 ± 20	838	6.0
JO_60	quartz/Si-nc	-	821	5.6
JO_62	quartz/interdigital Cr/Si-nc	$440 \ldots 2900$	842	5.1
JO_69	mica/Si-nc	-	-	-
JO_70	quartz/interdigital Cr/Si-nc	$54 \ldots 110$	804	5.2
GP_10	HOPG/Si-nc	-	-	-

Table 1: Description of samples. Layer thickness h_{Si-nc} determined by AFM, PL peak wavelengths λ_{PL} and derived Si-nc diameters d_{PL}.

Layer thicknesses were estimated by atomic force microscopy (AFM) after carving a line scratch by a needle usually used for injections. On each sample at least 2 measurements have been performed and the average has been calculated. The errors as listed in Tab. 1 are determined to specify a range, which includes all measurement data. For all samples these errors are smaller than ±30 nm, except for samples JO_62, JO_70, which show lateral thickness inhomogeneities. On two of the samples (JO_69, GP_10) only a sparse distribution of Si-nc was deposited, hence a layer thickness is not well defined.

Evaluation of the layer thicknesses was performed by the “step height” function of the software supplied by Digital Instruments with the “Dimension Series SPM”, which was used for the measurements. For each measurement one has to specify two plateaus on different levels, e.ġ. one on the substrate and one on the layer (Fig. 2). On each area the mean height is calculated by the software and the step height is determined as the difference of these two values.

Si-nc diameters d_{PL} were estimated from photoluminescence (PL) measurements (Fig. 3) by translating the measured wavelengths λ_{max} of PL maxima *via* relation (2) into Si-nc diameters d_{PL}. Samples were excited by a frequency doubled continuous wave Nd:YAG laser at wavelength $\lambda_{exc} = 532$ nm with power of 0.2 μW focused on an area of about $(1\ \mu\text{m})^2$ in a confocal microscopy set-up. The PL yield was intensity calibrated with help of a tungsten calibration lamp and a pyrometer. PL yields Y_{PL} given in Fig. 3 are proportional to the spectral distribution of the emitted photon flux. On sample GP_10 the PL yield was too low to estimate a maximum.

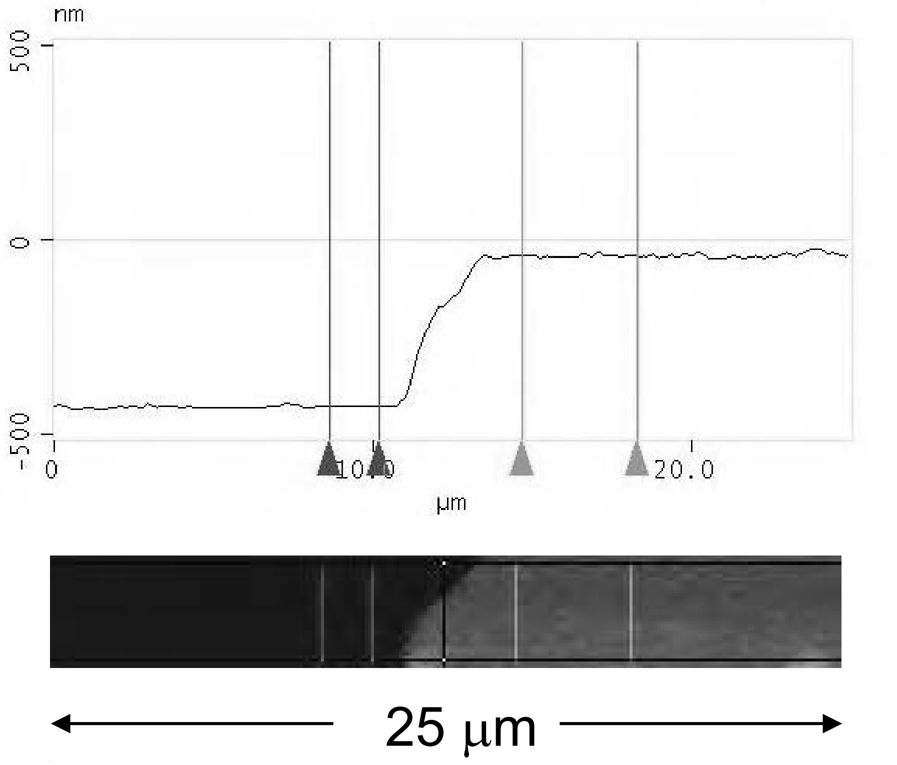

Figure 2: Estimation of layer thickness by AFM. Upper graph: mean height in a vertical line in the scan (lower graph) in dependence on lateral position. Lower graph: Tapping mode AFM scan on sample GO_11A, height is encoded in tones of grey-scale. Left side shows p-Si surface, right side Si-nc layer.

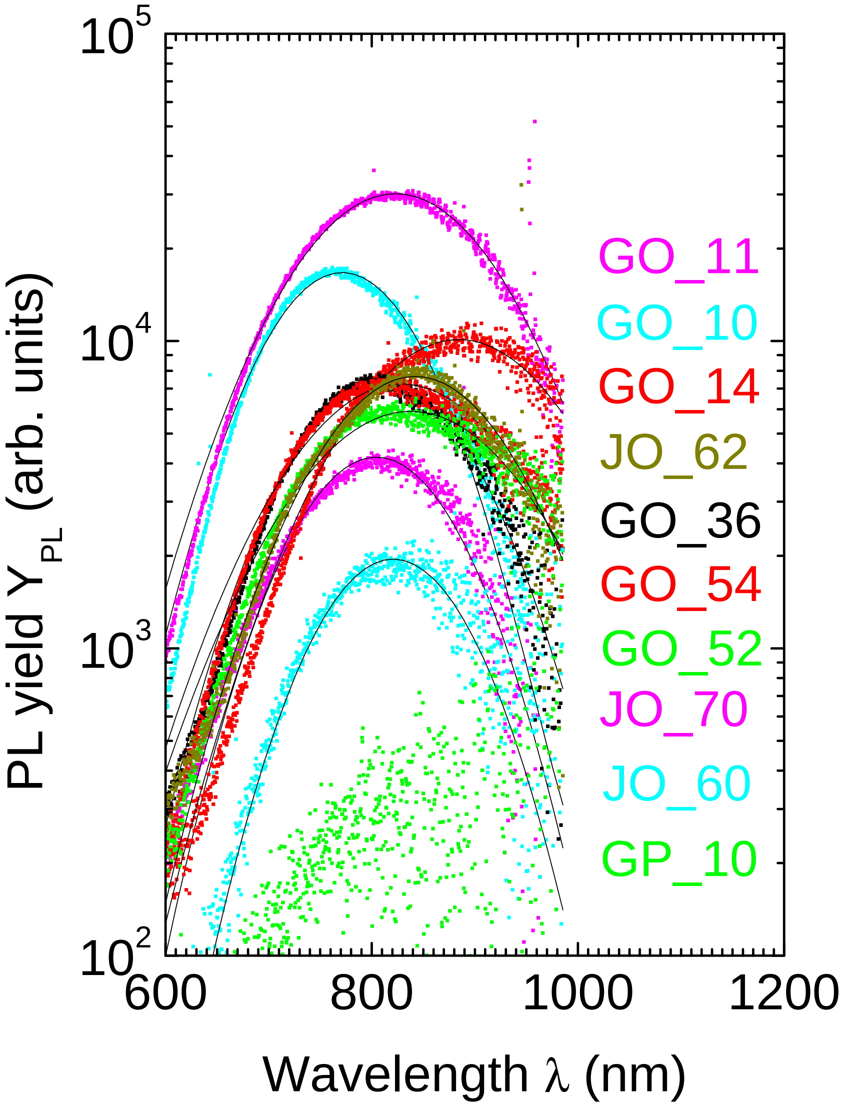

Figure 3: PL yield vs. wavelength. Solid lines: Gaussian fits.

2 Theory of quantum confinement

If semiconductors are scaled down to smaller and smaller structures and the extension in the 3 space directions reach scales of few *nm*, quantum mechanical effects modify the electronic states. According to the number of confined spatial dimensions d_c quantum confined structures are classified into three types:

1. quantum wells ($d_c = 1$),
2. quantum wires ($d_c = 2$),
3. quantum dots ($d_c = 3$).

The Si nanocrystals (Si-nc) investigated here belong to the category of quantum dots. In order to calculate the state functions of electrons in Si-nc, one can solve the Schrödinger-equation (S-Eq) in 1-electron approximation for electrons in the potential of the Si ion cores of the Si-nc. As nanocrystals are confined in three directions of space, this leads in effective mass approximation to the S-Eq for an electron in a 3-dimensional (3d) potential well. Therefore in the following we summarize solutions of the potential well S-Eqs. We report on the steps necessary to obtain the solutions of 4 kinds of potential wells:

1. infinite and finite spherical potential well (Section 2.1),
2. infinite and a special finite cubic potential well (Section 2.2).

In all calculations an isotropic effective mass m^* of the electrons and holes respectively is assumed. We will only outline the steps how to solve the S-Eqs and how to obtain the energy *eigen*-values.

2.1 Spherical potential well

Here we report on the infinite and finite spherical potential wells.

Remark	**Infinite 3d spherical potential well**	**Finite 3d spherical potential well**
Sketch of potential	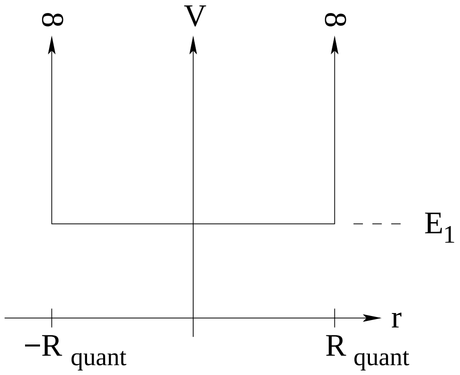	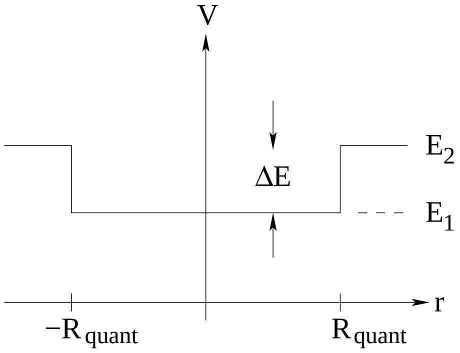
Stationary S-Eq	$(-\frac{\hbar^2}{2m^*}\Delta+V(r))\psi \; = \; E\psi$ with Laplace-operator $\Delta=\Delta_{r\theta\phi}=\frac{\partial^2}{\partial r^2}+\frac{2}{r}\frac{\partial}{\partial r}-\frac{(\mathbf{L}/\hbar)^2}{r^2}$ in spherical coordinates, where **L** is angular momentum operator (see Appendix B).	
Transformation of energy Transformed potential Transformed energy *eigen*-values	Choose E_1 as zero energy. $W(r) := V(r)-E_1$ $F := E-E_1$	Choose E_1 as zero energy and normalize ΔE to 1. $W(r) := (V(r)-E_1)/\Delta E$ $F := (E-E_1)/\Delta E$
Energy transformed S-Eq	$(-\frac{\hbar^2}{2m^*}\Delta+W(r))\psi \; = \; F\psi$	
Normalization in radial direction	normalized radial variable $\rho : \; = \; r/R_{quant}$	

Radially normalized potential	$X(\rho) := W(\rho R_{quant})$	
Radially normalized wave function	$\varphi(\rho,\theta,\phi) := \psi(\rho R_{quant},\theta,\phi)$	
Radially normalized Laplace-operator	$\Delta_{\rho\theta\phi} := R_{quant}^2 \Delta_{r\theta\phi}$	
Normalized S-Eq	$(-C_R\Delta_{\rho\theta\phi}+X(\rho))\varphi = F\varphi$ with $C_R := \frac{\hbar^2}{2m^* R_{quant}^2}$	
Solutions of normalized S-Eq (bound states)	$\varphi_{nlm}(\rho,\theta,\phi)$ $= C_{hl}\cdot Y_{lm}(\theta,\phi)\, j_l(\chi_{nl}\rho)$	for $\rho < 1$: $\varphi_{nlm}(\rho,\theta,\phi)$ $= C_{hl}\cdot Y_{lm}(\theta,\phi) A j_l(\chi_{nl}\rho)$ for $\rho > 1$: $\varphi_{nlm}(\rho,\theta,\phi)$ $= C_{hl}\cdot Y_{lm}(\theta,\phi) B h_l^{(1)}(i\kappa_{nl}\rho)$
	with spherical Bessel-functions j_l, spherical Hankel-functions $h_l^{(1)}$ of 1. kind, spherical harmonics Y_{lm} (see Appendix B), χ_{nl} denotes n-th zero point of j_l.	
Eigen-energies	$F_{nl} = C_R\chi_{nl}^2 = 3.781\cdot 10^{-20}\text{eVm}^2 \cdot \left(\frac{m^*}{m_0}\right)^{-1} R_{quant}^{-2}\chi_{nl}^2$	Continuity of φ_{nlm}, φ'_{nlm} at $\rho = 1$ demands: $q_{nl}\frac{\partial}{\partial\rho} ln(j_l(q_{nl}\rho))\|_{\rho=1}$ $= \kappa_{nl}\frac{\partial}{\partial\rho} ln(h_l^{(1)}(i\kappa_{nl}\rho))\|_{\rho=1}$ with $q_{nl} = \sqrt{\frac{F}{C_R}}$, $\kappa_{nl} = \sqrt{\frac{1-F}{C_R}}$ Energy *eigen*-values F_{nl} follow from solutions of the above equation.

2.2 Cubic potential well

The solution of the infinite cubic potential well and solutions of a specially designed finite cubic potential well are sketched in the table below.

The 3d finite cubic potential well with a constant potential inside a cube and a constant potential outside the cube is complicated to be solved due to complex boundary conditions. A 3d Schrödinger-equation with a potential, which is built of a sum of 1-dimensional finite cubic potential wells, however, is more easily solved, because the solutions are obtained as the product of the solutions to the 1-dimensional cases [48]. For simplicity this will be demonstrated for the 2d case here. The normalized potential $W(x,y)$ is composed of two 1d contributions

$$W(x,y) = W_1(x) + W_2(y),$$

as is shown in Fig. 4. Let ψ_i $(i = 1,2)$ be solutions of the 1d S-Eqs

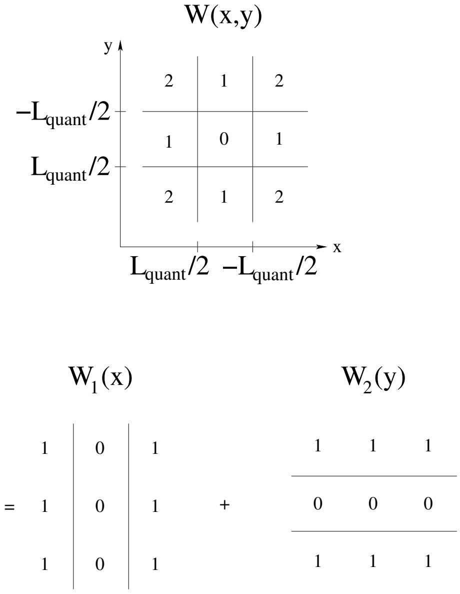

Figure 4: Potential $W(x,y)$ of the specially designed finite cubic 2d well is composed of two 1d potentials $W_1(x)$, $W_2(y)$.

$$(-\frac{\hbar^2}{2m^*}\Delta_i + W_i)\psi_i = F_i\psi_i.$$

Then $\psi(x,y) := \psi_1(x)\psi_2(y)$ is a solution of the 2d S-Eq, because

$$\begin{aligned}
& \left(-\frac{\hbar^2}{2m^*}\Delta + W(x,y)\right)\psi(x,y) \\
= & \left(-\frac{\hbar^2}{2m^*}\Delta + W_1(x) + W_2(y)\right)\psi_1(x)\psi_2(y) \\
= & \left[\left(-\frac{\hbar^2}{2m^*}\Delta_x\psi_1(x)\right) + W_1(x)\psi_1(x)\right]\psi_2(y) \\
+ & \left[\left(-\frac{\hbar^2}{2m^*}\Delta_y\psi_2(x)\right) + W_2(x)\psi_2(x)\right]\psi_1(y) \\
= & [F_1 + F_2]\,\psi_1(x)\psi_2(y).
\end{aligned}$$

Remark	**Infinite 3d cubic potential well**	**Special finite cubic potential well**
Sketch of potential	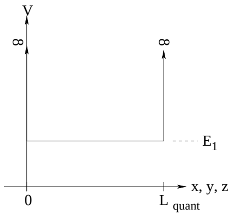	$V(x,y,z) = \begin{cases} E_1 & x,y,z \in I \\ E_1+\Delta E & 2 \text{ of } x,y,z \in I \\ E_1+2\Delta E & 1 \text{ of } x,y,z \in I \\ E_1+3\Delta E & x,y,z \notin I \end{cases}$ with $I := [-\frac{L_{quant}}{2}, \frac{L_{quant}}{2}]$
Stationary S-Eq	$$(-\frac{\hbar^2}{2m^*}\Delta + V(x,y,z))\psi \quad = \quad E\psi$$ with Laplace-operator $\Delta = \Delta_{xyz} = \frac{\partial^2}{\partial x^2} + \frac{\partial^2}{\partial y^2} + \frac{\partial^2}{\partial z^2}$ in rectangular coordinates.	
Transformation of energy Transformed potential Normalized energy *eigen*-values	Choose E_1 as zero point of energy. $W(x,y,z) := V(x,y,z) - E_1$ $F := E - E_1$	Choose E_1 as zero energy and normalize ΔE to 1. $W(x,y,z) := (V(x,y,z) - E_1)/\Delta E$ $F := (E - E_1)/\Delta E$
Energy transformed S-Eq	$$(-\frac{\hbar^2}{2m^*}\Delta + W(x,y,z))\psi \quad = \quad F\psi$$	
Normalized variables of space	$(\xi_1, \xi_2, \xi_3) := \frac{(x,y,z)}{L_{quant}}$	$(\xi_1, \xi_2, \xi_3) := \frac{(x,y,z)}{L_{quant}/2}$
Spatially normalized potential	$X(\xi_1, \xi_2, \xi_3) := W(\xi_1 L_{quant}, \xi_2 L_{quant}, \xi_3 L_{quant})$	
Spatially normalized wave functions	$\varphi(\xi_1, \xi_2, \xi_3) := \psi(\xi_1 L_{quant}, \xi_2 L_{quant}, \xi_3 L_{quant})$	
Spatially normalized Laplace-operator	$\Delta_{\xi_1\xi_2\xi_3} := L_{quant}^2 \Delta_{xyz}$	$\Delta_{\xi_1\xi_2\xi_3} := 2^{-2} L_{quant}^2 \Delta_{xyz}$

Normalized S-Eq	$(-C_{Lquant}\Delta_{\xi_1\xi_2\xi_3} + X(\xi_1,\xi_2,\xi_3)\varphi \quad = \quad F\varphi$	
	with $C_{Lquant} := \frac{\hbar^2}{2m^* L_{quant}^2}$	with $C_{Lquant} := \frac{\hbar^2}{m^* L_{quant}^2}$
Solutions of normalized S-Eq	$\varphi_{n_1n_2n_3}(\xi_1,\xi_2,\xi_3)$ $= A\cdot\varphi_1^{(n_1)}(\xi_1)\varphi_2^{(n_2)}(\xi_2)\varphi_3^{(n_3)}(\xi_3)$ with $\varphi_i^{(n_i)}(\xi_i) = sin(n_i\pi\xi_i)$ for $\xi_i \in (-1,1)$, $\varphi_i^{(n_i)}(\xi_i) = 0$ for $\xi \notin (-1,1)$, $n_i \in \{1,2,3\ldots\}$. (Follows with *ansatz* of separation.)	$\varphi_{n_1n_2n_3}(\xi_1,\xi_2,\xi_3)$ $= \varphi_1(\xi_1)\varphi_2(\xi_2)\varphi_3(\xi_3)$ with $\varphi_i(\xi_i)$ $= \begin{cases} A_i\sin(q\xi_i) & -1<\xi_i<1 \\ \text{or} & \\ A_i\cos(q\xi_i) & \text{”} \\ B_i^-\exp(\kappa\xi) & \xi_i<-1 \\ B_i^+\exp(-\kappa\xi) & \xi_i>+1 \end{cases}$ $q = F^{1/2}C_{Lquant}^{-1/2}$, $\kappa = (1-F)^{1/2}C_{Lquant}^{-1/2}$.
Eigen-Energies	$F_{n_1n_2n_3} = C_{Lquant}\pi^2(n_1^2+n_2^2+n_3^2)$ $= 3.732\times10^{-19}\text{eVm}^2\left(\frac{m^*}{m_e}\right)^{-1}$ $\cdot L_{quant}^{-2}(n_1^2+n_2^2+n_3^2)$	Continuity of φ_i, φ_i' demands for odd solutions: $\tan(q-\pi/2) = (C_{Lquant}^{-1}q^{-2}-1)^{1/2}$ for even solutions: $\tan(q) = (C_{Lquant}^{-1}q^{-2}-1)^{1/2}$ Energy *eigen*-values F follow from solutions of the above equations.

2.3 *Eigen*-energies of electrons and holes in 3d Si quantum wells

In order to determine the *eigen*-energies of the charge carriers in Si quantum wells, one has to account for the effective masses of electrons and holes respectively.

For the electrons an isotropic effective mass $m_e^* = m_{dc}^* := (m_{1l}^* m_{2t}^* m_{3t}^*)^{1/3} = 0.33 \cdot m_e$ has been assumed, which is the density of states effective mass in c-Si at room temperature. This results from effective electron masses $\frac{m_{1l}^*}{m_0} = 0.916$ (longitudinal), $\frac{m_{2t}^*}{m_0} = \frac{m_{3t}^*}{m_0} = 0.199$ (transversal) at RT according to [16]. (Note that the approach of [16] to include the degeneracy factor $\nu = 6$ of conduction band minima in the first Brillouin-zone in the density of states effective mass as $m_{dc}^{*(Green)} := \nu^{2/3}(m_{1l}^* m_{2t}^* m_{3t}^*)^{1/3}$ has not been followed here.)

The situation of the holes in the valence band is more complicated. There exist three different types of holes with different effective masses m_{hh}^*, m_{lh}^*, m_{sh}^* corresponding to three different kinds of valence bands [32]:

1. heavy holes ($m_{hh}^* = 0.49 m_e$),
2. light holes ($m_{lh}^* = 0.16 m_e$),
3. split-off holes ($m_{sh}^* = 0.25 m_e$).

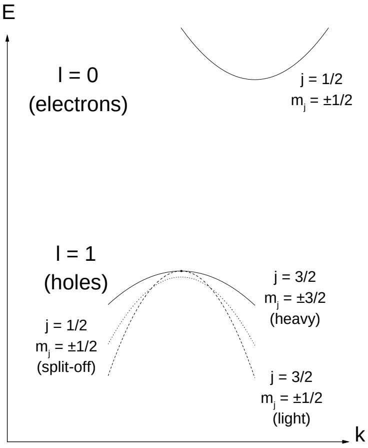

Figure 5: Sketch of c-Si band structure (Energy E vs. wave vector k). Quantum numbers of orbital angular momentum l, total angular momentum j, magnetic quantum number m_j. Three types of holes indicated: heavy h. (solid line), light h. (dashed line), split-off h. (dotted line).

In c-Si the valence band edge has p-orbital character, whereas the conduction band edge has s-character. This means the orbital angular momentum of the electrons in the valence band is $l = 1$, whereas the conduction band owns $l = 0$ (Fig. 5). In the valence band there are two possible values for the total angular momentum quantum number j, which originates from an addition of orbital momentum and spin: $j = \frac{3}{2}$ (heavy holes and light holes), $j = \frac{1}{2}$ (split-off holes). For $j = \frac{3}{2}$ there are four possibilities for the magnetic quantum number $m_j = \pm\frac{3}{2}$ (heavy holes) and $m_j = \pm\frac{1}{2}$ (light holes), whereas for $j = \frac{1}{2}$ there are only two degenerate possibilities $m_j = \pm\frac{1}{2}$. The selection rules for dipole allowed photon induced, phonon assisted transitions between the valence band and the conduction band are:

$$
\begin{aligned}
\Delta l &= \pm 1 \\
\Delta j &= 0,\ \pm 1 \\
\Delta m_j &= 0,\ \pm 1
\end{aligned}
$$

Hence we see, that in principle transitions between all types of valence bands and the conduction band are possible. Anyway we approximate the effective mass of the valence band by the effective mass of the heavy holes: $m_h^* \approx 0.5 m_e$. As the corresponding band has higher energies than the ones corresponding to the two other types of holes, the heavy holes are assumed to play the most significant role for the band structure of the Si-nc. Furthermore the right way of weighting the three effective hole masses to yield an isotropic mean effective hole mass depends on the quantity to be calculated (density of states, conductivity, thermal velocity) and is complicated to formulate in a general way.

In Tab. 4 the first 6 energy *eigen*-values F_{nl}, $F_{n_1n_2n_3}$ for electrons and holes in infinite spherical and cubic Si potential wells are summarized. We consider Si-nc with diameter $d =$ 5 nm. Thus as radius of the spherical well $R_{quant} = 2.5$ nm has been chosen and the edge length L_{quant} of the cubic well has been determined such, that the volume of the cube corresponds to the volume of the sphere:

n	l	χ_{nl}	g	$F_{nl}^{(e)}$(eV)	$F_{nl}^{(h)}$(eV)	n_1	n_2	n_3	g	$F_{n_1n_2n_3}^{(e)}$ (eV)	$F_{n_1n_2n_3}^{(h)}$ (eV)
1	1	3.14	1	0.18	0.12	1	1	1	1	0.21	0.11
1	2	4.49	3	0.37	0.24	2	1	1	3	0.42	0.22
1	3	5.76	5	0.61	0.39	2	2	1	3	0.63	0.34
2	1	6.28	1	0.72	0.48	3	1	1	3	0.76	0.41
1	4	6.99	7	0.90	0.59	2	2	2	1	0.84	0.45
2	2	7.73	3	1.10	0.72	3	2	1	6	0.97	0.52

Table 4: Lowest 6 energy *eigen*-values of electrons (e) and holes (h) in infinite spherical (F_{nl}) and cubic ($F_{n_1n_2n_3}$) Si quantum wells (according to Section 2.1, 2.2). χ_{nl}: n-th zeros of spherical Bessel-function j_l, g: degeneracy. Parameters: $R_{quant} = 2.5$ nm, $L_{quant} = 4.03$ nm, $m_e^* = 0.330 \cdot m_e$, $m_h^* = 0.5 \cdot m_e$.

$$
L_{quant}^3 = \frac{4}{3}\pi R_{quant}^3.
$$

By cyclic permutation of n_1, n_2, n_3 identical energy values are obtained for the cubic well, which are listed only once in Tab. 4.

2.4 Separation energies of Si-nc

In Si-nc the energy splitting E_g^* between the highest occupied state and the lowest unoccupied state (at temperature $T = 0$) differs from the energy gap $E_{g,c-Si}$ of crystalline silicon. The separation energy E_g^* is the analogue to the band gap of bulk semiconductors, where one has to keep in mind that in nanocrystals bands of states do not exist, but rather discrete states (Fig. 6).

In effective mass approximation E_g^* is calculated as

$$
E_g^* = E_{g0} + \Delta E_C + \Delta E_V + \Delta E_{Coulomb},
$$

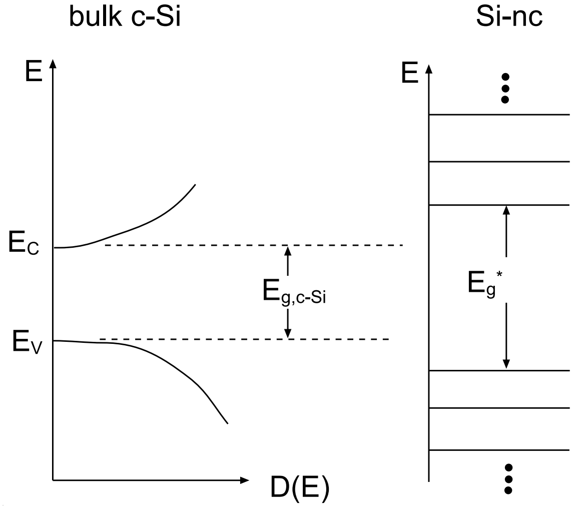

Figure 6: Band diagram of c-Si in comparison to the energy positions of electronic states in Si-nc (sketched). $D(E)$ denotes the density of states in c-Si.

where E_{g0} is the bulk energy gap of the semiconductor, ΔE_C, ΔE_V are confinement induced energy shifts of the conduction and valence bands corresponding to the lowest *eigen*-energies of the electrons / holes in the quantum wells and $\Delta E_{Coulomb}$ is the energy due to Coulomb-attraction between the electron and the hole, if an exciton is formed. By neglecting the Coulomb-interaction, one may approximate the separation energy with the results of the first *eigen*-energies of the infinite spherical potential well (Section 2.1):

$$\begin{aligned} E_g^* &\approx E_{g0} + \Delta E_C + \Delta E_V \\ &\approx E_{g0} + 3.781 \cdot 10^{-20} \mathrm{eVm}^2 m_r^{*-1} \pi^2 R_{quant}^{-2} \\ &\approx 1.12\ \mathrm{eV} + 7.51 \cdot 10^{-18} \mathrm{eVm}^2 d^{-2}, \end{aligned} \tag{1}$$

where $E_{g0} = 1.12$ eV is the RT energy gap of c-Si,

$$m_r^* := \left(m_e^{*-1} + m_h^{*-1}\right)^{-1} = \left(0.33^{-1} + 0.50^{-1}\right)^{-1} m_e = 0.20 m_e$$

denotes the reduced electron-hole mass and $d = 2R_{quant}$ the Si-nc diameter (Fig. 7). By application of linear combination of atomic orbitals (LCAO) technique [10] another formula for the dependence of the separation energy on the Si-nc diameter was derived [26]:

$$E_{g,Delerue}^* \approx E_{g0} + 3.73\ \mathrm{eV} \cdot (d/\mathrm{nm})^{-1.39}. \tag{2}$$

According to Fig. 7 both formulae agree for diameter $d = 3$ nm and due to their different exponents of the power laws they show increasing differences as the diameters depart from this value. For the estimation of the Si-nc diameters from PL measurements Eq. (2) will be used.

2.5 Excitons

For *quasi*-free electrons and holes in c-Si exerting Coulomb-interaction on each other there exist hydrogen-atom-like solutions. These so-called exciton states exhibit energies

$$\Delta E_{Coulomb} = -E_R^* n^{-2} \; (n = 1, 2, 3 \ldots)$$

with a “Rydberg-energy”

$$E_R^* = \frac{m_r^* e^4}{8\varepsilon_0^2 \varepsilon^2 h^2} = 13.6 \text{ eV} \cdot \varepsilon^{-2} \frac{m_r^*}{m_e} = 0.019 \text{ eV}$$

corresponding to the ground state and a “Bohr radius”

$$a_B^* = \frac{4\pi\varepsilon_0 \varepsilon \hbar^2}{m_r^* e^2} = 0.053 \text{ nm} \cdot \varepsilon \left(\frac{m_r^*}{m_e} \right)^{-1} = 3.2 \text{ nm}.$$

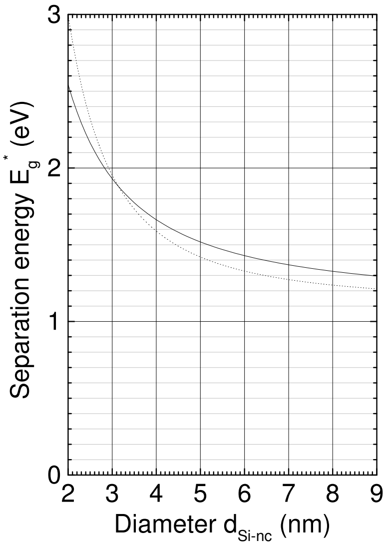

Figure 7: Separation energy E_g^* in dependence on Si-nc diameter. Dotted line: approximation (1) according to infinite spherical potential well. Solid line: equation (2) derived by LCAO technique [10].

The ratio of the quantum confinement radius R_{quant} to the Bohr radius a_B^* determines, how large the Coulomb-interaction $\Delta E_{Coulomb}$ is in comparison to the confinement induced energy shift $\Delta E_C + \Delta E_V$. Expressing the shift as

$$\Delta E_C + \Delta E_V = \frac{\hbar^2 \pi^2}{2 m_r^* R_{quant}^2} = E_R^* \left(\frac{\pi a_B^*}{R_{quant}} \right)^2$$

suggests that for small quantum dots the energy shift is large in comparison to the ground state exciton binding energy $|\Delta E_{Coulomb}| = E_R^*$. However this argumentation neglects, that for $R_{quant} < a_B^*$ the electron-hole pair is forced to stay together closer than in a distance a_B^*. This should alter the Coulomb-interaction from the value for quasi-free excitons such that $|\Delta E_{Coulomb}| > E_R^*$. According to [11] and [5], confinement can be classified into three regimes, depending on the relation between the quantization radius R_{quant} and the Bohr-radii of electrons ($a_{B,e}$), holes ($a_{B,h}$) and electron-hole pairs (a_B^*):

1. $R_{quant} \ll a_B^*$ (strong confinement),

2. $a_{B,h} < R_{quant} < a_{B,e}$ (intermediate confinement),
3. $R_{quant} \gg a_B^*$ (weak confinement),

where the single particle Bohr-radii of the electrons / holes are defined as

$$a_{B,e/h} = \frac{4\pi\varepsilon_0\varepsilon\hbar^2}{m_{e/h}^* e^2}.$$

For c-Si

$$a_{B,e} = 1.93 \text{ nm},\ a_{B,h} = 1.27 \text{ nm},\ a_B^* = 3.2 \text{ nm},$$

such that Si-nc with diameter $d = 5$ nm (radius $R_{quant} = 2.5$ nm), which have been mainly investigated in this thesis, can be classified to the transition range between strong and intermediate confinement. These Si-nc show an energy shift

$$\Delta E_C + \Delta E_V = 0.30 \text{ eV} \gg E_R^* = 0.019 \text{ eV}.$$

As the corresponding radius $R_{quant} = 2.5$ nm is not so small compared to $a_B^* = 3.2$ nm to expect an enormous deviation of $\Delta E_{Coulomb}$ from the bulk value E_R^*, we neglect the Coulomb-interaction in the calculations with Si-nc. More precisely we use (2), where also no Coulomb-interaction is included, for all following calculations.

2.6 Bloch-functions in nanocrystals

In the preceding estimations we have just added the energy of the potential well to the energy of a Bloch-function in the bulk semiconductor to obtain the total energy of an electron / hole in a quantum confined system. Why one can separate the whole problem into two parts like this, will be exposed in the following. We will stick to the one-dimensional case, but it is analogously valid in 2 or 3 dimensions.

Let's first recapitulate the solutions of a 1-dimensional infinite potential well (Fig. 8). The solutions of the Schrödinger-equation are sine-functions

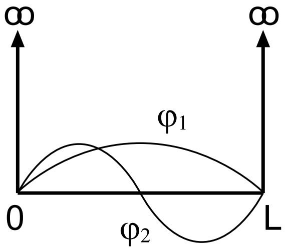

Figure 8: Infinite, 1-dimensional square well with first two solutions φ_1, φ_2.

$$\varphi_n(x) = \sin(k_n x)$$

with $k_n = n\frac{\pi}{L}$, $n = 1,2,3\ldots$ and the *eigen*-energies

$$E_n = \frac{\hbar^2\pi^2}{2m^*L^2}n^2. \tag{3}$$

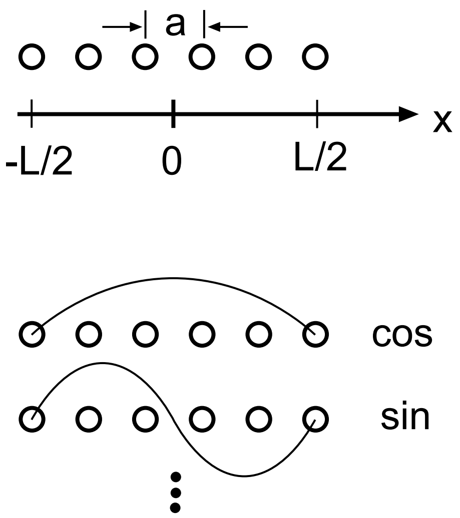

Figure 9: Finite 1-dimensional crystal. Circles symbolize positions of the atoms. Envelopes of first two solutions are sketched.

Let's visualize a confined crystal (Fig. 9). The Bloch-functions can be written as

$$\varphi_{nk}(x) = e^{ikx} f_{nk}(x),$$

where $f(x)$ has the periodicity of the lattice, n is the band index and k the quasi wave vector. They are exact solutions for the infinite crystal. We assume that they are still approximate solutions for the confined crystal. Additionally we demand boundary conditions

$$\psi(-\frac{L}{2}) = \psi(\frac{L}{2}) = 0 \tag{4}$$

for the solutions ψ of the problem. As the problem has symmetry of inversion, the energies of the solutions φ_{nk}, $\varphi_{n,-k}$ are the same, and they even exhibit the same functions $f_{nk} = f_{n,-k}$. Hence we can build new solutions to the same *eigen*-energy by adding these pairs of Bloch-functions,

$$\psi^+_{nk} := \varphi_{nk} + \varphi_{n,-k} = 2\cos(kx) f_{nk}(x)$$

or subtracting them,

$$\psi^-_{nk} := \varphi_{nk} - \varphi_{n,-k} = 2i\sin(kx) f_{nk}(x).$$

The boundary conditions (4) are fulfilled for the functions ψ^+_{nk}, if

$$k = (2l-1) \cdot \frac{\pi}{L},\ l = 1,2,3\ldots,$$

and for the functions ψ^-_{nk}, if

$$k = 2m \cdot \frac{\pi}{L},\ m = 1,2,3\ldots.$$

Summa summarum there exist only solutions for wave vectors

$$k_n = n \cdot \frac{\pi}{L},\ n = 1,2,3\ldots. \tag{5}$$

In other words, in the $E(k)$-diagram, which is a parabola in effective mass approximation, only special k-values represent states (Fig. 10). The functions $\psi_{nk}^{+/-}$ and $\psi_{n,-k}^{+/-}$ belong to the same states, because $\psi_{n,-k}^{+/-} = \pm\psi_{nk}^{+/-}$. For this reason the $E(k)$ relation has only been drawn for positive k. For 6 atoms in a chain (Fig. 9) we obtain exactly 6 solutions in one band of the confined crystal (Fig. 10), neglecting spin degeneracy. The corresponding energies are calculated as

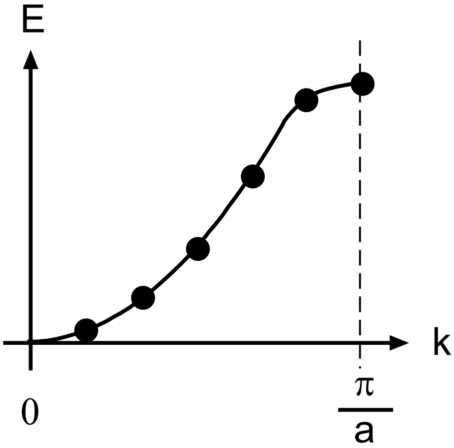

Figure 10: Electron dispersion relation for a 1-dimensional, finite crystal consisting of 6 atoms.

$$E(k_n) = \frac{\hbar^2 k_n^2}{2m^*} = \frac{\hbar^2 \pi^2}{2m^* L^2} n^2,$$

which is exactly the same result as the one (3) for the 1-dimensional infinite potential well. We have to keep in mind, that also the procedure followed here is an approximation, because the Bloch-functions are no correct solutions of the S-Eq at the boundaries of the crystal. But in contrary to the mere addition of the energies of an electron in an infinite crystal and the *eigen*-energies of electrons in a potential well, the procedure of combining Bloch-functions provides a picture about which kind of states electrons occupy in a confined crystal.

One can combine the above knowledge with the band structure of c-Si to gain a sketch of a “Si-nc band structure”. Therefore we mark all allowed wave vector values with a star in the band structure of c-Si (Fig. 11). If we assume Si-nc with diameter $d \approx 5$ nm, we yield according to Eq. (5) 10 allowed wave vectors $k_n \approx n \cdot \frac{\pi}{d}$, $n = 1,2,3\ldots10$ up to the end of the first Brillouin-zone at $k = \frac{\pi}{a} \approx k_{10}$, because the lattice constant of c-Si is $a \approx 0.54$ nm[29], which means $d \approx 10a$. The states marked by open circles at the maximum of the valence band and the minimum of the conduction band do not exist in Si-nc. Thus the transition from the valence band to the conduction band with lowest energy is the one indicated by the arrow in the figure. Fig. 11 provides an imaginative understanding of the increase of the “band gap” of Si-nc (rigorously separation energy E_g^*) with regard to c-Si. One has to be careful when using Fig. 11 for quantitative calculations, because the allowed wave vectors have been calculated assuming a 1-dimensional model of confinement, whereas the Si-nc diameter d and c-Si band structure originate from 3-dimensional considerations. But for qualitative imaginations about electronic transitions in Si-nc this picture is extremely suggestive and enlightening.

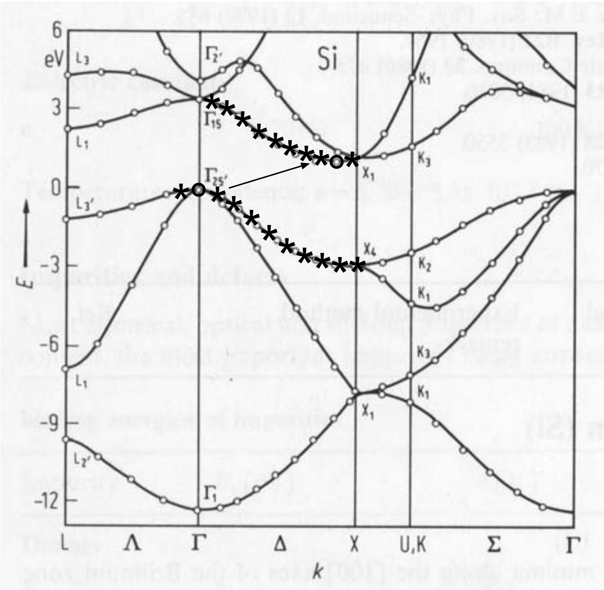

Figure 11: Electronic band structure (energy E vs. wave vector k) of c-Si [29]. The existing values of k for a 5 nm diameter Si-nc are marked by stars. The highest valence band state for bulk c-Si and the lowest conduction band state are indicated by open circles. These states do not exist in Si nanocrystals. Arrow shows the lowest interband transition for the Si-nc.

3 Atomic Force Microscopy

Atomic Force Microscopy (AFM) is a broadly used method to record the topology of a surface in the μm-range down to the atomic scale. In our case it was used to estimate layer thicknesses as described in Section 1.2 and to determine the Si-nc diameters of a sparse distribution of Si-nc on a substrate. Furthermore the surface structure of Si-nc agglomerates was monitored. All AFM topography scans shown in this chapter were recorded by a Nanoscope Multimode Scanning Probe Microscope of Digital Instruments and the measurements were performed by Frederic Houze in LGEP / SUPELEC in Paris Orsay.

3.1 Determination of diameters

10 Si-nc were chosen (marked by circles in Fig. 12) on a Si-nc / mica sample to measure their heights . The Si-nc heights have been determined by the “Analyze / Grain Size” function of the Digital Instruments Nanoscope III software. These heights represent the proper values for the diameters of the Si-nc, whereas the lateral dimensions on the AFM scan are obtained as the convolution of the AFM tip with the Si-nc height profile. An average Si-nc diameter $d_{Si-nc}^{(AFM)} = (5.7 \pm 0.9)$ nm has been estimated, where 0.9 nm is the standard deviation of the single values. The larger structures in Fig. 12 are agglomerates of Si-nc, which show extensions not related to the diameters of a single Si-nc.

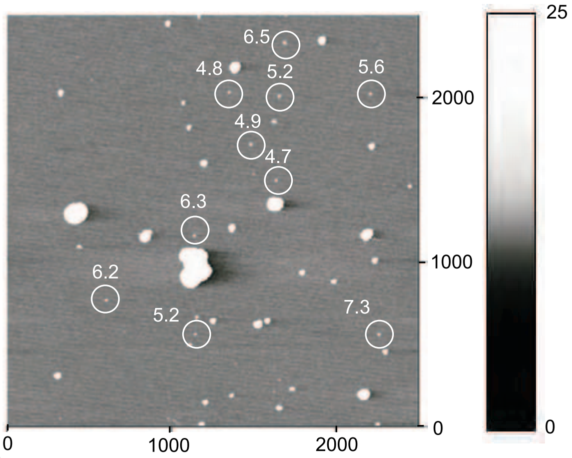

Figure 12: AFM topography scan of sample JO_69, Si-nc / mica. All numbers are in units of nm. Estimated heights of the encircled Si-nc are included in the graph.

Another thicker Si-nc layer (sample JO_70) has been deposited immediately after deposition of sample JO_69 in the same run. By PL measurements the Si-nc diameter has been determined *via* relation (2) to $d_{Si-nc}^{(PL)} = 5.2$ nm (Fig. 13), which agrees fairly well with the above mentioned mean diameter, determined by AFM.

3.2 Structure of agglomerates

The composed structure of agglomerates can be seen in AFM topography scans (Fig. 14). Fig. 14 (a) shows a zoom on the largest agglomerate in Fig. 12. Lateral structures down to ≈ 30 nm are resolved. This is not the range of a Si-nc diameter (≈ 5 nm), but one has to be aware that the topography image originates as a convolution of the real structures with the AFM tip.

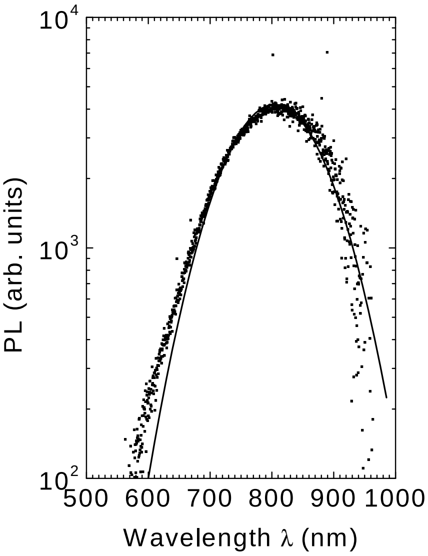

Figure 13: PL on sample JO_70, quartz/interdigital Cr/Si-nc. Squares: measurement. Line: Gaussian fit with peak position $\lambda_{max} = 804$ nm.

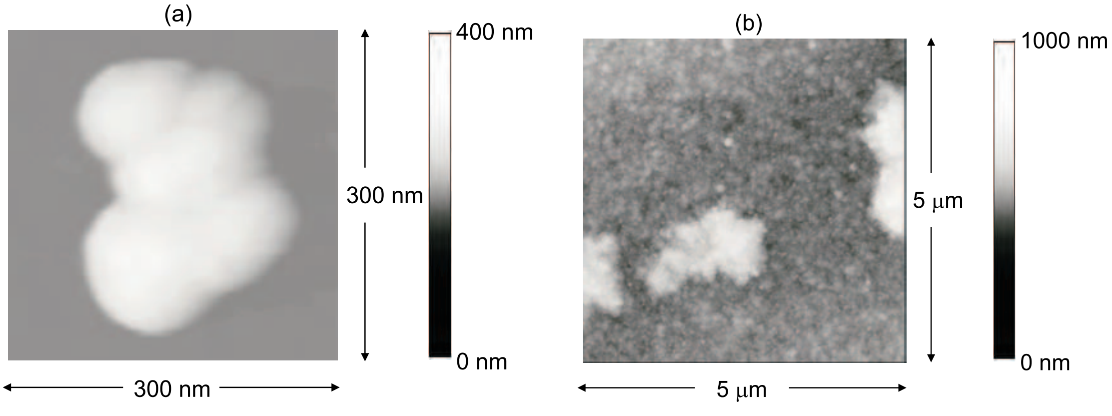

Figure 14: AFM topography scan showing the surface structure of agglomerates. (a) Sample JO_69, Si-nc / mica. (b) Sample GP_10 Si-nc / HOPG, agglomerates of Si-nc with length scales of some μm.

On the Si-nc layers agglomerates with lateral extensions of a few Si-nc diameter to extensions of about 10 μm are found. In the centre of Fig. 14 (b) an agglomerate of about 2 μm can be seen. Topography scans certainly show only the surface of the agglomerates, but from PL measurements on agglomerates as well on Si-nc in comparison it can be concluded that the diameter distribution of the Si-nc inside the agglomerates and for the single Si-nc on the layer underneath are similar [47]. Furthermore it should be noted, that the contours of single Si-nc are also not resolved in Fig. 14 (b). The smallest structures seen in the figure amount to $\approx$ 30 nm, which is not much larger than the diameter of the AFM tip. Probably these structures are again composed of agglomerates of single Si-nc. One hypothesis about the origin of the agglomerates is that Si-nc accumulate inside the nozzle during deposition, are detached after some time and impinge on the substrate.

4 Optical Transmission and Reflection

4.1 Introduction

Aims

Transmission experiments have been mainly carried out with the aim to determine the absorption coefficient α_2 of the layers. As a second result we obtain also the layer thickness d_2, which can be compared with results from AFM. Furthermore we estimate optical band gaps $E_{g,opt}$.

Outline

As will be derived later in Eq. (24), the optical transmittance through a system consisting of a layer, which is thin in comparison to the coherence length of the radiation, on a comparably thick substrate can be calculated as

$$T_{theo} = \frac{|t_{123}|^2 \, |t_{34}|^2 \, e^{-\alpha_3 d_3}}{1 - |r_{321}|^2 \, |r_{34}|^2 \, e^{-2\alpha_3 d_3}} \qquad (6)$$

where the undefined symbols in (6) denote transmission, reflection and absorption coefficients of the system and d_3 the substrate thickness. (The coefficients will be defined in Subsection 4.2.5.) Relevant at this point is that for every photon energy T_{theo} only depends on 2 unknown quantities: the real part $n_2' = re(n_2)$ and the imaginary part $n_2'' = im(n_2)$ of the complex refractive index n_2 of the layer. These parts influence the coefficients t_{123}, r_{123} in (6). (Here it is assumed that the layer thickness d_2 is known. It can either by estimated from an analysis of transmittance in the transparent region (see Subsection 4.5.1) or can be measured, e.g. by AFM. Also the substrate parameters are assumed to be known.) As there is only one equation for each value of energy E,

$$T_{theo}(n_2'(E), n_2''(E)) = T_{exp}(E),$$

where T_{exp} denotes the measured transmittance, one cannot determine the real and imaginary part of the refractive index for each single energy separately, unless one uses the Kramers-Kronig relation. But a Kramers-Kronig analysis is extremely complicated for this general case and lies outside of the scope of this PhD thesis. So we have to supply additional information, e. g. a model. We can assume some function $n_{2model}(P_1, P_2, P_3 \ldots P_N, E)$ with parameters P_1, P_2, $P_3 \ldots$ P_N for the complex refractive index, derived e. g. from an oscillator model. Then we can try to fit the modelled data T_{theo} to the experimental data T_{exp} by variation of the parameters $P_1 \ldots P_N$ and minimization of $\chi^2 := \sum_i (T_{1231coh\_inc}(E_i) - T_{exp}(E_i))^2$. This attempt is extremely difficult and ”does not fit pretty well” in most cases, because it is essential to find the proper initial values for the fit parameters; furthermore additional complications are induced by inhomogeneities, which effect that the extrema of interference do not reach the theoretically predicted values of (6). To circumvent these complexities we apply the method of envelopes [43, 41]. We plot the transmittance curves, draw the lower and upper envelopes enclosing the transmittance by means of a curved, flexible ruler and subsequently transfer the curves by scanning from the paper to the computer. From the envelope curves T_{exp_min}, T_{exp_max} an average transmittance $T_{exp\_geo} := (T_{exp\_min} T_{exp\_max})^{0.5}$ is calculated. As there follow rigorous analytical expressions for the theoretical envelope curves T_{theo_min} and T_{theo_max} from (6), a rigorous expression for the theoretical geometrical mean T_{theo_geo} can also be deduced (see Eq. (28), the same as the expression derived in [43]). By evaluation of the position of the extrema of T_{exp}

in the transparent region, one obtains the real part n_2' of the refractive index at these energies. While extrapolating n_2' in the region, where absorption occurs, the only open quantity n_2'' can be determined by use of Eq. (28) and equating

$$T_{theo\_geo}(n_2'(E), n_2''(E)) = T_{exp\_geo}(E). \tag{7}$$

From n_2'' the absorption coefficient is calculated according to $\alpha_2 = \frac{4\pi}{\lambda_0} n_2''$.

$$T_{1234\_inc\_0} = \frac{(1-R_{12})(1-R_{23})(1-R_{34})}{1-R_{23}(R_{12}+R_{34})-R_{12}R_{34}(1-2R_{23})}.$$

Remark: T_{theo_geo} approximately equals the incoherent transmittance T_{1234_inc}, Eq. (19), through the layer substrate system. So the absorption coefficient can alternatively be obtained by equating

$$T_{theo\_inc}(n_2'(E), n_2''(E)) = T_{exp\_geo}(E). \tag{8}$$

One has to keep in mind that although it is a very good approximation, it is not exact.

4.2 Theory

4.2.1 Basics

When an electromagnetic plane wave enters a medium, it retains its frequency, but alters its velocity and therefore its wavelength. This can be described by a change of the wave vector $k_0 = \frac{2\pi}{\lambda_0}$ to $k = \frac{2\pi}{\lambda_0} n$, where n is the refractive index of the medium and λ_0 is the vacuum wave length. Absorption in the medium can be included, if we let the refractive index n take complex values:

$$n = n' + in''.$$

The electric field at location x in direction of propagation in the medium becomes

$$E(x) = E_0 e^{ikx} = E_0 e^{i\frac{2\pi}{\lambda_0} n' x - \frac{2\pi}{\lambda_0} n'' x} \tag{9}$$

with the electric field amplitude E_0. As the energy flux density S is proportional to $|E(x)|^2$, we yield

$$S(x)\ \ |E_0|^2 e^{-\frac{4\pi}{\lambda_0} n'' x}.$$

This is Lambert-Beer's law of absorption with absorption coefficient

$$\alpha = \frac{4\pi}{\lambda_0} n''. \tag{10}$$

The plane wave (9) is a special solution to the Maxwell equations in a medium, if the relation

$$n^2 = \varepsilon$$

is fulfilled, where ε is the medium dielectric function.

If an electromagnetic wave meets an interface between two media, it is partly reflected and partly transmitted (Fig. 15).

Fresnel coefficients r_{ij} (t_{ij}) are defined as ratio of the electric field amplitude of the reflected (transmitted) part to the amplitude of the incident wave. They are determined by the refractive

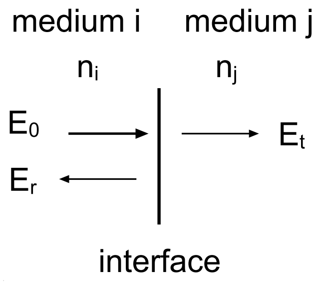

Figure 15: Reflection and transmission of an electromagnetic wave at an interface.

indices n_i, n_j of the media, the angle of incidence and the polarization of the wave. For normal incidence one yields :

$$r_{ij} = \frac{E_r}{E_0} = \frac{n_i - n_j}{n_i + n_j}, \quad t_{ij} = \frac{E_t}{E_0} = \frac{2n_i}{n_i + n_j} \ . \tag{11}$$

Reflection (Transmission) coefficients can also be defined for the energy flux density S, which can be calculated as the norm of the Poynting vector. S is proportional to $n|E_0|^2$, with the refractive index n of the medium and the electric field amplitude E of the wave. We yield the “intensity” coefficients

$$R_{ij} = \frac{n_i |E_r|^2}{n_i |E_0|^2} = \left|r_{ij}\right|^2 = \left|\frac{n_i - n_j}{n_i + n_j}\right|^2, \quad T_{ij} = \frac{n_j |E_t|^2}{n_i |E_0|^2} = \frac{n_j}{n_i}\left|t_{ij}\right|^2 = \frac{4n_i n_j}{\left|n_i + n_j\right|^2} \ . \tag{12}$$

4.2.2 Transfer matrix method

We investigate a system consisting of N layers of dielectric media (Fig. 16).

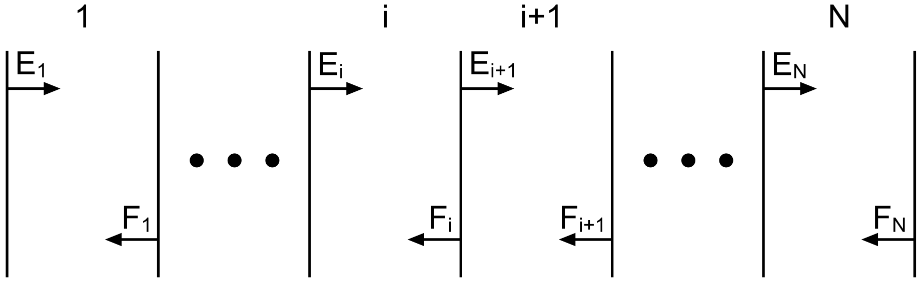

Figure 16: N-media system.

Let d_i denote their thicknesses, n_i their indices of refraction. The electric field in each medium is assumed to consist of a superposition of two plane waves, one with electrical field amplitude E_i moving to the right side and one with amplitude F_i moving to the left side. Now $2(N-1)$ equations can be deduced:

$$E_{i+1} = G_i t_{i,i+1} E_i + G_{i+1} r_{i+1,i} F_{i+1},$$

$$F_i = G_{i+1} t_{i+1,i} F_{i+1} + G_i r_{i,i+1} E_{i+1},$$

($i = 1,2,3\dots N-1$), where t_{ij}, r_{ij} are Fresnel transmission and reflection coefficients (11) and $G_i := e^{\gamma_i}$ contains a change in phase and an attenuation of the electromagnetic wave when protruding medium i; In detail

$$\gamma_i = i\varphi_i - \frac{\alpha}{2} d_i$$

with phase shift $\varphi_i := \frac{2\pi}{\lambda_0} n_i d_i$ and absorption coefficient $\alpha = \frac{4\pi}{\lambda_0} n''$ (see (10)). The above equations are equivalent to the following transfer formula:

$$\begin{pmatrix} E_i \\ F_i \end{pmatrix} = M_{i+1,i} \begin{pmatrix} E_{i+1} \\ F_{i+1} \end{pmatrix},$$

$(i = 1,2,3\dots N-1)$, with transfer matrix

$$M_{i+1,i} = \begin{pmatrix} G_i^{-1} t_{i,i+1}^{-1} & -G_i^{-1} G_{i+1} r_{i+1,i} t_{i,i+1}^{-1} \\ r_{i,i+1}^{-1} & G_{i+1}(t_{i+1,i} - r_{i+1,i} r_{i,i+1} t_{i,i+1}^{-1}) \end{pmatrix}.$$

In order to calculate the total transmission and reflection coefficients of the system, we have to solve for the $2N$ unknown field amplitudes E_i, $F_i (i = 1,2,3\cdots N)$, but our system of linear equations consists of only $2(N-1)$ equations. So we have to supply additional information, e. g. two of the field amplitudes. In a standard transmission/reflection experiment we know two field amplitudes by boundary conditions:

$$\begin{aligned} E_1 &= \mathit{given}, \\ F_N &= 0. \end{aligned}$$

Recursively one yields

$$\begin{pmatrix} E_1 \\ F_2 \end{pmatrix} = M_{21} \cdot M_{32} \cdot M_{43} \dots M_{N,N-1} \begin{pmatrix} E_N \\ 0 \end{pmatrix}.$$

Therefore the transmission and reflection coefficients of the field amplitude through the total system can be calculated as

$$t_{123\dots N} := \frac{E_N}{E_1} = \left\{ \left[M_{21} \cdot M_{32} \cdot M_{43} \dots M_{N,N-1} \cdot \begin{pmatrix} 1 \\ 0 \end{pmatrix} \right] \cdot \begin{pmatrix} 1 \\ 0 \end{pmatrix} \right\}^{-1}, \tag{13}$$

$$r_{123\dots N} := \frac{F_1}{E_1} = \frac{\left[M_{21} \cdot M_{32} \cdot M_{43} \dots M_{N,N-1} \cdot \begin{pmatrix} 1 \\ 0 \end{pmatrix} \right] \cdot \begin{pmatrix} 0 \\ 1 \end{pmatrix}}{\left[M_{21} \cdot M_{32} \cdot M_{43} \dots M_{N,N-1} \cdot \begin{pmatrix} 1 \\ 0 \end{pmatrix} \right] \cdot \begin{pmatrix} 1 \\ 0 \end{pmatrix}^{-1}}. \tag{14}$$

The transfer matrix method can also be used, when electromagnetic waves incoherently penetrate a multilayer system. Then we have to deal with energy flux densities (“intensities”) instead of field amplitudes. Let I_i (J_i) denote the energy flux densities of the electromagnetic wave moving in medium i to the right (left) side. Then we yield a system of linear equations similar to the one given above for the field amplitudes. This system can analogously be transformed into transfer formalism:

$$\begin{pmatrix} I_i \\ J_i \end{pmatrix} = M^*_{i+1,i} \begin{pmatrix} I_{i+1} \\ J_{i+1} \end{pmatrix},$$

$(i = 1, 2, 3 \ldots N-1)$, with transfer matrix

$$M^*_{i+1,i} = \begin{pmatrix} A_i^{-1}(1-R_{i,i+1})^{-1} & -A_i^{-1}A_{i+1}R_{i,i+1}(1-R_{i,i+1})^{-1} \\ R_{i,i+1}(1-R_{i,i+1})^{-1} & A_{i+1}\left[(1-R_{i,i+1}) - R^2_{i,i+1}(1-R_{i,i+1})^{-1}\right] \end{pmatrix},$$

where $A_i = e^{-\alpha_i d_i}$ is the absorbance of layer i and R_{ij} are the reflection coefficients (12) for the energy flux density. The transmission (reflection) coefficients $T_{123\ldots N\_inc}$ ($R_{123\ldots N\_inc}$) for the energy flux density through the total system are calculated analogously to Eqs. (13), (14).

In the following, results of the transmission and reflection coefficients from matrix transfer formalism (13), (14) are summarized. In every case the absorption and the phase shift in the first and the last medium are assumed to be zero ($\gamma_1 = \gamma_N = 0$). This corresponds to the case, where E_1would have been defined as close as possible to interface 1|2 and F_N close to interface N-1|N in Fig. 16. For our experiments this assumption is justified, because the outer media are air. In the incoherent case the transmission (reflection) coefficients directly resemble the transmittance (reflectance) of an experiment as they will be defined in section 4.3. In coherent cases the transmittance (reflectance) can be calculated from the amplitude coefficients analogously to (12):

$$T_{123\ldots N\_coh} = \frac{n_N}{n_1}\left|t_{123\ldots N}\right|^2 = \left|t_{123\ldots N}\right|^2,\; R_{123\ldots N\_coh} = \left|r_{123\ldots N}\right|^2.$$

Coherent transmission through a 3-media system

$$t_{123} := \frac{E_3}{E_1} = \frac{G_2 t_{12} t_{23}}{1 - G_2^2 r_{21} r_{23}}, \tag{15}$$

$$r_{123} := \frac{F_1}{E_1} = r_{12} + \frac{G_2^2 r_{23} t_{12} t_{21}}{1 - G_2^2 r_{21} r_{23}}. \tag{16}$$

Incoherent transmission through a 3-media system

$$T_{123\_inc} := \frac{I_3}{I_1} = \frac{A_2(1-R_{12})(1-R_{23})}{1 - A_2^2 R_{12} R_{23}}. \tag{17}$$

Coherent transmission through a 4-media system

$$t_{1234} := \frac{E_4}{E_1} = \frac{G_2 G_3 t_{12} t_{23} t_{34}}{1 - G_2^2 r_{21} r_{23} - G_3^2 r_{32} r_{34} - G_2^2 G_3^2 r_{21} r_{34}(t_{23} t_{32} - r_{23} r_{32})}. \tag{18}$$

Incoherent transmission through a 4-media system

$$T_{1234\_inc} = \frac{I_4}{I_1} = \frac{A_2 A_3 (1-R_{12})(1-R_{23})(1-R_{34})}{1 - A_3^2 R_{23} R_{34} - A_2^2 R_{12} R_{23} - A_2^2 A_3^2 R_{12} R_{34}(1-2R_{23})}. \tag{19}$$

If we neglect the absorption in media 2 and 3 we get the coefficient of ”transparent transmittance”

$$T_{1234\_inc\_0} = \frac{(1-R_{12})(1-R_{23})(1-R_{34})}{1 - R_{23}(R_{12}+R_{34}) - R_{12}R_{34}(1-2R_{23})}.$$

4.2.3 Substitution of a subsystem in a multilayer system

The field amplitudes E_1, F_2 of the incoming waves and the amplitudes E_2, F_1 of the outgoing waves on an interface between two media (Fig. 17 (a)) are related to each other via the Fresnel coefficients t_{12}, t_{21}, r_{12}, r_{21}:

$$\begin{aligned} E_2 &= t_{12}E_1 + r_{21}F_2, \\ F_1 &= r_{12}E_1 + t_{21}F_2. \end{aligned}$$

This can be summarized in the matrix equation

$$\begin{pmatrix} E_2 \\ F_1 \end{pmatrix} = \begin{pmatrix} t_{12} & r_{21} \\ r_{12} & t_{21} \end{pmatrix} \cdot \begin{pmatrix} E_1 \\ F_2 \end{pmatrix}. \tag{20}$$

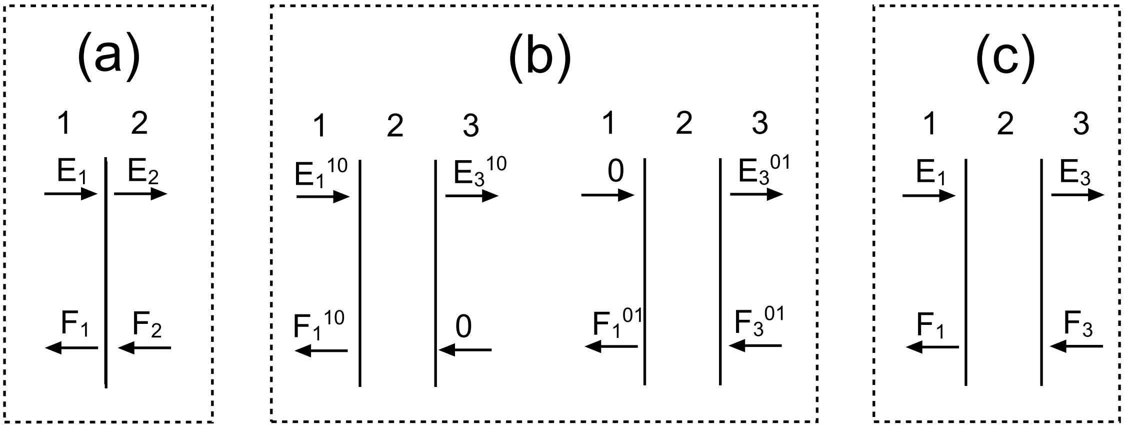

Figure 17: Substitution of an interface by a layer. (a) Just an interface between two media. (b), (c) Instead of the interface another layer is introduced.

On the other hand the amplitudes E_1, F_1 and E_3, F_3 in a 3-media system (special case of Fig. 16) are connected via the transfer formula

$$\begin{pmatrix} E_1 \\ F_1 \end{pmatrix} = M_{21} \cdot M_{32} \cdot \begin{pmatrix} E_3 \\ F_3 \end{pmatrix}. \tag{21}$$

Let's focus on 2 special solutions to (21), one, where light only enters from the left side ($F_3 = 0$) and one, where light only enters from the right side ($E_1 = 0$). We will call these solutions "fundamental solutions" and name them E_1^{10}, E_3^{10}, F_1^{10}, $F_3^{10} (= 0)$ and $E_1^{01} (= 0)$, E_3^{01}, F_1^{01}, F_3^{01} respectively (Fig. 17 (b)). According to (13), (14) these "fundamental solutions" define the reflection and transmission coefficients t_{123}, t_{321}, r_{123}, r_{321}, which can be summarized in the two equations

$$\begin{pmatrix} E_3^{(10)} \\ F_1^{(10)} \end{pmatrix} = \begin{pmatrix} t_{123} \\ r_{123} \end{pmatrix} \cdot E_1^{(10)}, \quad \begin{pmatrix} E_3^{(01)} \\ F_1^{(01)} \end{pmatrix} = \begin{pmatrix} r_{321} \\ t_{321} \end{pmatrix} \cdot F_3^{(01)} \ .$$

The 2 "fundamental solutions" to (21) added together yield again a solution to (21), because (21) is linear:

$$\begin{pmatrix} E_3^{(10)} + E_3^{(01)} \\ F_1^{(10)} + F_1^{(01)} \end{pmatrix} = \begin{pmatrix} t_{123} & r_{321} \\ r_{123} & t_{321} \end{pmatrix} \cdot \begin{pmatrix} E_1^{(10)} \\ F_3^{(01)} \end{pmatrix}.$$

In fact any solution of (21) can be obtained by this kind of superposition: First, one can achieve any desired couple E_1, F_3, because in one “fundamental solution” F_3 is zero in the other $E_1 = 0$. Second, if two of the quantities E_1, F_1, E_3, F_3 in (21) are known, the other two can be calculated, because (21) resembles a homogeneous system of two linear equations with 4 unknowns. (We assume that the matrix $M_{21} \cdot M_{32}$ has maximal rank.) Hence the matrix equation

$$\begin{pmatrix} E_3 \\ F_1 \end{pmatrix} = \begin{pmatrix} t_{123} & r_{321} \\ r_{123} & t_{321} \end{pmatrix} \cdot \begin{pmatrix} E_1 \\ F_3 \end{pmatrix} \tag{22}$$

is equivalent to (21).

Eq. (22) has the same structure as (20). If we substitute

$$\begin{gathered} E_2 \rightarrow E_3,\ F_2 \rightarrow F_3, \\ t_{12} \rightarrow t_{123},\ t_{21} \rightarrow t_{321},\ r_{12} \rightarrow r_{123},\ r_{21} \rightarrow r_{321}, \end{gathered} \tag{23}$$

(20) transforms to (22). This means that an interface can be replaced by an interface|layer|-interface system just by substitution according to (23). Here we have to set the absorption / phase-factors $G_1 = G_3 = 1$ in the calculation of the coefficients t_{123}, t_{321}, r_{123}, r_{321}, because the amplitude E_1 (F_3) is defined at the left (right) side of medium 1 (3) in Fig. 16, but the corresponding amplitudes E_1 (F_2) in Fig. 17 are defined in closest proximity to the interface to be substituted.

Analogously one can substitute an interface by a multi-sandwich consisting of many media stacked together. One just has to replace the transmission/reflection coefficients t_{12}, t_{21}, r_{12}, r_{21} by the appropriate multi-transmission/reflection coefficients, while using one of the transfer matrix formulae of subsection 4.2.2.

4.2.4 Coherent transmission through a 4-media system, recalculation

From matrix transfer formalism we have the coherent transmission coefficient (15) through a 3 media system. If we numerate the media 1, 3, 4 the formula reads

$$t_{134} := \frac{E_4}{E_1} = \frac{G_3 t_{13} t_{34}}{1 - G_3^2 r_{31} r_{34}}.$$

As has been shown in the proceeding subsection, we can substitute the interface between media 1 and 3 by an interface|layer 2|interface system just by substituting t_{13}, t_{31}, r_{13}, r_{31} by t_{123}, t_{321}, r_{123}, r_{321}. Thereby we yield

$$\begin{aligned} t_{1234} &= \frac{G_3 t_{123} t_{34}}{1 - G_3^2 r_{321} r_{34}} = \frac{G_3 \frac{G_2 t_{12} t_{23}}{1 - G_2^2 r_{21} r_{23}} t_{34}}{1 - G_3^2 \left(r_{32} + \frac{G_2^2 r_{21} t_{32} t_{23}}{1 - G_2^2 r_{23} r_{21}} \right) r_{34}} \\ &= \frac{G_2 G_3 t_{12} t_{23} t_{34}}{1 - G_2^2 r_{21} r_{23} - G_3^2 r_{32} r_{34} - G_2^2 G_3^2 r_{21} r_{34} \left(t_{23} t_{32} - r_{23} r_{32} \right)}. \end{aligned}$$

This result is identical with (18), which has been obtained by pure matrix transfer formalism.

4.2.5 Partially coherent transmission through a 4-media system

The optical transmission through a thin layer on a thick substrate often occurs coherently in the layer while the transmission through the substrate is incoherent. This can be attributed to 2 effects:

1. The substrate is not flat on a scale of the wavelengths of the electromagnetic waves used.
2. The coherence length of the monochromatic light is less than the thickness of the substrate.

Additionally also the interference in the thin layer is not perfect. One reason is that the light that is used to explore the layer is not strictly monochromatic, but has a band width $\Delta\lambda$. Another reason can be thickness inhomogeneities of the thin layer. In the following treatment we will neglect the latter two effects.

Analytically we have to calculate a mixture of coherent and incoherent transmission. From matrix transfer formalism we have the expression (17) for the incoherent transmittance through a 3-media system. If we numerate the media 1, 3, 4, the formula reads

$$T_{134\_inc} = \frac{A_1A_3(1-R_{13})(1-R_{34})}{1-A_3^2R_{13}R_{34}} = \frac{A_1A_3\frac{n_3}{n_1}|t_{13}|^2\frac{n_4}{n_3}|t_{34}|^2}{1-A_3^2|r_{31}|^2|r_{34}|^2} = \frac{n_4}{n_1}\cdot\frac{A_1A_3|t_{13}|^2|t_{34}|^2}{1-A_3^2|r_{31}|^2|r_{43}|^2}.$$

As was shown in the previous subsection and is illustrated in Fig. 18, we can substitute the interface between layers 1 and 3 by an interface|layer 2|interface system by substituting t_{13}, t_{31}, r_{13}, r_{31} by t_{123}, t_{321}, r_{123}, r_{321}.

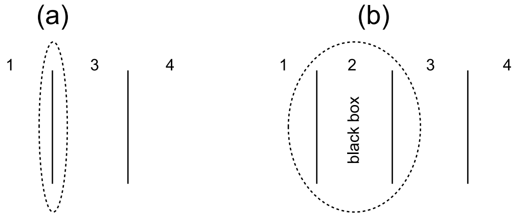

Figure 18: Substitution of layer 2 in a 4-media system to calculate the transmittance occurring coherently in layer 2 and incoherently in layer 3.

Then we yield the transmittance, which is calculated coherently through layer 2 and incoherently through the substrate (layer 3).

$$T_{1234\_coh\_inc} = \frac{n_4}{n_1}\cdot\frac{A_1A_3|t_{123}|^2|t_{34}|^2}{1-A_3^2|r_{321}|^2|r_{43}|^2} = \frac{|t_{123}|^2|t_{34}|^2e^{-\alpha_3d_3}}{1-|r_{321}|^2|r_{34}|^2e^{-2\alpha_3d_3}}, \tag{24}$$

assuming $A_1 = 1$, and using $A_3 = e^{-\alpha_3d_3}$, $r_{34} = -r_{43}$.

The last formula can be found in [42], where a similar but less detailed derivation is given as shown here. Analogously a reflection coefficient is found in this reference

$$R_{1234\_coh\_inc} = |r_{123}|^2 + \frac{|t_{123}|^2|r_{31}|^2|t_{321}|^2e^{-2\alpha_3d_3}}{1-|r_{321}|^2|r_{34}|^2e^{-2\alpha_3d_3}}.$$

4.3 Experiments

Specular transmittance T and reflectance R of Si-nc/quartz samples were measured for wavelengths $\lambda = (200\ldots3000)$ nm by a double beam spectrophotometer (Varian Cary 5E). Transmittance (Reflectance) is defined as ratio of the transmitted (reflected) energy flux density $S_t(S_r)$ to the incident energy flux density S_0:

$$T = \frac{S_t}{S_0},\ R = \frac{S_r}{S_0}.$$

The absolute accuracy of the spectrometer is approximately ±1 %. Inhomogeneities in the Si-nc layers make it necessary to confine the light beam to a small area of the sample surface. Therefore diaphragms (1 mm diameter) have been introduced in front of the samples (Fig. 19).

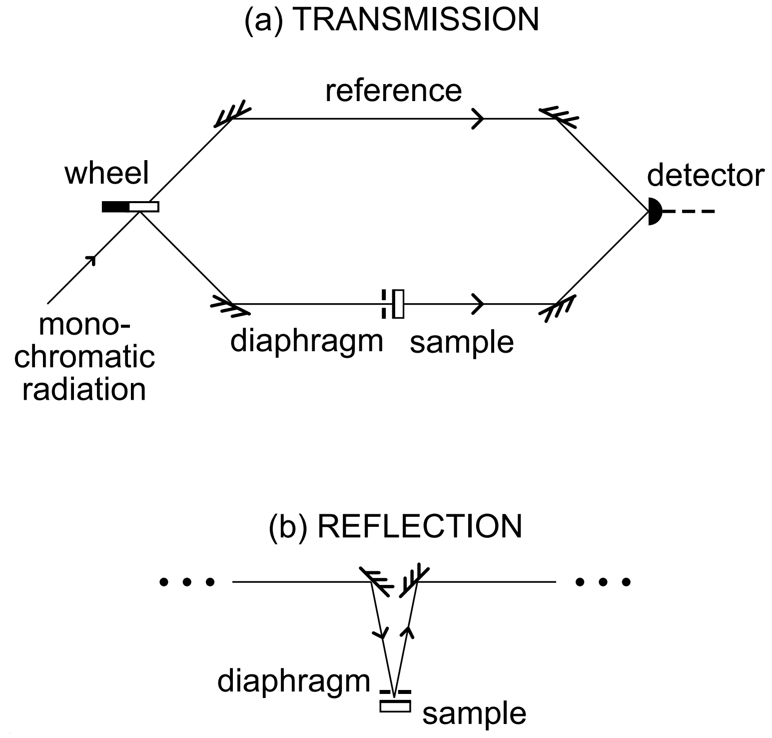

Figure 19: Sketch of beam path for transmission (a) and reflection (b) measurements. Only measurement beam is shown in (b).

The same light source is used for the reference and the measurement beam. This is managed by a turning wheel, which is partly transmitting and partly reflecting the beam. Thus the reference and measurement beam are switched on and off in an alternating series. The light of both beams is collected on the same detector and the signal is transfered to a computer. In the reflection measurement the incidence of light is almost normal to the sample surface. The beam path is simplified in the sketch. In the real experiment there are more mirrors in the set-up for the reflection measurement, which allow to measure the reflectance of a single mirror and to record baselines. The baseline corresponds to 100 % transmittance (no sample) and 100 % reflectance (perfect mirror) respectively; It has to be recorded before every measurement series and is used to calculate the specular transmittance T (reflectance R) from the detector signal.

4.4 Experimental results

Measured specular transmittance of Si-nc/quartz samples shows interference patterns for small energies, which is typical for thin films (Fig. 20). For large energies the transmittance decreases asymptotically towards zero.

For one of the Si-nc/quartz samples specular reflectance has been measured (Fig. 21). The measurement was performed with a circular diaphragm of 1 mm diameter in front of the sample.

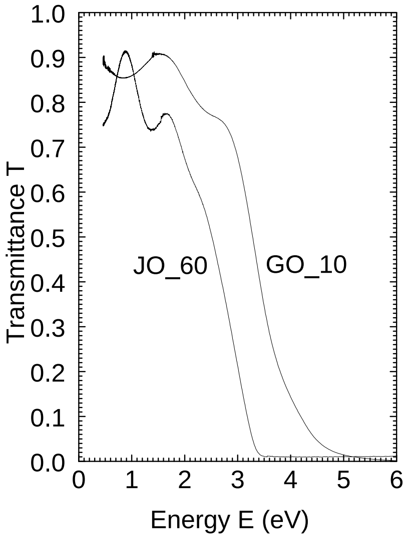

Figure 20: Measured specular transmittance of samples GO_10, JO_60.

This reduces the effect of layer inhomogeneities. Features of interference are observed for low energies. The measured reflectance R decreases drastically for energies $E \geq 4$ eV. From 4 eV to 6 eV it drops one order of magnitude. At the highest measured energy it becomes $R(6\text{ eV}) \approx 3 \cdot 10^{-3}$.

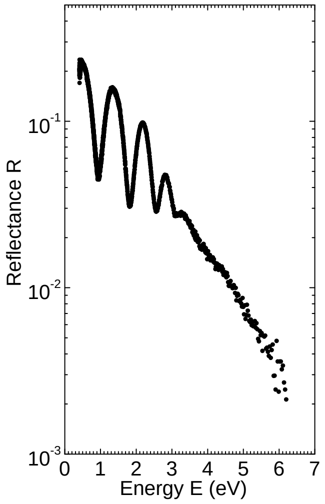

Figure 21: Specular reflectance measurement on sample JO_60.

4.5 Evaluation

4.5.1 Specular transmittance

I used a method, described in the thesis [41] to determine the real part n_2' of the refractive index and the absorption coefficient α_2. (At variance with the method described in [41] I will use Eq. (7) to determine α_2 in step 5 below, whereas in [41] approximation (8) was used. The approximation is very good and does not yield significant differences compared with the exact expression in most cases.) Only the partially coherent transmittance $T_{1234\_coh\_inc}$ through the layer-substrate system is needed as input for this evaluation. The procedure consists of the following steps:

1. Determination of envelopes T_{exp_min}, T_{exp_max} to the measured data T_{exp} and calculation of geometrical mean T_{exp_geo}.
2. Determination of layer thickness d_2.
3. Calculation of real part $n_2'(E_k)$ of refractive index at energies E_k of extrema of transmittance in the transparent region.
4. Quadratic extrapolation $n_{a0\_a1\_a2}'(E)$ of real part of refractive index in entire measured energy region.
5. Determination of imaginary part $n''(E_k)$ of refractive index and therefore the absorption coefficient α_2 as a function of T_{exp_geo} and $n_{a0\_a1\_a2}'(E)$.

In the following is shown, how the above steps are carried out in detail for a measurement on sample GO_10 (Fig. 22). (As an additional check the software “Diplot 4.3” [28] was used, which is designed for evaluation of optical thin film spectra. For sample GO_10 results obtained by a fit to T_{exp} with this program are included for comparison in the following graphs showing n_2' and α_2.)

Step 1: The measured transmittance T_{exp} in dependence on the energy E was plotted on a paper. With a flexible ruler the lower and the upper envelopes T_{exp_min}, T_{exp_max} were drawn (Fig. 22). The envelope curves were scanned, digitized to numerical data and interpolated with a computer. The geometrical mean was calculated as $T_{exp\_geo} := (T_{exp\_min}T_{exp\_max})^{1/2}$.

Step 2: First the orders k of the extrema have to be determined. The condition for the wavelengths λ_k at extrema is

$$2n_2'd_2 = k\lambda_k \tag{25}$$

with $k = 0.5, 1.5, 2.5\ldots$ for minima and $k = 1, 2, 3\ldots$ for maxima. From (25) follows that the extrema have equidistant energy positions, as long as n_2' is constant. In the transparent regime, where n_2' varies only little, the order k can be calculated from the energies or from the wavelengths of two adjacent extrema:

$$k = \frac{\lambda_{k+0.5}}{2\left(\lambda_k - \lambda_{k+0.5}\right)} = \frac{E_k}{2\left(E_{k+0.5} - E_k\right)}. \tag{26}$$

These calculated values of k are listed in the second column of table 5. As the refractive index slightly changes also in the regime of low energies, and absorption starts to obscure the real position of the extrema, the calculated values of k are not exact integers or integers $+\ 0.5$. The assumed values of k are listed in column 3. Now $n_2'd_2$ can be calculated from condition (25). In order to calculate the layer thickness d_2, the values of n_2' have to be known. We obtain n_2 in the transparent region from the measured absolute value T_{exp_geo}.

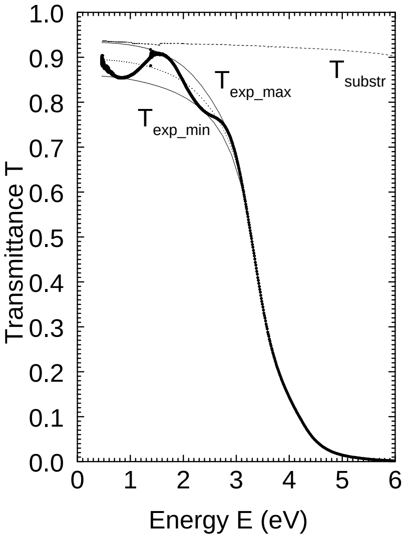

Figure 22: Transmittance of sample GO_10. Thick line: measurement T_{exp}. Geometrical mean T_{exp_geo} is found in middle of the envelopes T_{exp_min}, T_{exp_max}. Also included is the substrate transmittance T_{substr}.

Theoretically one has

$$T_{1234\_coh\_inc\_min/max} = \frac{16n_2^2n_3A_2}{(n_2+1)^3\left(n_2+n_3^2\right) \ {}^{+}_{-}\ 2\left(n_2^2-1\right)\left(n_2^2-n_3^2\right)A_2+(n_2-1)^3\left(n_2-n_3^2\right)A_2^2},$$

$$\begin{aligned} T_{1234\_coh\_inc\_geo} : &= \left(T_{1234\_coh\_inc\_min}\cdot T_{1234\_coh\_inc\_max}\right)^{1/2} \\ &= \frac{C_1A_2}{\left\{\left[C_2+C_3A_2+C_4A_2^2\right]\left[C_2-C_3A_2+C_4A_2^2\right]\right\}^{1/2}} \\ &= \frac{C_1A_2}{\left\{C_2^2+\left(2C_2C_4-C_3^2\right)A_2^2+C_4^2A_2^4\right\}^{1/2}}, \end{aligned} \tag{27}$$

with $C_1 := 16n_2^2n_3$, $C_2 := (n_2+1)^3\left(n_2+n_3^2\right)$, $C_3 := 2\left(n_2^2-1\right)\left(n_2^2-n_3^2\right)$, $C_4 := (n_2-1)^3\left(n_2-n_3^2\right)$. If we neglect the absorption in layer 2 by setting $A_2 = 1$, we obtain

$$T^2_{1234\_coh\_inc\_geo\_0} = \frac{C_1^2}{(C_2+C_4)^2-C_3^2} = \frac{8n_2'^2n_3^2}{[n_2'^4+n_2'^2(n_3^2+1)+n_3^2](n_3^2+1)}. \tag{28}$$

This quadratic equation in $n_2'^2$ can be solved for n_2':

$$n_2' = \left[-\frac{P}{2}\pm\left(\frac{P^2}{4}-n_3^2\right)^{1/2}\right]^{1/2} \tag{29}$$

with $P := -\left(\frac{8n_3^2}{T^2_{1234\_coh\_inc\_geo\_0}(n_3^2+1)} - (n_3^2+1)\right)$(after [43]). We assume $n_3 = 1.53$. By substituting $T_{1234\_coh\_inc\_geo\_0} = T_{exp\_geo\_0}$ with the experimental value, we determine n_2' (values in the 6th column of Tab. 5 for the + sign in (29), the - sign would result in $n_2' < n_3$). The layer thickness d_2 is now calculated from $n_2'd_2$ (4th column) and n_2' (6th column). If absorption was absent, all values obtained for d_2 should be identical, but the calculated values decrease for increasing k; Since absorption is smallest for $k = 0.5$, the value $d_2 = 218$ nm is the most exact and this value is taken for further calculations. (The layer thickness d_2 is about a factor 2 larger than the value $h_{Si-nc} = 104$ nm determined by AFM (Tab. 1); This difference results from the fact, that h_{Si-nc} was determined near the border of the Si-nc spot, whereas optical transmission was measured in the centre of the spot.)

E_k (eV)	k Eq. (26)	assumption k	$n_2'd_2$ Eq. (25)	$T_{exp\_geo}(E_k)$	n_2' Eq. (28)	d_2
0.83 (min.)	0.58	0.5	373	0.891	1.71	218
1.55 (max.)	1.19	1	400	0.872	1.82	220
$\approx$ 2.2 (min.)	1.83	1.5	$\approx$ 423	0.827	2.08	203
$\approx$ 2.8 (max.)	-	2	$\approx$ 443	-	-	-

Table 5: Results of evaluation of transmittance of sample GO_10.

Step 3: Having determined the layer thickness d_2, more accurate values of n_2' can be found by using Eq. (25). These values are more exact than the ones calculated in step 2 from T_{exp_geo}, because the positions λ_k of the extrema are less influenced by absorption than T_{exp_geo}. (See Tab. 6.)

E_k (eV)	n_2' $d_2 = 218$ nm and Eq.(25)
0.83 (min.)	1.71
1.55 (max.)	1.83
$\approx$ 2.2 (min.)	$\approx$ 1.94
$\approx$ 2.8 (max.)	$\approx$ 2.03

Table 6: More accurate values for the real part n_2' of the refractive index by using the condition for position of the extrema (sample GO_10).

Step 4: Now the real part n_2' of the refractive index is extrapolated with a quadratic polynomial in the entire measured energy region:

$$n_2' = a_0 + a_1 E + a_2 E^2. \tag{30}$$

By using only three of the values n_2' in Tab. 6 ($k = 0.5, 1, 1.5$) we obtain the coefficients by solving a system of linear equations:

$a_0 = 1.5741$, $a_1 = 0.1622$, $a_2 = 0.0019$. The result of the extrapolation is shown in Fig. 23.

Step 5: The absorption coefficient is calculated by equating $T_{1234\_coh\_inc\_geo} = T_{exp\_geo}$. Equation (27) shows that this leads to a quadratic equation in A_2^2. After solving for A_2 the absorption coefficient and the imaginary part of the refractive index are determined:

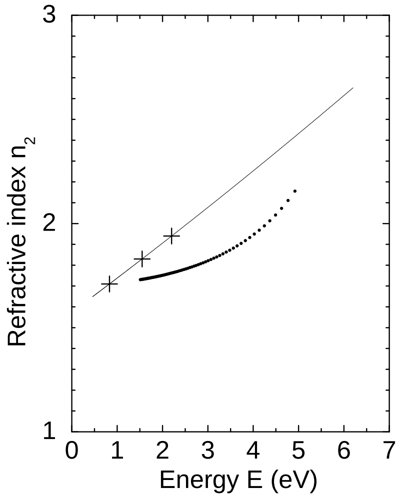

Figure 23: Real part n_2' of refractive index of sample GO_10. Crosses: values from Tab. 6, solid line: extrapolation from step 4, dots: results from software “Diplot”.

$$\alpha_2 = -\frac{\ln(A_2)}{d_2},$$

$$n_2'' = \frac{\lambda_0}{4\pi}\alpha_2,$$

with $\lambda_0 = \frac{1240\text{ nm eV}}{E}$. The absorption coefficient of sample GO_10 is shown in Fig. 24.

In the following I will summarize the evaluation of a measurement on sample JO_60. As the procedure is the same as for sample GO_10, only the results are shown in form of tables and graphs. The extrema have been determined as the energies at the osculation points between the measured transmittance T_{exp} and the envelopes T_{exp_min}, T_{exp_max} (Fig. 25).

E_k (eV)	k	assumption k	$n_2'd_2$	$T_{exp\_geo}(E_k)$	n_2'	d_2
	Eq. (26)		Eq. (25)		Eq. (28)	
±0.01				±0.001		
≈ 0.46 (min.)	0.52	0.5	≈ 674	≈ 0.836	≈ 2.03	332
0.90 (max.)	0.98	1	689	0.826	2.09	330
1.36 (min.)	1.66	1.5	684	0.792	2.27	301
≈ 1.77 (max.)	-	2	≈ 701	0.731	≈ 2.60	270

Table 7: Results of evaluation of transmittance of sample JO_60.

A quadratic extrapolation of the 3 first values of n_2' found in Tab. 8 according to 30 supplies an unreasonable result, because n_2' is largest for the middle energy. I have chosen the first three values of n_2' in the 6th column of Tab. 7 for the extrapolation and yield:

$a_0 = 2.0845$, $a_1 = -0.2489$, $a_2 = 0.2833$.

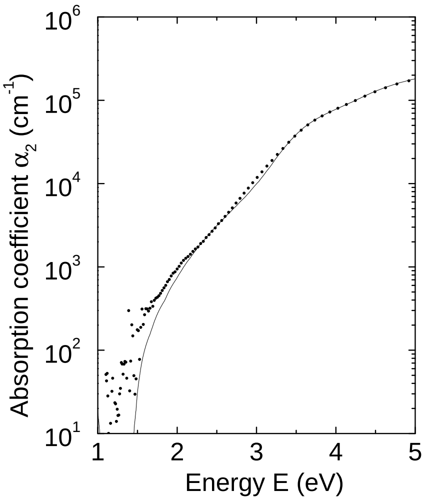

Figure 24: Absorption coefficient of sample GO_10. Solid line: evaluation according to [41], dots: results from software “Diplot”.

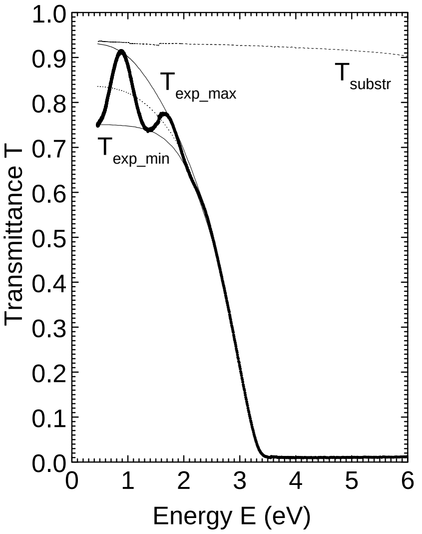

Figure 25: Transmittance of sample JO_60. Bold line: measurement T_{exp}. Geometrical mean T_{exp_geo} is found in middle of the envelopes T_{exp_min}, T_{exp_max}. Also included is substrate transmittance T_{substr}.

E_k (eV)	n'_2 $d_2 = 331$ nm and Eq.(25)
≈ 0.46 (min.)	≈ 2.04
0.90 (max.)	2.08
1.36 (min.)	2.07
≈ 1.77 (max.)	≈ 2.12

Table 8: More accurate values for the real part n'_2 of the refractive index by using the condition for position of the extrema (sample JO_60).

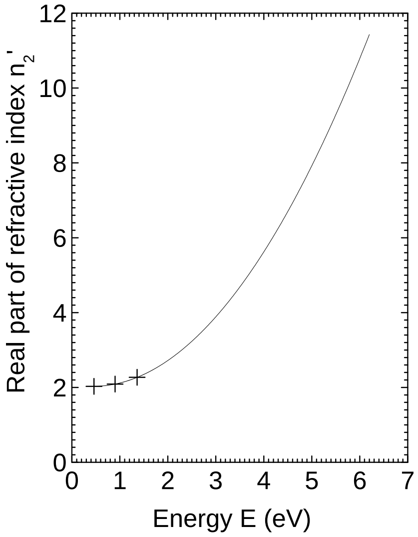

Figure 26: Real part n'_2 of refractive index of samples JO_60. Crosses: values from Tab. 7, solid line: extrapolation from step 4.

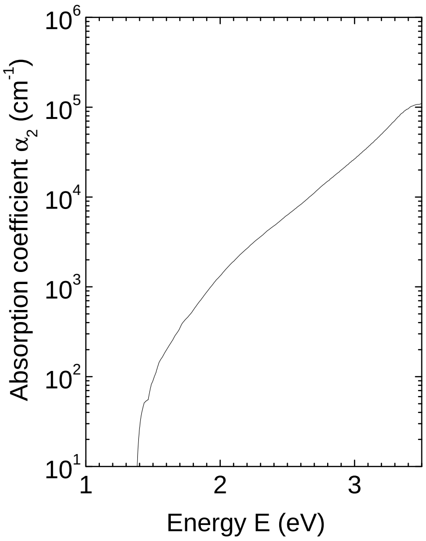

Figure 27: Absorption coefficient of sample JO_60. Solid line: evaluation according to [41].

4.5.2 Estimation of band gaps

According to [49] the real part n' of the refractive index follows the relation

$$n'^2 = 1 + \frac{E_0 E_d}{E_0^2 - E^2} \tag{31}$$

for many materials. The above given result resembles an effective 1-oscillator model, with E_0 being the resonance energy and E_d a "dispersion-energy" parameter. With substitution $Y := (n'^2 - 1)^{-1}$ follows the linear relation

$$Y = E_0^{-1} E_d^{-1} \left(E_0^2 - E^2\right)$$

between Y and E^2. A plot of Y vs. E^2 yields a straight line with E_0^2 as intercept on the E^2-axis.

Now in [45] was found, that for amorphous AsS films the optical band gap $E_{g,opt}$ and the resonance energy E_0 follow the relation $E_0 \approx 1.9 \cdot E_{g,opt}$. I will follow the procedure of the authors of reference [31], who calculated approximate optical band gaps $E_{g,opt}$ by

$$E_{g,opt} \approx \frac{E_0}{2}$$

for amorphous GeSe films and found good agreement with the Tauc gaps, determined from the absorption coefficients.

The n'_2-values obtained by the procedure of the proceeding subsection in step 3 are not suitable to determine the resonance energy E_0. They can only be calculated at extrema of transmittance and are therefore too few data (3 for both examined samples). In order to supply more n'_2-values for a fit according to (31) we calculate n'_2 from the geometrical mean $T_{1234\_coh\_inc\_geo}$ of the envelopes by Eq. (29) assuming again that absorption is negligible. Hence the calculated n'_2-values are accurate only for small energies and we expect them to fulfil relation (31) also only for small energies. Astonishingly the data for sample GO_10 describe a straight line over a large range ($E \leq 2.4$ eV) in the Y vs. E^2-plot (Fig. 28 (a)). A fit according to (31) has been

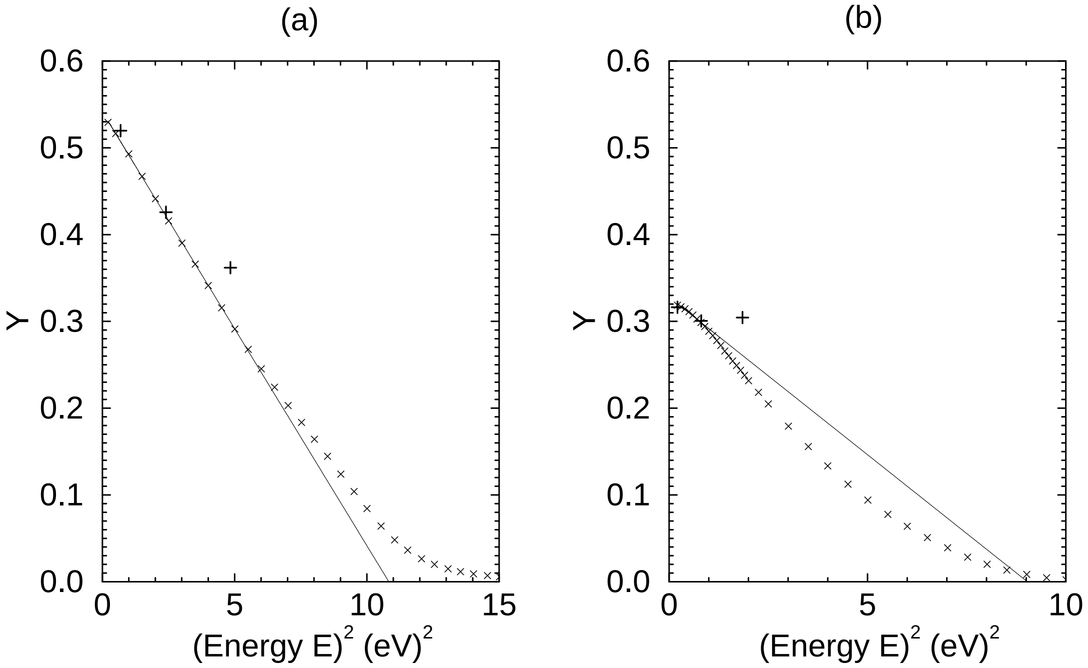

Figure 28: (a) sample GO_10, (b) sample JO_60; $Y := (n'^2 - 1)^{-1}$ in dependence on E^2. Crosses (x): n'_2 determined by (29). Crosses (+): n'_2 determined from position of extrema (Tabs. 6, 8). Solid lines: Fits to crosses (x) for small energies according to (31).

performed in the range $E = (0.46\dots2.1)$ eV and is included in the figure. For sample JO_60 a behaviour of the corresponding n'-data according to (31) is observed only for small energies. A fit has been performed in the range $E = (0.46\dots1.0)$ eV (Fig. 28 (b)). The results of the fit parameter E_0 are shown in Tab. 9. The relative deviation between $E_{g,opt}$ and the PL band gap E_{PL} is less than 0.025.

Sample	E_0(eV)	$E_{g,opt}$ (eV)	λ_{PL} (nm)	E_{PL}(eV)	relative deviation
GO_10	3.29	1.65	771	1.61	0.025
JO_60	3.005	1.503	821	1.510	0.005

Table 9: Resonance energies E_0 and approximated optical band gaps $E_{g,opt}$. For comparison the PL band gap $E_{PL} = 1240\,\text{eV nm}/\lambda_{PL}$ calculated from the wavelength λ_{PL} of maximal PL. Relative deviation$|E_{g,opt} - E_{PL}|/E_{PL}$.

Each of the fits in Figs. 28 (a) and (b) quite reasonably hits the first two of the n_2'-data (+), justifying the use of the n_2'-data (x), evaluated by (29). In each figure the third of the n'-data (+) lies above the fit lines. One reason can be inaccuracies of these (+)-data; They have been evaluated from transmittance in a range where absorption is no longer negligible. Furthermore relation (31) is only valid for energies $E \lesssim 0.4 \cdot E_0$. This can be estimated by studying the plots for substances NaF and CdS in [49]. For higher energies deviations can be observed because of the proximity of the band edge or excitonic absorption.

4.5.3 Diffuse reflection

From specular reflection measurements at the high energy end of the spectrum one can find out, whether diffuse scattering of the light is important for a specific sample [42]. Diffuse scattering is negligible for wavelengths large compared to the dimensions R of the structures on the layer. When the wavelengths approach the dimensions of the structures on the sample surface ($\lambda > R$), scattering strongly increases with decreasing wavelength (Rayleigh scattering S_R):

$$S_R \sim \lambda^{-4}.$$

For $\lambda \lesssim R$ scattering is almost wavelength independent (Mie scattering S_M). This is also the case for $\lambda < R$, where diffuse scattering can be explained just as an effect of reflection on the layer surface. Although there is little wavelength dependence of scattering for $\lambda \leq R$, nevertheless this is the regime where diffuse scattering is strongest. The increase of scattering should affect the diffuse reflectance R_{diff} to increase and therefore the specular reflectance R_{spec} to decrease, because light is scattered in all directions. This can also be deduced from the net formula

$$R_{spec} + R_{diff} + T_{spec} + T_{diff} + A = 1.$$

For high absorption ($\alpha_2 d_2 \gg 1$) almost all photons are absorbed in medium 2 (Si-nc layer). This means that the specular reflectance $R_{1234\_coh\_inc}$ converges to the reflection coefficient R_{12} of the air|medium 2 interface [42]:

$$R_{1234\_coh\_inc} \approx |r_{123}|^2 \approx |r_{12}|^2 = R_{12} = \frac{|1-n_2|^2}{|1+n_2|^2} = 1 - \frac{4n_2'}{(1+n_2')^2 + n_2''^2}, \tag{32}$$

where n_2', n_2'' are the real and the imaginary part of the refractive index of medium 2.

By AFM we have determined a root mean square roughness $R_q \approx 100$ nm of Si-nc layers (sample GO_54B showed $R_q = 145$ nm). Although the AFM roughness is measured only in direction perpendicular to the sample surface, it is also an estimate for the lateral dimensions R of the structures of the layer. So we expect the scattering to increase significantly in the proximity of 100 nm.

Specular reflectance was measured on sample JO_60 (Fig. 21). There is no convergence to a finite value to be seen. Reflectance seems rather to drop to zero for $E \to \infty$. According to [42] this is a hint for the presence of diffuse reflection. Semiquantitatively I will discuss the measured specular reflection $R(6\text{ eV}) \approx 3 \cdot 10^{-3}$ at the high energy end.

From the evaluation of specular transmission on this sample (Figs. 26, 27) we estimate the values of the optical constants and R_{12}, listed in the first row of Tab. 10. The value n_2' has been obtained by extrapolation from values of n_2' for energies $E \leq 1.5$ eV to an energy $E = 6.2$ eV. As this far extrapolation is doubtful, we supply other examples of calculations of $R_{12}(200\text{ nm})$ for similar materials. In [1] the values given in the second row of Tab. 10 are found, which correspond to a wavelength of 200 nm and a 30 … 40 nm thick Si-nc layer consisting of Si-nc with diameters $d \approx 3$ nm. Crystalline silicon has a quite high reflectance at 200 nm. In [29] the values shown in the third row of Tab. 10 are recorded for c-Si at 6 eV.

sample	reference	n_2'	n_2''	$\alpha_2[cm^{-1}]$	R_{12}
JO_60	Figs. 26, 27	11	≥ 0.16	$\geq 10^5$	≥ 0.69
Si-nc/quartz	[1]	1.75	0.5		0.10
c-Si	[29]	1.010	2.909		0.677

Table 10: Optical constants and reflection coefficient R_{12} at wavelength 200 nm (energy $E \approx 6$ eV) for three samples.

Each of the 3 above mentioned values of $R_{12}(E \approx 6\text{ eV})$ is more than a factor of 50 higher than the experimentally found reflectance $R(200\text{ nm}) = 2 \cdot 10^{-3}$. This is a strong hint, that diffuse reflectance indeed plays a significant role for sample JO_60 for energies $E = 4\text{ eV} \ldots 6\text{ eV}$. That is probably also the case for other Si-nc samples. A more quantitative treatment of diffuse reflection would require its measurement by an integrating sphere.

4.6 Discussion

4.6.1 Sources of error

Non-negligible contribution of diffuse reflection for $E > 4$ eV implies that the evaluation of the absorption coefficients (Figs. 24, 27) is erroneous in this range. Nevertheless the evaluations should not or only little be influenced by diffuse reflection for $E < 4$ eV. As we have only used the transmittance values for energies $E \leqslant 2.4$ eV to determine the optical band gaps (Subsection 4.5.2), this evaluation should not be affected by diffuse reflection.

4.6.2 Dense layer

As Si-nc layers are highly porous, the optical constants n_2', n_2'' obtained in subsection 4.5.1 are the result of a mixture of the components of the layers. The components are the Si-nc with their oxide shells and the empty pores. For comparison with other materials, it is necessary to formulate constants, which do not depend on the grade of porosity. Therefore we are interested to calculate the optical constants of a hypothetical dense layer of Si-nc. The standard way to calculate the real part n'_{Si-nc} and the imaginary part n''_{Si-nc} of a dense layer of Si-nc would be a transformation via Bruggeman's effective medium approximation ([7]). This would consist of the following steps:

1. calculation $\varepsilon'_2 + i\varepsilon''_2 = (n'_2 + in''_2)^2$,
2. transformation $\varepsilon'_2 + i\varepsilon''_2 \rightarrow \varepsilon'_{Si-nc} + i\varepsilon''_{Si-nc}$,
3. recalculation $n'_{Si-nc} + in''_{Si-nc} = (\varepsilon'_{Si-nc} + i\varepsilon''_{Si-nc})^{1/2}$.

According to (10) the absorption coefficient α_{Si-nc} can be calculated from n''_{Si-nc}. In the transformational step 2 one has to consider that the "measured pseudoelectric function [here ε_2] is described by the sum of the dielectric function of the film constituents averaged by their respective volume fractions" [15]. As the film constituents in our case are just a hypothetical dense Si-nc layer and air, we would yield

$$\varepsilon_2 = (1-P)\,\varepsilon_{Si-nc},$$

where P denotes the layer porosity (see Eq. (33)). The above given procedure involves a coupling between n'_2 and n''_2 in the calculation of n''_{Si-nc} and therefore α_{Si-nc}. As n'_2 is extrapolated in a large interval of energy and therefore rather un-precise in this range, this procedure is here not suitable to determine α_{Si-nc}.

We choose a pragmatic way to calculate α_{Si-nc} directly from α_2, based on the following considerations, and abandon to calculate n'_{Si-nc}. If light pervades a porous medium like a layer of Si-nc, it passes both, dense material and voids (Fig. 29 (a)). At the end of the layer the energy flux density has been attenuated by a factor

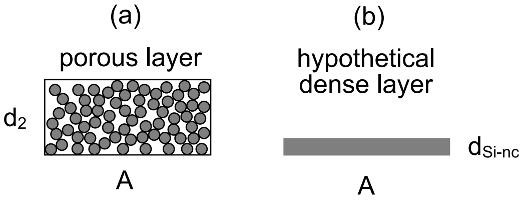

Figure 29: A porous Si-nc layer (a) is "compressed" to a hypothetical dense layer (b).

$$e^{-\alpha_2 d_2}.$$

If one would "compress" the layer to a dense layer with thickness d_{Si-nc} and absorption coefficient α_{Si-nc}, one would yield an attenuation

$$e^{-\alpha_{Si-nc} d_{Si-nc}}.$$

By equating these two exponential factors one yields

$$\alpha_{Si-nc} = \frac{d_2}{d_{Si-nc}}\alpha_2.$$

From the point that the volume filled by Si-nc is the same in the porous and the dense layer, follows the thickness d_{Si-nc} of the dense layer:

$$Ad_2P = Ad_{Si-nc},$$

where A is the area and P the layer porosity. We yield $d_{Si-nc} = d_2P$ and hence

$$\alpha_{Si-nc} = \frac{\alpha_2}{P}.$$

We take the mean value

$$P \approx 0.78$$

of the experimentally determined porosity and the one found by simulations (Eq. 36). Directly observable in the plot of the calculated absorption coefficients α_{Si-nc}(Fig. 30) is, that sample GO_10 has a larger band gap than JO_60, which is in accordance with the band values listed in Tab. 9. Furthermore the calculated absorption coefficients α_{Si-nc} of hypothetical dense layers are strikingly similar to the absorption coefficient of c-Si for energies $E \geq 1.7$ eV, whereas $\alpha_{Si-nc} < \alpha_{c-Si}$ for $E < 1.5$ eV. This is understood in the framework of band structure supposed for Si-nc in Fig. 11. Due to the lack of electronic states near the valence band maximum and the conduction band minimum in Si-nc there exist less transition for photon energies $E_{photon} \approx E_{g,c-Si} \ldots E_{g,Si-nc}$ in the range between the indirect band gap $E_{g,c-Si}$ of c-Si and the separation energy $E_{g,Si-nc}$ of Si-nc. This significantly reduces the absorption coefficient of Si-nc in comparison to the one of c-Si in this range. If the photon energy is sufficiently higher than the Si-nc separation energy, $E_{photon} \gg E_{g,Si-nc}$, a variety of possible transitions also exist for

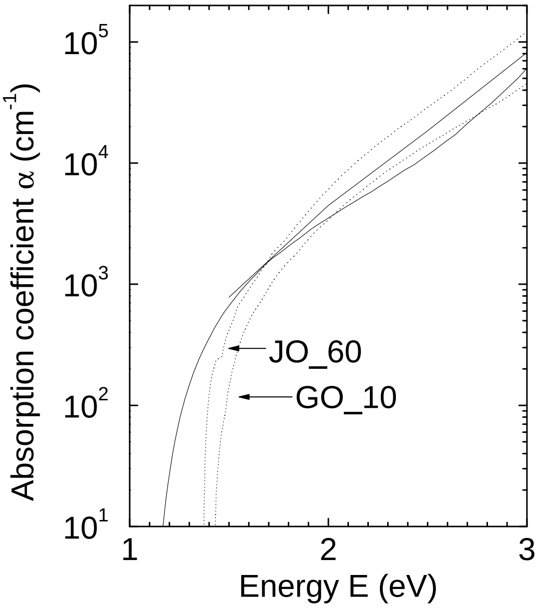

Figure 30: Absorption coefficients α_{Si-nc} of hypothetical dense layers of Si-nc. Dotted: samples GO_10, JO_60. Solid lines: absorption coefficient of c-Si at RT (lower curve: "pure c-Si" [17], upper curve: n-type c-Si, donor concentration $N_D = 2.3 \times 10^{14}$ cm^{-3} [3]) .

Si-nc, quite similar as in c-Si, which results in similar absorption coefficients for the confined and non-confined form of silicon.

5 Layer growth

5.1 Introduction

During deposition Si-nc impinge on the substrate and form a porous layer. I have simulated the layer growth by a computer program using the Monte-Carlo method, based on a simple stick-ball approach. When increasing the volume to surface ratio in the simulations one obtains a limit bulk value of the porosity of the layers. This value is compared to an experimentally estimated porosity of [1]. Furthermore the stick-ball model will be used later to explain charge transport during layer growth.

5.2 Model

The main properties of the computer model are:

1. Si-nc are treated as solid spheres.
2. Si-nc move one after the other towards a base area (substrate). Their local distribution perpendicular to their direction of motion is uniform.
3. The Si-nc stick as soon as they touch the base area or other Si-nc and do not move further (surface mobility assumed to be zero).

The number of spheres contributing to layer formation has been varied between $N = 100 \dots 10^6$. Quadratic base areas A with side lengths $a = (5 \dots 100)\, d$ have been chosen, where d corresponds to a Si-nc diameter (examples shown in Fig. 31).

5.3 Porosity

Former experiments showed a high porosity $P_{exp} = 0.706$ of Si-nc layers [1]. Porosity P is defined by the deficit in filling volume

$$P = 1 - \frac{4}{3} \frac{\pi R^3 \cdot N}{Ah}, \tag{33}$$

where R is the Si-nc radius, A the base area of the regarded volume, N the number of Si-nc in this volume and h height of the volume. As the upper surfaces of the layers show large roughness, the definition of the layer thickness h is not trivial. One can choose the position of the top of the highest located Si-nc, which will be denoted by h_{max} (Fig. 32 (a)).

An average value h_{av} for the height is obtained by "Monte Carlo probing" of the upper surface: A Si-nc probe impinges 1000 times on the completely simulated arrangement and is removed after each probing event; h_{av} is the average of the “south pole positions” of the Si-nc at these probing events (Fig. 32 (b)). The corresponding filling volumes are calculated as $V_{max} = h_{max} \cdot a^2$, $V_{av} = h_{av} \cdot (a-d)^2$.

In the calculation of V_{av} half a Si-nc diameter ($0.5d$) has been subtracted on each side of the base area, because in the bulk in a region of a distance of one Si-nc diameter also Si-nc partially lying outside the simulation volume would contribute to the filling. Corresponding to V_{max} and V_{av} porosities P_{max}, P_{av} have been calculated according to (33) as upper and lower estimates for the bulk porosity $P(\infty)$. For small numbers of Si-nc in the simulation and small filling volumes V the boundary surface $S = 2a^2 + 4ah$ has large influence on the calculated porosity. To quantify the influence of boundary effects we calculate the volume to surface ratio $\eta = V/S$. The larger

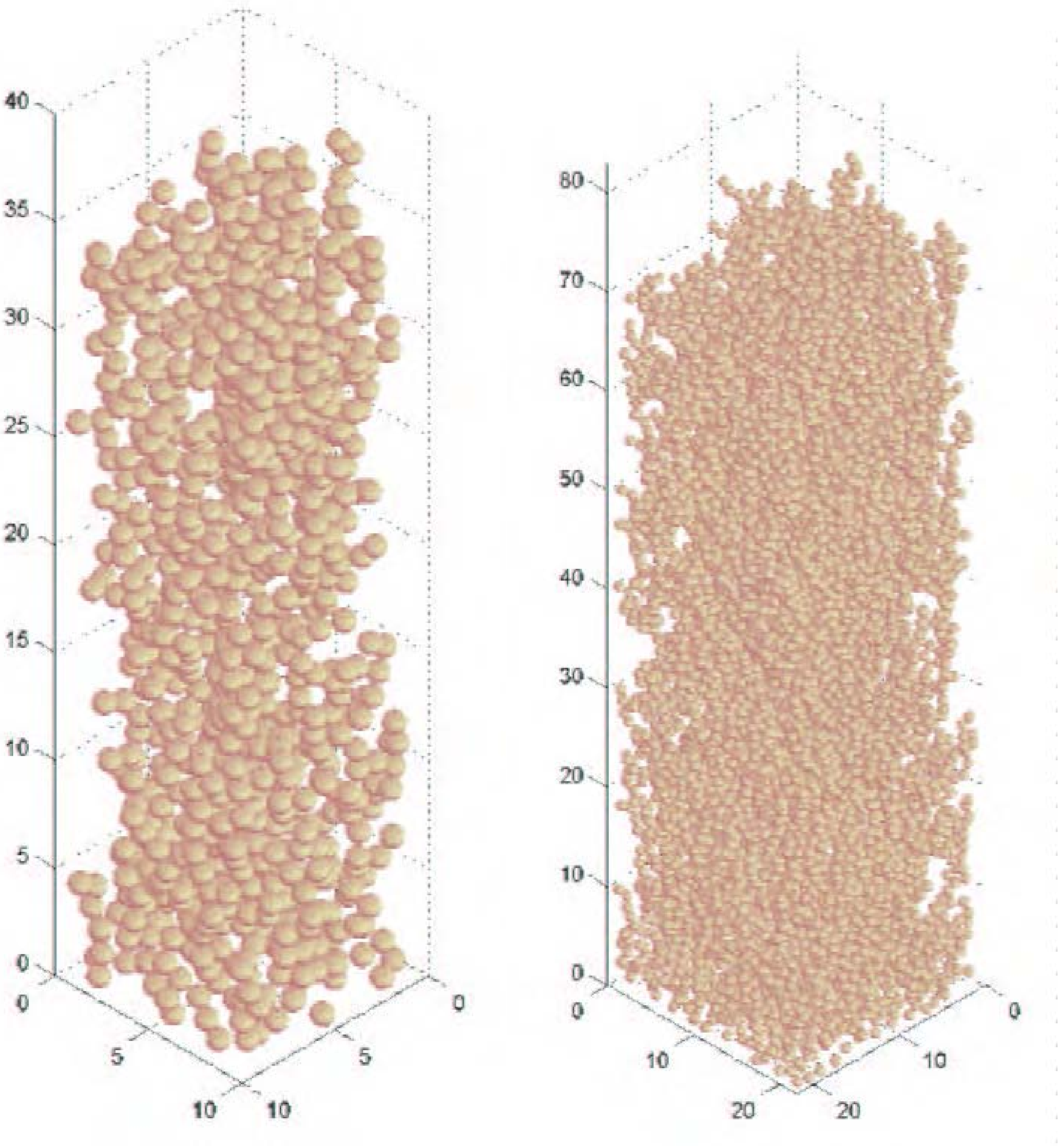

Figure 31: Simulated Si-nc arrangements according to model with 1000 Si-nc (diameter = 1) on a 10 × 10 square base area and 10000 Si-nc on a 22 × 22 area respectively.

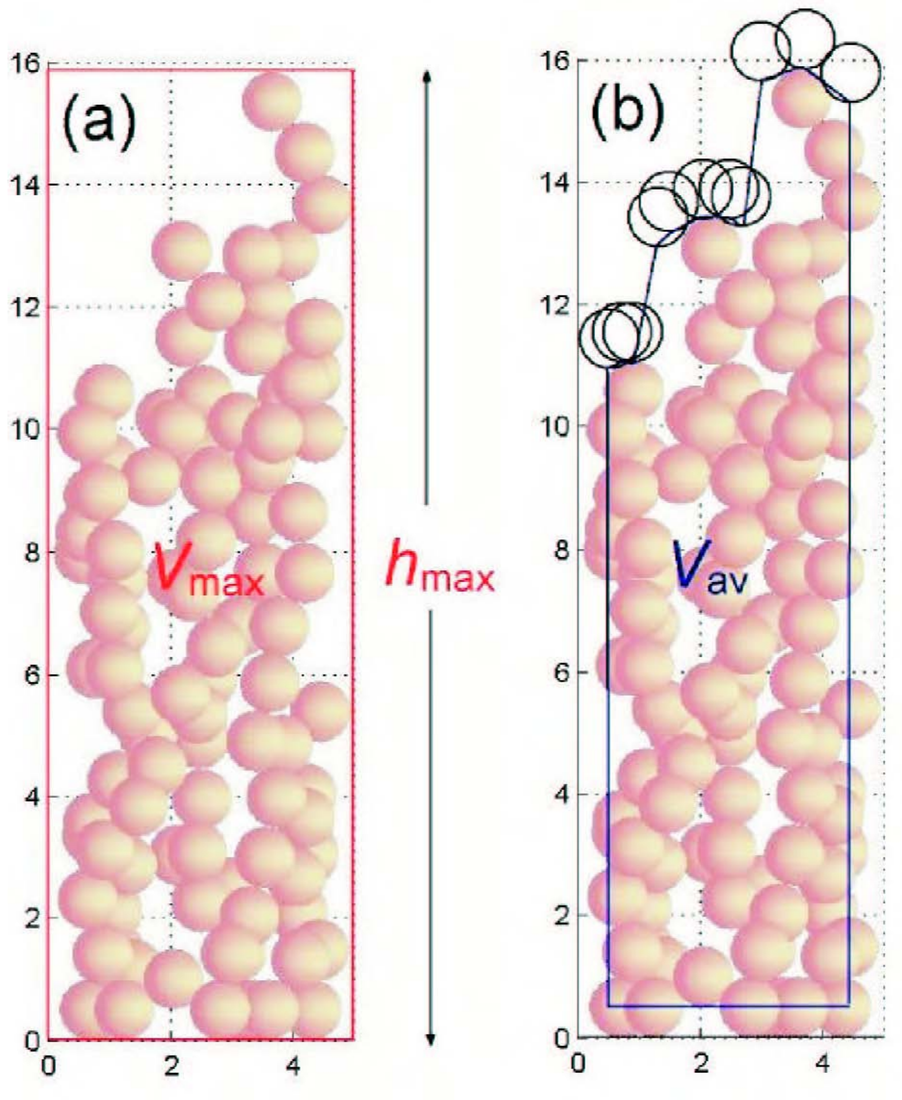

Figure 32: Illustration of definitions of layer thickness h: (a) Definition of maximal height h_{max}. (b) Definition of average Volume V_{av} by Monte Carlo probing of the surface.

η, the better the calculated value of porosity represents the bulk value. As η increases the upper and the lower bounds P_{max}, P_{av} of the porosity values "numerically converge" (Fig. 33). For

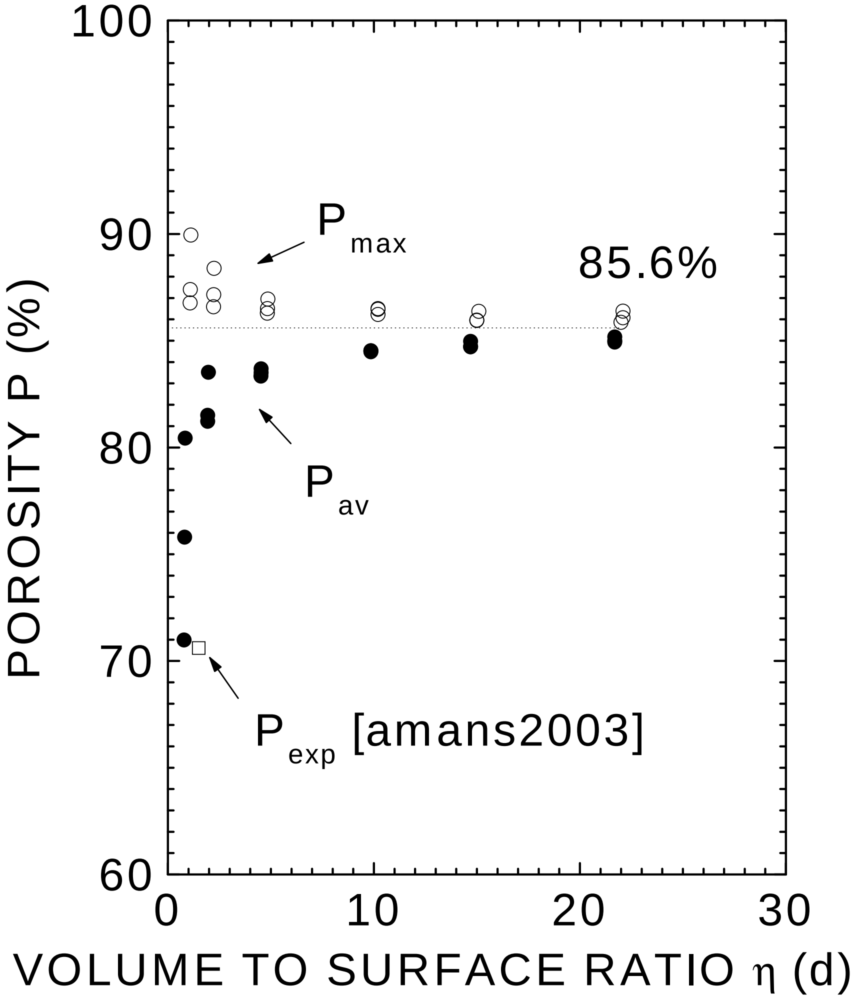

Figure 33: Porosities P_{max}, P_{av} from simulation in comparison with experimental value P_{exp} in variation with volume to surface ratio η. (Unit d is the Si-nc diameter).

$N = 10^6$ and $a = 100d$ ($\eta = 21.7d$) a porosity

$$P(\infty) = 0.856 \pm 0.008 \tag{34}$$

is obtained. Due to the small layer thickness $h_{exp} = (9 \pm 1)$ nm in the experiment [1] the experimental volume to surface ratio $h_{exp} = V/S = h_{exp}a^2/(2a^2 + 4ah_{exp}) \approx h_{exp}a^2/(2a^2) = h_{exp}/2 = 9\text{ nm}/2 = 1.5d$ (with $d = 3$ nm) is small (Fig. 33).

5.4 Discussion

The simulated porosity $P(\infty)$ departs from the experimental value P_{exp} by a difference $P(\infty) - P_{exp} = 0.856 - 0.706 = 0.15$, which we attribute to two reasons:

1. By the computer model the porosity $P(\infty)$ is overestimated, because it does not allow for spatial relaxation (increasing density of the film) due to vanishing surface mobility of arriving Si-nc.

2. The experimentally detected porosity P_{exp} is underestimated since in the current experiment the volume to surface ratio $\eta_{exp} = 1.5d$ is too small to yield reliable results for film thicknesses of only few (≈ 3) Si-nc diameters as chosen in the experiment.

As the layer thickness h_{exp} has been determined as an average value by AFM measurement in the experiment which corresponds to a Monte Carlo scanning of the surface in the simulation, one expects $h_{exp} \approx h_{av}$. So P_{av} should be a good approximation for experimentally determined porosities, even for small η. Actually the scatter of the simulated values $P_{av}(\eta \approx 0.8d)$ extends almost to P_{exp} (Fig. 33).

We note that compared to the porosities of simple cubic (0.48) and a close package like face centred cubic (0.26) the values $P(\infty)$, P_{exp} are both quite high.

5.5 Conclusions

Both, experiments and simulations show a high porosity of the thin films built from Si-nc, which supports the plausibility of the model. The difference of 0.15 between the simulated ($P(\infty) = 0.856 \pm 0.008$) and the experimental ($P_{exp} = 0.706$) value of porosity can to one part be attributed to discrepancy between the model and reality and to another part to a low volume to surface ratio ($h = 1.5d$) of the experiment. The actual bulk porosity P of the layers can be expected to lie somewhere between the two values:

$$P \approx 1/2\,(P(\infty) + P_{exp}) \approx 0.78. \tag{35}$$

6 Charge transport

6.1 Introduction

Charge transport through porous layers of Si-nc is highly complex. One has to consider transport through a network of interconnected Si-nc, of which the exact arrangement and structure of existing paths are unknown. In the easiest case one can assume that charges are transported through 1-dimensional channels, which are aligned parallel and connect the two metal contacts (Fig. 34). This is certainly a strong simplification of the percolative network of paths between the metal contacts, which is only applicable for sufficiently thick layers. In order to gain insight into the growth of Si-nc layers, we have recorded charge transport simultaneously with layer growth, which reveals the percolative nature of transport-paths in thin Si-nc layers. For a fundamental understanding of charge transport, measurements after completed deposition and at different grades of oxidation were performed as well. Corresponding to the two types of experiments,

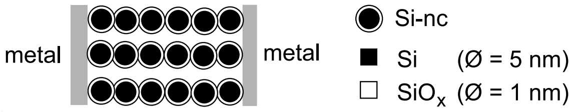

Figure 34: Rearrangement of Si-nc, which allows simpler calculations.

1. *In situ* charge transport during layer growth;
2. Charge transport after different grades of oxidation;

we expect different mechanisms governing charge transport:

1. Transport from Si-nc to Si-nc with minor importance of the Si-nc oxide shells;
2. Tunnelling from one Si-nc to the next through the Si-nc oxide shells.

6.2 *In situ* charge transport during layer growth

During the deposition of Si-nc layers charge transport has been measured (Fig. 35). As the deposition takes place in vacuum, at a pressure $p \approx 5 \cdot 10^{-5}$ mbar, it is assumed that no significant oxide shell is formed around the Si-nc.

It must be admitted that also at $p \approx 5 \cdot 10^{-5}$ mbar oxidation can take place; but we know that oxidation of the Si-nc surfaces even in ambient air takes place very slowly. According to [26] only after oxidation for some hours or days in ambient air the Si-nc surfaces are passivated by SiO_2 and PL can be observed. Oxidation of the Si-nc surface is finished after some months. According to the equation for an ideal gas the density of gas molecules is proportional to the pressure. If the composition of the gas mixture in the vacuum chamber is approximately the same as in the ambient air, the density of O_2 molecules and also of O radicals, is a factor of 2×10^7 smaller than in the atmosphere. So I assume that we can neglect the oxidation occurring in the vacuum chamber in the time-frame of hours.

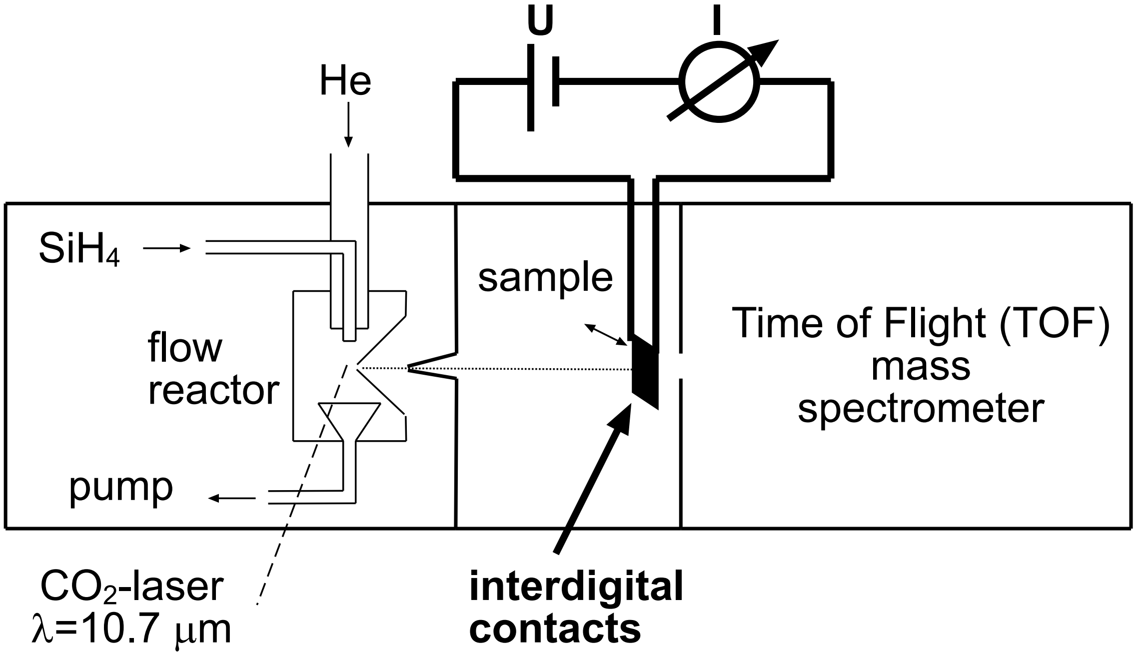

Figure 35: Set-up for charge transport measurements through Si-nc during layer growth.

6.2.1 Experimental

The current $I_{10\,\mathrm{V}}$ at a voltage $U = 10$ V was monitored during deposition of three samples as measured by a pico-ampere-meter (Präcitronic MV 40 DC-Milli-Pico-Meter). Deposition took place at RT and a pressure $p \approx 5 \cdot 10^{-5}$ mbar. The contact arrangement was coplanar; metal electrodes had been evaporated on the quartz substrates prior to deposition in an interdigital pattern (Fig. 36). Deposition parameters for the three samples have been similar. The Si-nc mean diameters and the layer thicknesses are listed in Tab. 11.

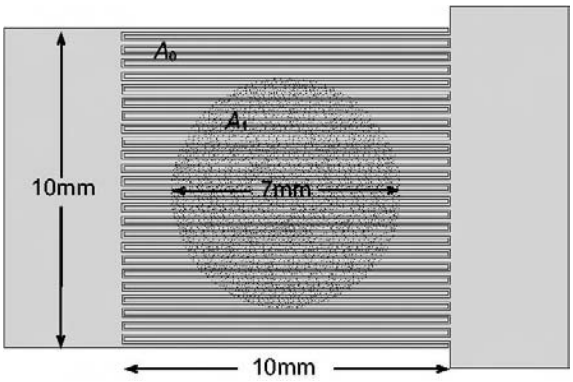

Figure 36: Interdigital contacts used for charge transport measurements. The gaps between the electrode fingers were $L = 60\ \mu$m, total contact length was 500 mm.

To compare the experimental results with computer simulations the description is based on the areal density D of Si-nc rather than the layer thickness h. Especially for small areal densities the layer thickness h is a rather undefined magnitude, due to the granular structure of the Si-nc

Sample name	d_{PL} (nm)	λ_{max} (nm)	h (nm)
GO_52	5.8	828	490
GO_54	6.0	838	530
JO_62	6.1	842	$<$ 2900 (inhomogeneous)

Table 11: Si-nc diameters d_{PL} determined from PL peak wavelengths λ_{max} and layer thickness h.

layers. The transformation of the two quantities is illustrated in Fig. 37. We assume that N Si-nc with diameter d occupy an area A and fill it up to a height h. Let P denote the layer porosity, which is defined as the ratio of the empty volume to the total volume. Now the volume occupied merely by the Si-nc without the space in between can be calculated in two ways:

$$N \cdot \frac{4}{3}\pi(\frac{d}{2})^3 = A \cdot h(1-P).$$

For the layer porosity we assume the arithmetic mean value

$$P \approx 0.78 \tag{36}$$

of the experimentally determined porosity $P_{exp} = 0.706$ [1] and the bulk value $P(\infty) = 0.856$, Eq. (34), obtained by computer simulations. As described in Sections 5.4, 5.5 this value approximates the real bulk porosity. And here we are interested in the bulk porosity, because the layer thicknesses of the samples (Tab. 11) are large enough, that the porosities are very close to bulk at the end of a deposition. We calculate the Si-nc areal density

$$D := \frac{N}{A} = \frac{1-P}{\frac{4}{3}\pi(\frac{d}{2})^3} \cdot h = \frac{6(1-P)}{\pi} d^{-2} \cdot (\frac{h}{d}) = 0.42(\frac{h}{d})d^{-2}. \tag{37}$$

The layer thickness h was assumed to be proportional to the recorded deposition time. After measurement of the total layer thickness after the deposition, we could therefore calculate the layer thickness at every time during deposition and via (37) the Si-nc areal density D was determined.

6.2.2 Results

The conductance $G = \frac{I}{U}$ in dependence on the Si-nc areal density D showed three regions (Fig. 38):

I: $G_I(D) \approx 0$,
II: $G_{II}(D)$ increases non-linearly,
III: $G_{III}(D) = const \cdot \Delta D$ (linear increase).

Within regime II a range is found with super-linear increase

$$G_{IIa}(D) = G_0 \cdot D^{B_{exp}} \tag{38}$$

with exponent $B_{exp}(\text{JO\_62}) = 1.62 \pm 0.03$. This range is marked by a rectangle in Fig. 38(a). Fig. 38(b) shows a zoom in this region with measurements and power law fits of all three samples. The mean value of the 3 exponents is $\overline{B_{exp}} \approx 1.5$.

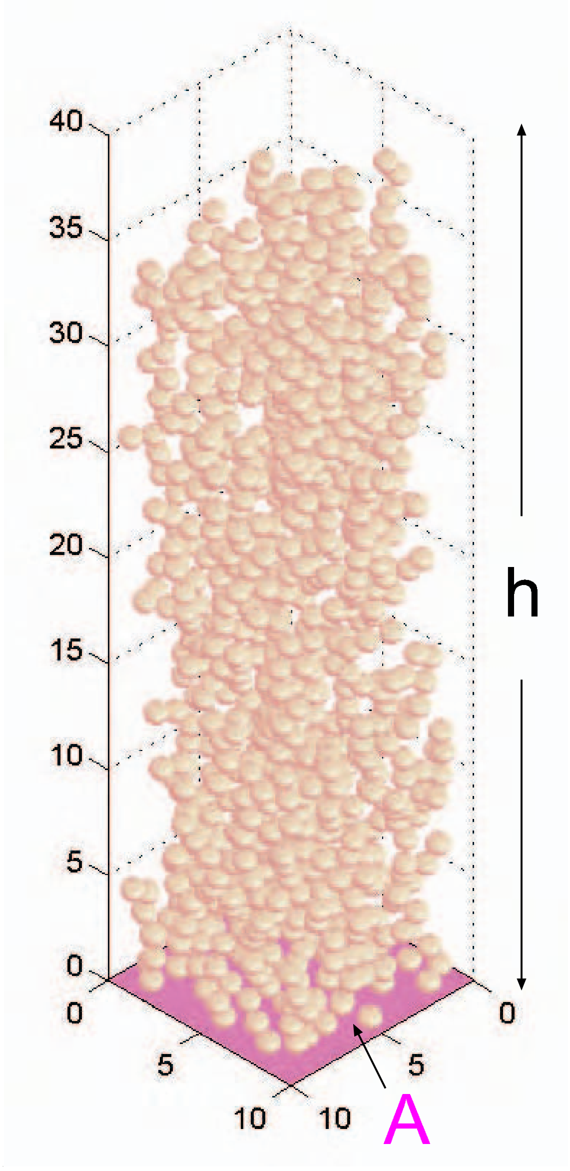

Figure 37: Illustration for the calculation of Si-nc areal density *D* vs. layer thickness *h*.

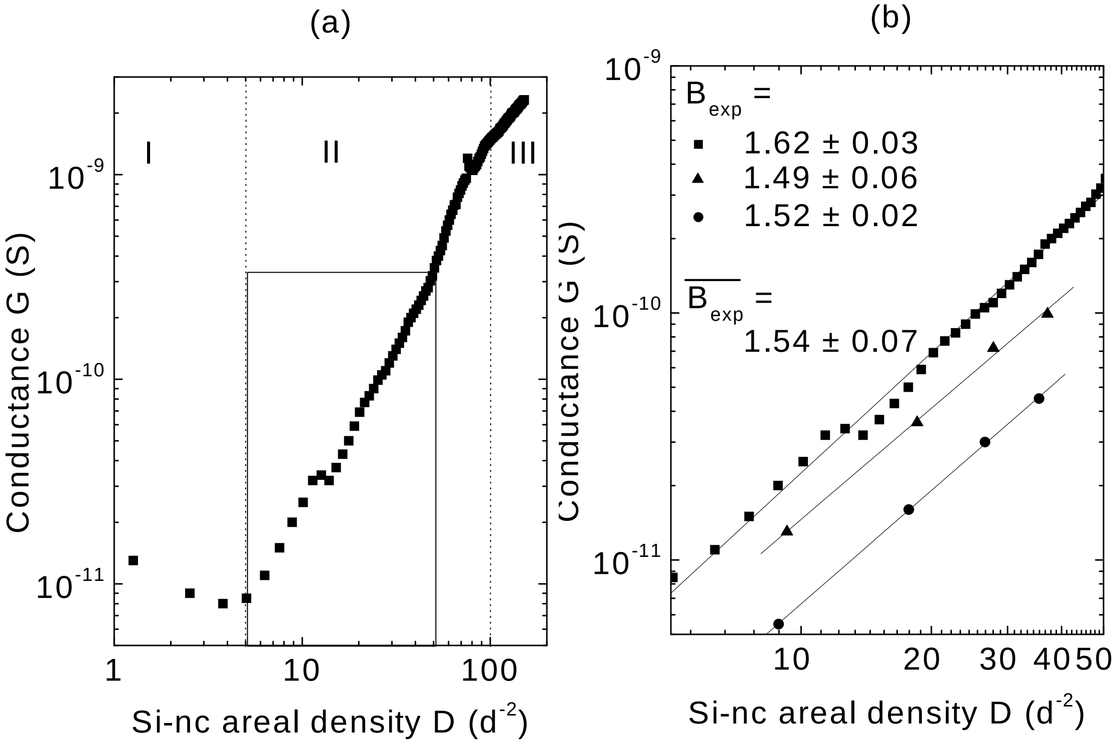

Figure 38: (a) Conductance monitored during deposition (sample JO_62, monitoring time 2h). Rectangle within regime II marks region of increase according to a power law. (b) Zoom in region marked by rectangle in (a); also shown are the conductances recorded on samples GO_52 (circles), GO_54 (triangles). Solid lines are fits according to power law (38).

6.2.3 Qualitative model

The charge transport during film growth can be explained qualitatively by a “three layer” model (Fig. 39). Each “layer” corresponds to one of the three regimes described in Fig. 38 such that G consists of three contributions:

I: $G_I = 0$: No paths of Si-nc between contacts built,

II: G_{II} : non-linear increase due to percolation near Si-nc layer/substrate interface and near Si-nc layer surfaces,

III: $G_{III} = const \cdot \Delta D$: linear increase, because percolation near interface and surface is negligible compared to contribution of bulk.

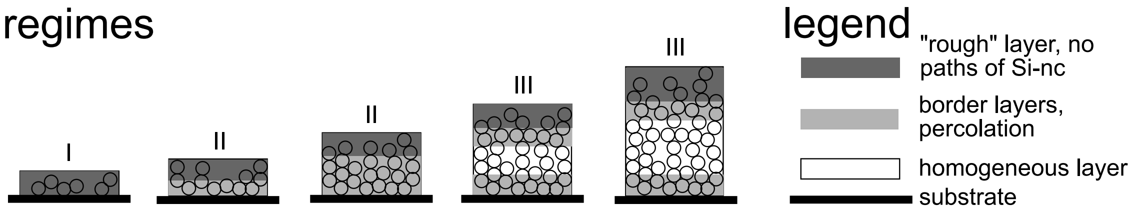

Figure 39: Qualitative model for charge transport during layer growth.

The separation between the “layers” is not abrupt, but smooth. This applies especially to the transition between the “layer” corresponding to the regimes II and III.

6.2.4 Simulations

Monte-Carlo computer simulations have been carried out to reproduce some of the main features found in experiments of charge transport during layer growth. The model for the simulation of the layer growth has already been described in Sec. 5.2. Additionally we assume here:

1. Charge carriers can only tunnel between two Si-nc for distances lower than a critical tolerance value d_{tol}.

Two types of simulations have been performed: “first contact simulations” and “simulations of connections”.

First contact simulation The simulation is performed until a contact between two metal electrodes is achieved *via* a path of Si-nc. The base area in the simulations is composed of a square with side length $d_{gap} = (9\ldots300)d$, enclosed by two rectangles with areas $(d_{gap}/3) \times d_{gap}$ representing the metal electrodes. The computer algorithm to check for the first contact is a kind of paint fill algorithm; all Si-nc touching one of the two metal electrodes (magenta, cyan) within the tolerance d_{tol} are painted in red and blue colour respectively (Fig. 40). Si-nc touching red/blue Si-nc within d_{tol} are painted in the same colour. As soon as one Si-nc “owns both colours red and blue”, the first contact is established. The Si-nc areal density at this moment is denoted by D_{1c}.

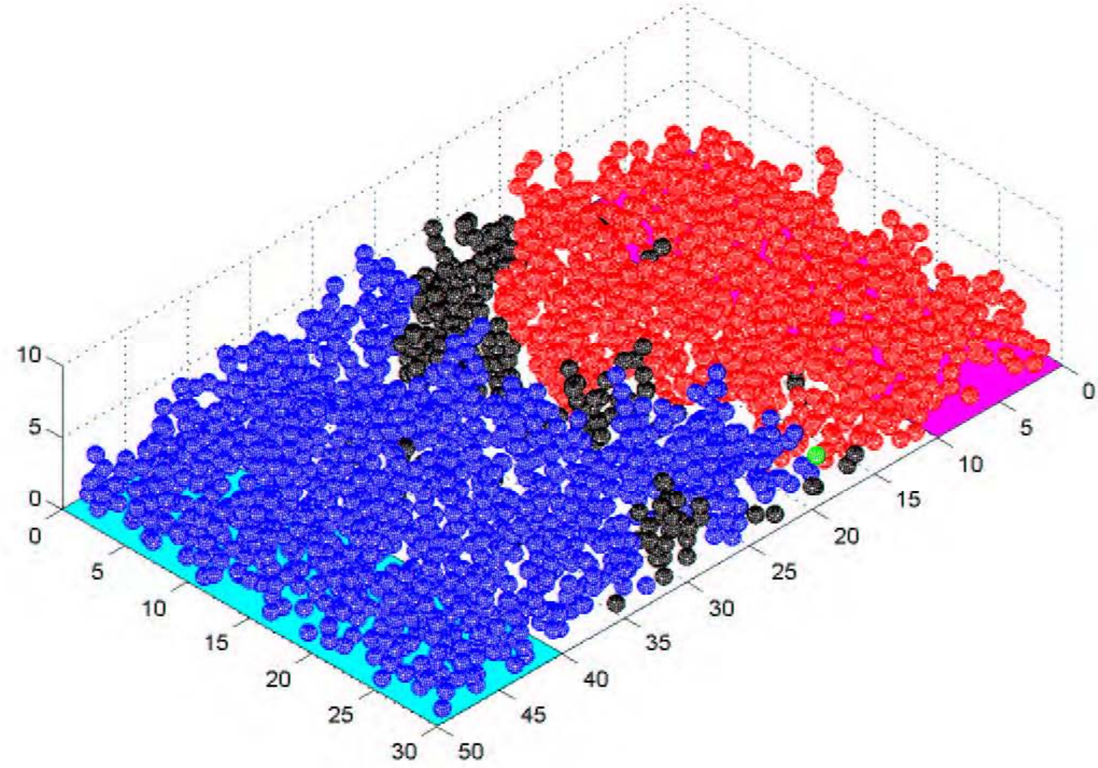

Figure 40: Arrangement of Si-nc at the moment of the first contact. $d_{tol} = \frac{1}{3}d$, $d_{gap} = 30d$. Lengths are given in units of the Si-nc diameters d.

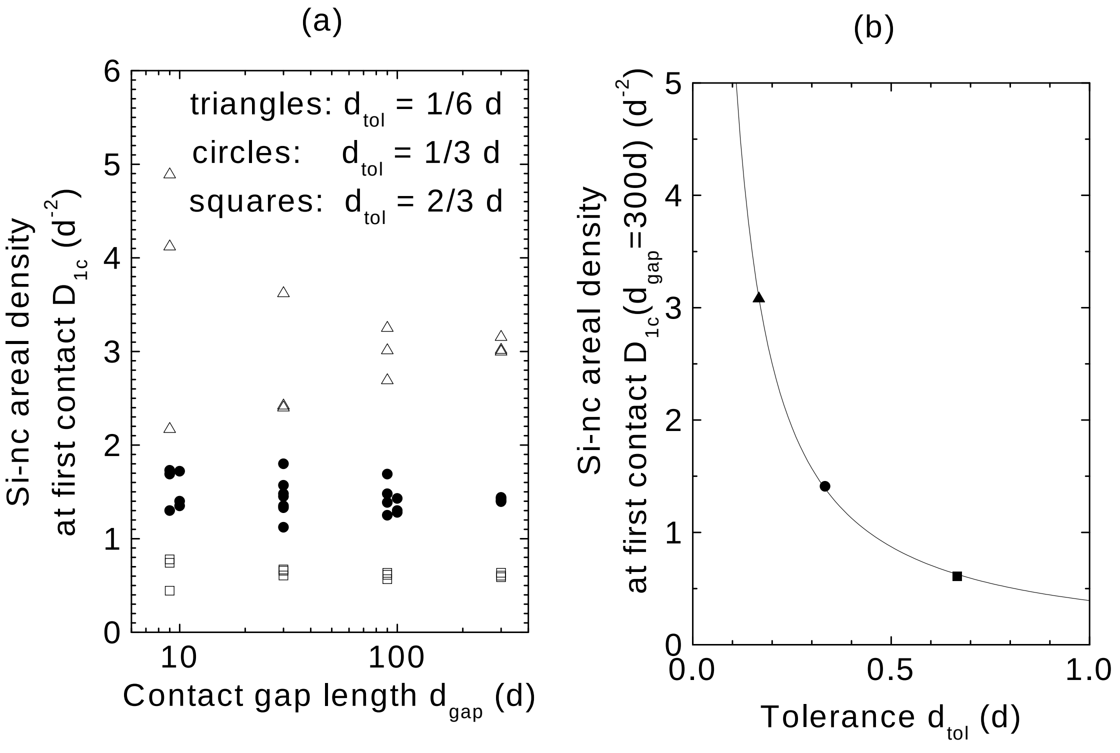

Figure 41: Results of first contact simulations. (a) Si-nc areal density D_{1c} in dependence on contact gap d_{gap} for 3 values of tolerance parameter d_{tol}. For each value of d_{gap} and each tolerance parameter d_{tol} three simulations have been performed. (b) Limit values of D_{1c} for $d_{gap} = 300d$ in dependence on d_{tol}. The dotted line is a fit according to a power law.

Results of first contact simulation The density D_{1c} at the first contact strongly depends on the parameter d_{tol} (Fig. 41(a), (b)). For small contact gap lengths d_{gap} the scatter in the 3 simulations which have been performed for each value of the tolerance parameter d_{tol} is significant. For increasing contact gap lengths d_{gap} the areal densities D_{1c} "numerically converge" for each value of d_{tol} separately. For $d_{gap} = 300d$ we yield the values displayed in Tab. 12. These limit values are plotted in Fig. 41(b) versus the tolerance parameter d_{tol}. With increasing d_{tol} the areal density $D_{1c}(300d)$ decreases hyperbolically. A least square fit yields the power law $D_{1c}(d_{gap} = 300d)(d_{tol}) = 0.393d^{-2} \cdot (d_{tol}/d)^{-1.15}$.

d_{tol} (d)	$D_{1c}(d_{gap} = 300d)$ (d^{-2})
$1/6$	3.08 ± 0.80
$1/3$	1.41 ± 0.02
$2/3$	0.61 ± 0.04

Table 12: Densities at moment of first contact D_{1c} in dependence on tolerance parameter d_{tol}.

Discussion The simulated areal densities $D_{1c}(d_{gap} = 300d)$ are smaller than the value $D \approx 5d^{-2}$ at which the onset of the conductance occurs in the experiment (Fig. 38). This difference can be partly attributed to the measurement accuracy. The precision of the current measurement is $\Delta I \approx 10^{-12}A$, such that the precision of the conductance should be $\Delta G \approx \frac{\Delta I}{U} \approx 10^{-13}S$. But the deposition of Si-nc influences the current measurement such that the accuracy becomes $\Delta G \approx 10^{-11}S$, which can be observed by an increase of G by $\approx 10^{-11}S$ right at the start of the deposition. Probably ions generated by decomposition of SiH_4 or charged Si-nc contribute to the total electrical current. So we conclude that the value of the onset of the conductance versus the areal density cannot be deduced from our experiment. Another feature is the ambiguity of D_{1c} due to the choice of the tolerance parameter d_{tol}.

A more detailed simulation should include the properly calculated quantum mechanical tunnelling currents through the oxides and the gaps between two adjacent Si-nc. This approach is very complicated to be accomplished in a large scale simulation and lies therefore outside the scope of this PhD thesis.

Simulation of connections In order to describe the increase of the conductance after the first contact I pursued an approximate *ansatz* [8]. The computer simulation starts with a "first contact simulation" (see previous paragraph). When the first contact is established, the last Si-nc is removed. Then the simulation is continued till a contact occurs the second time. Again the last Si-nc is removed, and the simulation is continued. This cycle is performed several times. Fig. 42 shows a screen-shoot after 10 cycles where the Si-nc establishing the contacts have been coloured in green colour. (They have been removed in the simulation, but are nevertheless drawn in the figure.)

Under certain circumstances the number N_c of established connections at a given moment during deposition is a measure for the conductance of the layer. In Fig. 42 one observes that at the 10th connection almost the entire area is coloured either red or blue. The green coloured Si-nc, establishing the 10 connections, lie all in a line separating the red coloured Si-nc from the blue ones. We assume that the connections between the Si-nc in a single coloured area are numerous, such that the main resistance will occur at the green painted Si-nc connecting the differently coloured areas of Si-nc. Therefore an equivalent circuit diagram shown in Fig. 43

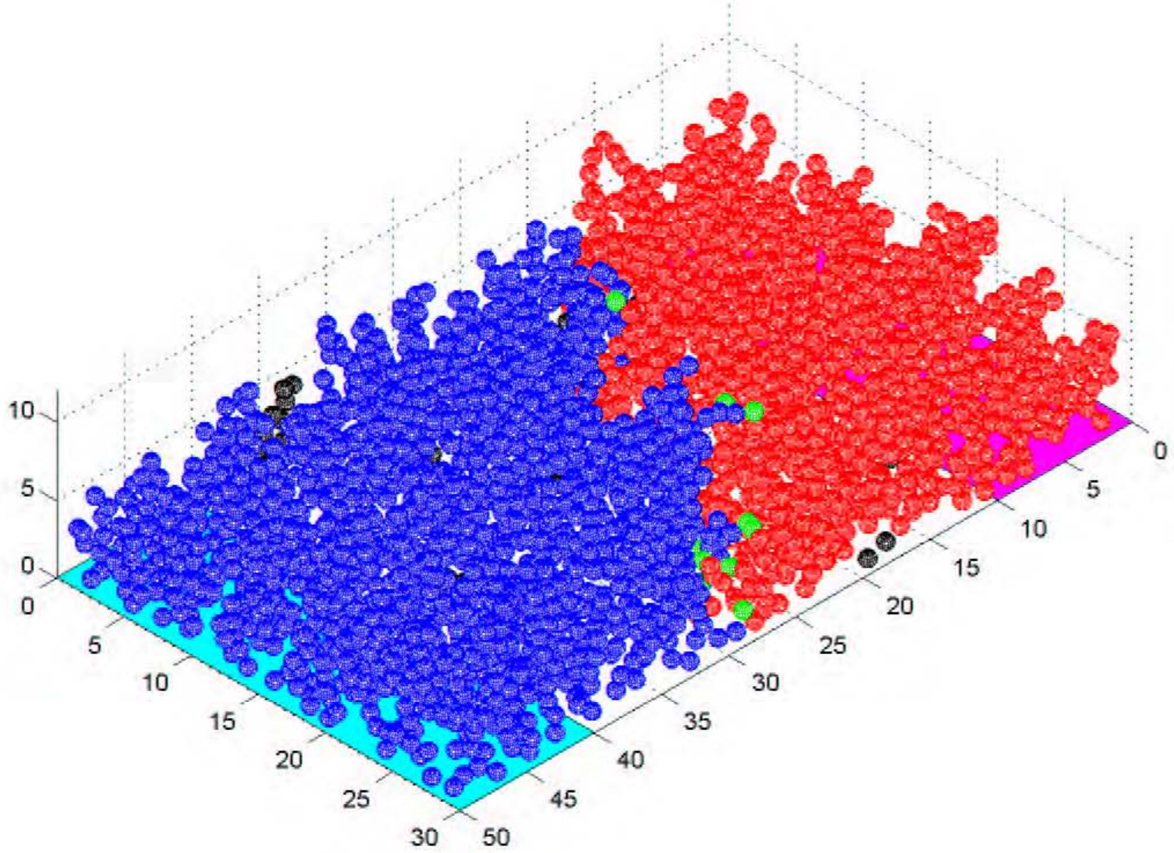

Figure 42: Arrangement of Si-nc at the moment when a contact between the two metal electrodes has been established for the 10th time. $d_{tol} = \frac{1}{3}d$. Lengths are given in units of the Si-nc diameters d.

can be applied. The “green” Si-nc occupy bottleneck positions and provide for conductances G_1, G_2, G_3... G_{N_c}. The mean conductance between the left (right) metal contact and the “green” Si-nc is denoted by G_L (G_R). With the assumption

$$G_L,\ G_R \gg G_1 = G_2 = G_3 = ... = G_0$$

one obtains a total conductance

$$G \approx G_1 + G_2 + G_3 + ... = N_c \cdot G_0.$$

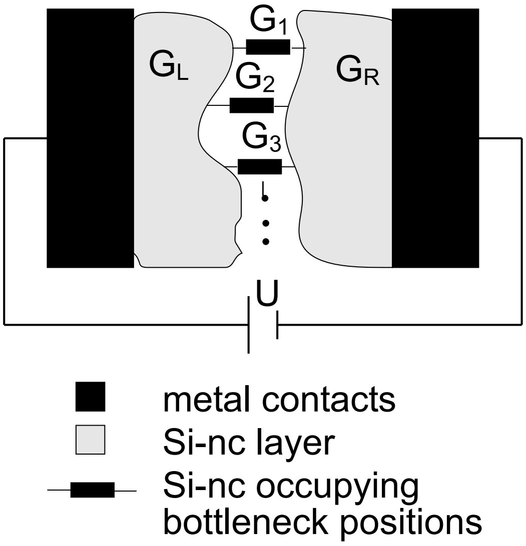

Figure 43: Equivalent circuit diagram representing a “bottleneck model”.

Results of simulations of connections 18 runs have been performed, each with a total number of $N_c = 50$ connections (Fig. 44). As the scatter between the experiments is still quite high at the scale the experiments have been performed ($d_{gap} = 30d$, $d_{tol} = \frac{1}{3}d$), some kind of averaging has to be applied to the results. For that purpose we calculated the arithmetic mean of the 18 Si-nc areal density values D for each value of calculated number of connections N_c. The resulting average curve can be fitted by an expression

$$N_c = N_{c0} \cdot (D - D_0)^{B_{sim}},$$

with the fit parameters N_{c0}, D_0, B_{sim} given in Fig. 44.

Discussion The fit parameter $B_{sim} = 1.35 \pm 0.03$ agrees fairly well to the experimental mean value $\overline{B_{exp}} = 1.54 \pm 0.07$. In the fit to the simulated data, however, a shift parameter D_0 has to be included, whereas in the fit to the experimental data it is not needed. But one has to remember, that measurement noise is involved in the conductance measurements shown in Fig. 38. If one subtracts a conductance off-set $\Delta G = 8 \times 10^{-12}$ S from the measurement on sample JO_62, also a shift parameter D_0 is needed to perform a power law fit (Fig. 45).

In the following the ***achievements*** of simulations according to the bottleneck model (Fig. 44) are listed and the ***limits of the model*** are outlined:

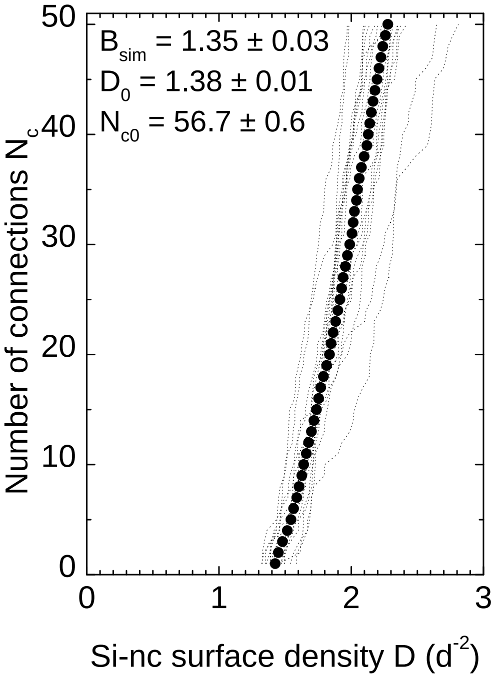

Figure 44: Results of simulation of connections. Dotted lines: simulations. Circles: average curve of all 18 simulations. Parameters: $d_{tol} = \frac{1}{3}d$, $d_{gap} = 135d$. Fit results of average curve according to $N_c = N_{c0}(D - D_0)^{B_{sim}}$.

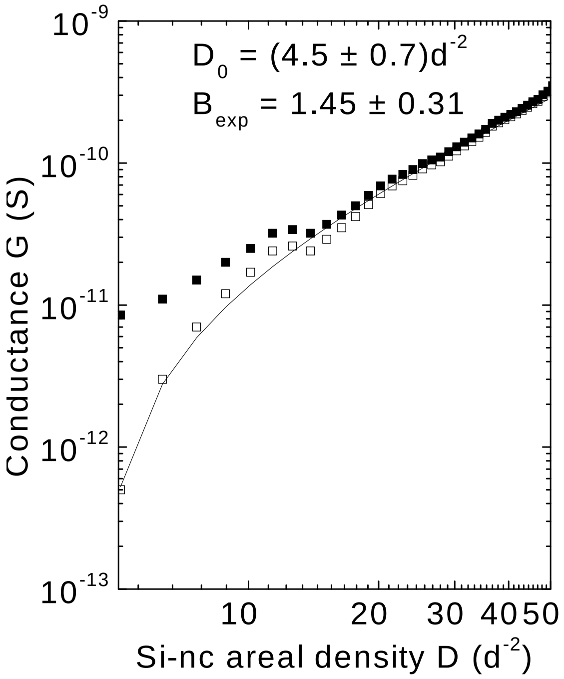

Figure 45: Solid squares: original conductance measurement (sample JO_62). Open squares: noise value $\Delta G = 8 \times 10^{-12}$ S subtracted. Solid line: fit according to shifted power law $G = G_0 \cdot (D - D_0)^{B_{exp}}$.

Achievements

- Non-linear increase according to power law in regime II of simulations.
- *Shifted* power law adequately describes $G(D)$ relation in regime II as well for simulations as for experiment.

Limits of model

- Tunnelling is not directly included in simulations.
- Relation $N_c(D) \sim G(D)$ is inappropriate for large D.
- Transport through network not only through Si-nc bottleneck positions has to be regarded in real Si-nc structures.

One might argue that tunnelling is not included in the model, although tunnelling could be the dominant charge transport mechanism in thin layers of Si-nc. There are two reasons, which justify to omit tunnelling. First deposition takes place in vacuum, thus the SiO_2 layers around the Si-nc might be negligibly thin. One would rather expect charge transport as a kind of scattering process than tunnelling. Second, it will be shown in Section 6.3, that the tunnelling current through a structure composed of a series of SiO_2 barriers in a broad range depends linearly on the applied voltage. Hence a tunnelling junction can be replaced by an Ohmic resistance in this case, which complies with the model.

Conclusions We achieved qualitative agreement between a model and the measurements. The measured Si-nc areal density at first contact does not agree with the simulations. Although $B_{sim} = 1.38 \pm 0.03$ agrees fairly well with the experimental mean value $\overline{B_{exp}} = 1.54 \pm 0.07$ the scale of simulation of connections is too small to make decisive statements about the exponent B_{sim}. Note that the range of Si-nc surface density in experiments is $D_{exp} = (0 \ldots 200)d^{-2}$, whereas in the simulation only values $D_{sim} = (0 \ldots 3)d^{-2}$ are reached. Although the scale of the simulations, limited by the memory capacities of the used computer and my life-time, are rather small in scale compared to the experiments, the simulations provide some understanding for the mechanisms of charge transport during layer growth.

6.3 Tunnelling through Si-nc oxide shells

After sufficient long exposure of the Si-nc layers to ambient air, the single Si-nc will be overcoated by SiO_2 oxide layers. Thus charge carriers have to surmount barriers, consisting of these oxide layers (Fig. 46). The form of the oxide barrier between two adjacent Si-nc is complex and not exactly known and can most easily be approximated as a disc. We will even apply a more simplified model and assume a barrier in the calculations below, which corresponds to a disc expanded to infinity. In the following theoretical considerations we will assume that only electrons contribute to the total current. The contribution of holes is neglected here. Nevertheless the formalism can be easily translated into the situation where holes are the majority current carriers. A possibility for the electrons to cross the barriers, is tunnelling. In the following the consequences of tunnelling for the electrical transport will be described.

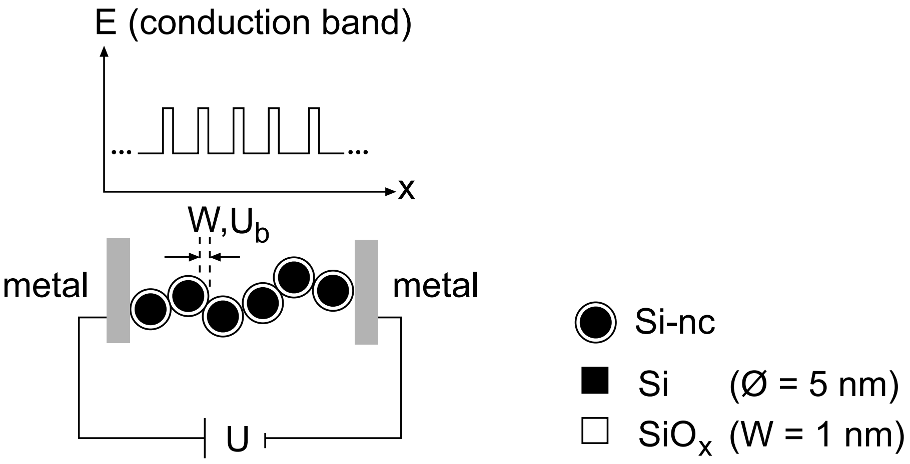

Figure 46: Oxide layers overcoat each Si-nc, yielding barriers of width W between adjacent Si-nc cores. U_b is the part of the applied voltage U dropping at each oxide barrier.

6.3.1 Theory

Tunnelling probability According to [23] the probability $T(E)$ of an electron to tunnel through a rectangular barrier, as drawn in Fig. 47, is

$$T(E) = \left| \frac{e^{-ikW}(1-\Phi^2)}{e^{KW} - \Phi^2 e^{-KW}} \right|^2 = \frac{1}{1 + \frac{1}{16} \cdot \frac{V^2}{E(V-E)} \left(e^{KW} - e^{-KW}\right)^2} \tag{39}$$

$k := \frac{(2m^* E)^{1/2}}{\hbar}$	wave vector outside barrier,
$K := \frac{(2m^*(V-E))^{1/2}}{\hbar}$	“ inside “,
$\Phi := \frac{K+ik}{K-ik}$	subsidiary variable,
m^*	effective mass.

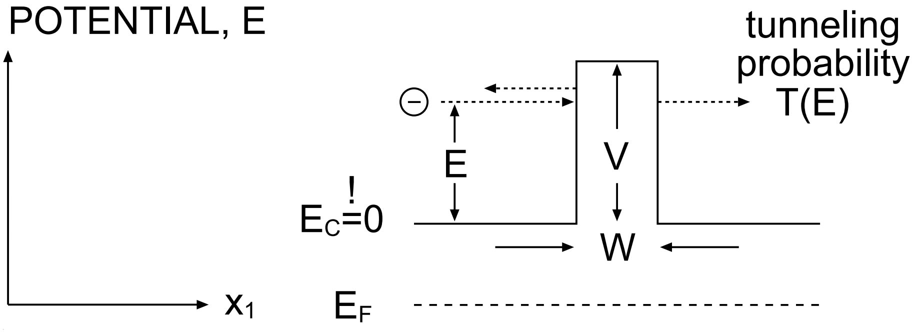

Figure 47: 1-dimensional square barrier, height V, width W. Conduction band edge E_C is chosen as zero point of energy.

For small energies, $E \ll V$ or more exactly $KW \gg 1$, the tunnelling probability can be approximated as

$$T(E) \approx 16 \cdot V^{-2}(V-E)E\exp(-2KW). \tag{40}$$

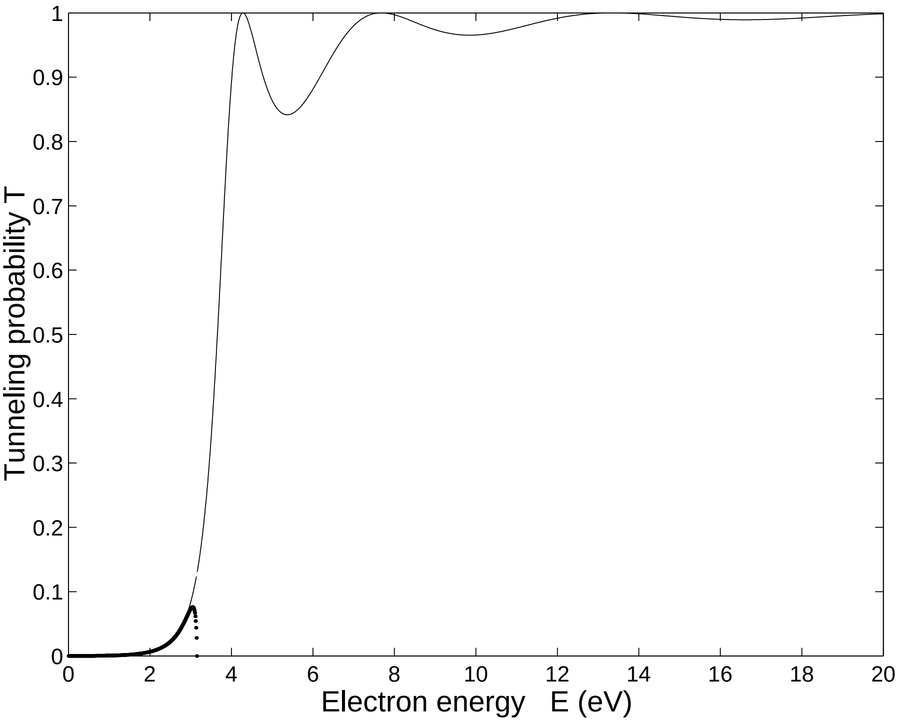

$V = 3.15$ eV	barrier height
$W = 10^{-9}$ m	barrier width
$m^{*} = 0.33 \cdot 9.1 \cdot 10^{-31}$ kg	effective density of states mass of conduction band

Figure 48: Tunnelling probability $T(E)$ through a square barrier for the given parameters. Dots show approximation according to (40).

Fig. 48 exemplarily shows $T(E)$ in the region $E = 0 \dots 20\,\text{eV}$ for electrons, which tunnel through a SiO_2 barrier in c-Si. In this example approximation (40) is valid up to energies $E \lesssim \frac{3}{4}V \approx 2.5$ eV.

While in the 1-dimensional case electrons only have velocities in one direction, in 3 dimensions the components in all three directions of space are present. For a 3-dimensional rectangular barrier (Fig. 49),

$$V_{3d}(x_1, x_2, x_3) := V_{1d}(x_1) := \begin{cases} 0 & x_1 < 0 \\ V & 0 < x_1 < W \\ 0 & W < x_1 \end{cases},$$

the stationary Schrödinger-equation (S-Eq) reads

$$-\frac{\hbar^2}{2m^*}\nabla^2\varphi + V_{3d}\varphi = E\varphi,$$

where the periodic lattice potential of the semiconductors is accounted for by the effective mass m^*. Rigorously the effective masses are different outside the barrier (Si) and inside (SiO_2), which we will neglect in the following treatment. An *ansatz* of separation

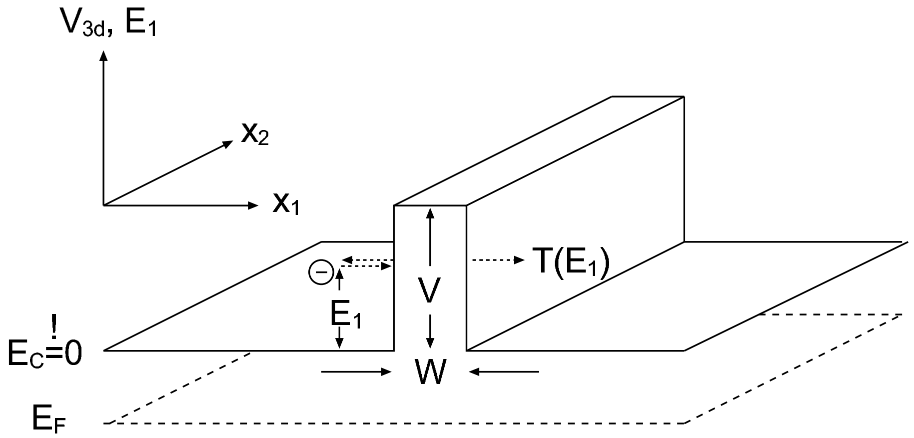

Figure 49: 3-dimensional rectangular barrier of height V and width W. (Third spacial coordinate x_3 is left out in figure.)

$$\varphi(x_1, x_2, x_3) = \varphi_1(x_1) \cdot \varphi_2(x_2) \cdot \varphi_3(x_3)$$

yields solutions

$$\varphi(x_1, x_2, x_3) = C \cdot \varphi_1(x_1) \cdot e^{i(k_2x_2 + k_3x_3)}.$$

Here φ_1 is the solution of the 1-dimensional problem with S-Eq

$$-\frac{\hbar^2}{2m^*}\varphi_1'' + V_{1d}\varphi_1 = E_1\varphi_1, \tag{41}$$

C is a constant and $e^{i(k_2x_2+k_3x_3)}$ represents a solution of the S-Eq

$$-\frac{\hbar^2}{2m^*}\varphi_i'' = E_i\varphi_i \ (i = 2, 3)$$

for plane waves. Thereby

$$k_i = \frac{(2m^* E_i)^{1/2}}{\hbar} \ (i = 2,3).$$

The total energy E is composed of three parts

$$E = E_1 + E_2 + E_3, \tag{42}$$

representing the kinetic energies in x_1-, x_2-, x_3-direction. As only φ_1 varies in direction perpendicular to the barrier (= x_1-direction), only the energy component E_1 is relevant for the tunnelling probability. The tunnelling probability reads (39) analogously as in the 1-dimensional case, if only E is replaced by E_1.

In the calculation of the tunnelling current density the decomposition of the kinetic energy in 3 independent parts has the following consequences:

- The tunnelling probability only depends on E_1.
- In the energy schemes one only considers the energy part E_1 in comparison with the electronic potential. (Such the correct limits of the velocity component v_1 in x_1-direction are found for the integrals.)

Tunnelling current density In the following the tunnelling current density through a barrier as shown in Fig. 49 will be calculated. Firstly the partial current is calculated, which flows in thermal equilibrium through the barrier in one direction. In thermal equilibrium no total current flows at all. The situation can, however, be equivalently described by equally large tunnelling currents flowing in opposite directions, resulting in a vanishing total current. Secondly we consider the barrier under *bias* voltage U. By the voltage drop induced asymmetry the partial current in one direction increases, while the current in opposite direction decreases, which results in non-vanishing total current.

Thermal equilibrium We yield the current density $J_{\rightarrow}$ from the left side of the barrier to the right side by integration in velocity space. Here we assume an isotropic dispersion relation $E = \frac{1}{2}m^*\mathbf{v}^2$ with density of state effective mass m^*. From the well-known expression $z_\mathbf{k} = \frac{2}{8\pi^3}$ for the density of states in wave vector space and by the relation $\mathbf{v} = \frac{\hbar}{m^*}\mathbf{k}$ the density of states $z_\mathbf{v} = \frac{m^{*3}}{4\pi^3\hbar^3}$ in velocity space is obtained. Occupation of the states follows Fermi-statistics, i. e. the occupation probability of a state at energy E equals $f(E) = \frac{1}{\exp(\frac{E-E_F}{kT})+1}$. The current density $J_{\rightarrow}$ is composed of infinitesimal contributions $dJ_{\rightarrow} = \nu \cdot e \cdot dn \cdot v_1 \cdot (1 - f(E))$, where the factor $\nu = 6$ accounts for the 6 minima found in the band structure of silicon and $dn = z_\mathbf{v} f(E) T(\frac{1}{2}m^*_{dc}v_1^2) dv_1 dv_2 dv_3$ denotes the part of the electrons approaching the barrier ($v_1 > 0$) and succeeding in tunnelling through it. The factor $(1 - f(E))$ represents the the probability of a state at energy E at the other side of the barrier being unoccupied . In total one yields

$$\begin{aligned} J_{\rightarrow} &= \int_{-\infty}^{+\infty} dv_3 \int_{-\infty}^{+\infty} dv_2 \int_{0}^{+\infty} dv_1 \nu \cdot e \cdot z_{\mathbf{v}} \cdot f(E)\,(1-f(E))\,T(\frac{1}{2}m_{dc}^{*}v_1^2)v_1 \\ &\approx \int_{-\infty}^{+\infty} dv_3 \int_{-\infty}^{+\infty} dv_2 \int_{0}^{+\infty} dv_1 \nu \cdot e \cdot z_{\mathbf{v}} \cdot f(E)T(\frac{1}{2}m_{dc}^{*}v_1^2)v_1 \\ &= \nu \cdot e \cdot z_{\mathbf{v}} \int_{0}^{+\infty} dv_1\, v_1 T(\frac{1}{2}m_{dc}^{*}v_1^2) \int_{0}^{+\infty} 2\pi v_{23} dv_{23} f(E). \end{aligned}$$

In the first step $1-f(E) \approx 1$ has been approximated, because we focus on non-degenerate semiconductors with $E_C \gg E_F$ and we deal with energies $E > E_C$. In the second step v_2 and v_3 have been substituted by the radial variable $v_{23}^2 := v_2^2 + v_3^2$. Further substitution, $E_1 := \frac{1}{2}m_{dc}^{*}v_1^2$, $E_{23} := \frac{1}{2}m_{dc}^{*}v_{23}^2$, yields

$$J_{\rightarrow} = \nu \cdot 4\pi e m^{*} h^{-3} \int_{0}^{+\infty} dE_1 \left[T(E_1) \int_{0}^{+\infty} dE_{23} f(E_1 + E_{23}) \right].$$

In Boltzmann-approximation ($f(E) \approx \exp(-\frac{E-E_F}{kT})$) this simplifies to

$$J_{\rightarrow} \approx \nu \cdot 4\pi e m^{*} h^{-3} kT \exp(\frac{E_F}{kT}) \int_{0}^{+\infty} dE_1 \exp(-\frac{E_1}{kT})T(E_1). \tag{43}$$

The integrand

$$g(E_1) := \exp(-\frac{E_1}{kT})T(E_1) \tag{44}$$

shows a maximum at $E_1 \approx 0.025\text{eV} = kT$ for barrier height $V = 4.5$ eV, width $W = 1$ nm and effective mass $m^{*} = 0.50 \cdot 9.1 \times 10^{-31}$ kg at room temperature (Fig. 50). This means, the contributions to the tunnelling current mainly stem from electrons with energies $E_1 \approx 0.025$ eV near the conduction band edge $E_C := 0$, which are much smaller than the barrier height V. The above mentioned issue, that $g(E_1)$ is maximal at $E_1 \approx kT$ can be theoretically derived. The integrand is approximately

$$g(E_1) \approx 16 \exp(A(E_1))\,(V-E_1)\,E_1 V^{-2}, \tag{45}$$

with $A(E_1) := -\frac{E_1}{kT} - 2^{3/2} m^{*1/2} \hbar^{-1} W\,(V-E_1)^{1/2}$. We yield the derivative

$$\begin{aligned} g'(E_1) &\approx 16V^{-2}\exp(A(E_1))\left\{A'(E_1)\,(V-E_1)\,E_1 + (V-2E_1)\right\} \\ &= 16V^{-2}\exp(A(E_1))\left\{\left(-k^{-1}T^{-1} + 2^{1/2}m^{*1/2}\hbar^{-1}W \cdot F^{-1/2}\right)F \cdot E_1 + F - E_1\right\} \end{aligned} \tag{46}$$

with the abbreviation $F := V - E_1$. The integrand $g(E_1)$ is maximal at energy E_{max} with $g'(E_{max}) = 0$, which is equivalent to

$$E_{max}^{-1} = k^{-1}T^{-1} + 2^{1/2}m^{*1/2}\hbar^{-1}W \cdot F^{-1/2} - F^{-1}.$$

For the above parameters

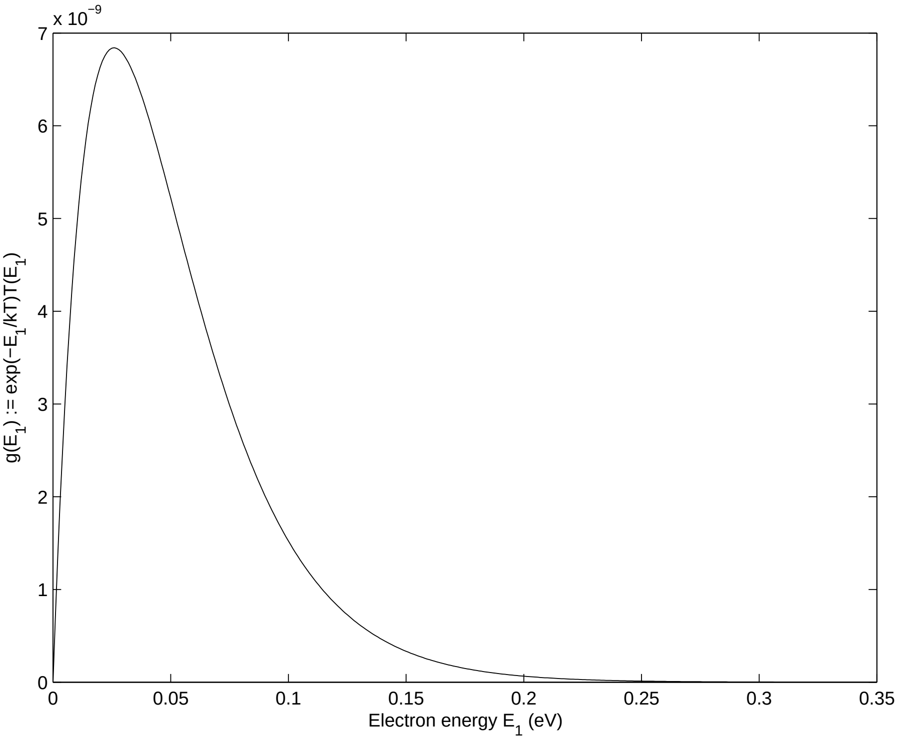

Figure 50: Integrand $g(E_1)$ from (44) for the parameters listed in text at RT.

$$
\begin{aligned}
F \approx 4.475\text{ eV} &\gg kT, \\
\left(F \cdot \frac{\hbar^2}{2m^* W^2}\right)^{1/2} \approx 0.58 &\gg kT,
\end{aligned}
$$

and therefore we yield

$$E_{max} \approx kT.$$

It is worthwhile to note, that by no means the exponential factor

$$\exp\left(-2^{3/2} m^{*1/2} \hbar^{-1} W \left(V-E\right)^{1/2}\right)$$

of the tunnelling probability $T(E)$ is responsible for this feature, but the expression $(V-E)E$, which leads to the dominating terms in (46) for small energies. If the exponential factor would be neglected in (45), the same maximal position $E_{max} \approx kT$ of $g(E)$ would be derived.

Barrier with *bias* voltage As we assume that no scattering of charge carriers occurs in the crystalline core of the Si-nc, a voltage U applied to a barrier structure as shown in Fig. 46 will solely drop at the barriers. Hence the band diagram of a single barrier (Fig. 47) is modified to the diagram shown in Fig. 51. The conduction band edge $E_C^{(2)}$ on the right side of the barrier differs from the band edge $E_C^{(1)}$ on the left side by an amount eU_b. The same holds for the Fermi-levels $E_F^{(1)}$, $E_F^{(2)}$. Therefore the definition $E_C := 0$ of zero point of energy can no longer

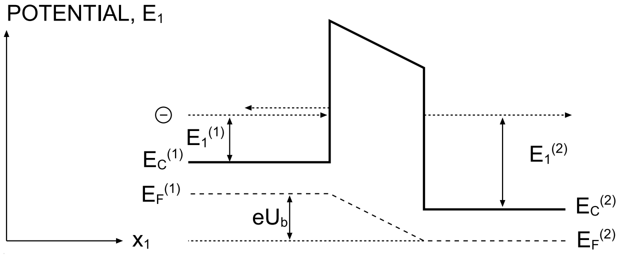

Figure 51: 1-dimensional rectangular barrier with *bias* voltage U_b.

be sustained. The quantities E_C, E_1, E_2, E_3, n, f, T are defined on each side individually. With upper indices the side of the barrier for the individual quantities is denoted,

$$E^{(i)} = E_C^{(i)} + E_1^{(i)} + E_2^{(i)} + E_3^{(i)} \ (i = 1,2).$$

By the *bias* voltage an asymmetry is introduced, which effects a net flow of carriers. In the calculation of the tunnelling current density the following assumptions and approximations are used:

1. The voltage solely drops at the barrier.
2. Occupation of the states is assumed to follow the thermal equilibrium distribution on both sides of the barrier.
3. The inclined barrier (Fig. 51) is approximated by a flat rectangular barrier (Fig. 52).This approximation is justified for $eU_b \ll V$ and $kT \ll V$, which applies in our case. Most of the electrons tunnel through the barrier near its base at energies $E \approx E_C$. (The flat barrier approximation corresponds to the Wentzel, Kramers, Brillouin method (WKB).)
4. Tunnelling probability is approximated by Eq. (40), which is strictly valid only for the symmetric case.

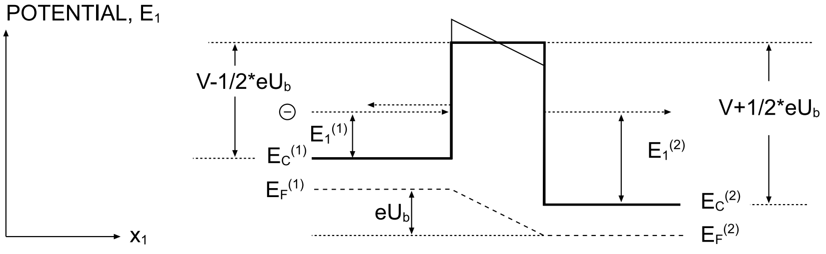

Figure 52: Approximation of tunnelling barrier (Fig. 51) by a flat rectangular barrier.

In this *ansatz* the effective barrier height $V^{(i)}$ $(i = 1,2)$ depends on the direction, from which the electron approaches. It is reduced for electrons on the left side and increased for electrons on the right side:

$$V^{(i)} = \begin{cases} V - 1/2 \cdot eU_b \text{ for } i = 1 \\ V + 1/2 \cdot eU_b \text{ for } i = 2 \end{cases} .$$

Hence also the tunnelling probability $T^{(i)}$ from side i to the other side depends on the side i,

$T^{(i)}(E_1^{(i)})$ = tunneling probability of an electron with kinetic energy $E_1^{(i)}$ in x_1-direction, which tunnels from side i $(i = 1,2)$ through a barrier of height $V^{(i)}$ and width W.

With assumption 4 and Eq. (40) follows

$$T^{(i)}(E_1^{(i)}) \approx 16 \cdot \left(V^{(i)}\right)^{-2} \left(V^{(i)} - E_1^{(i)}\right) E_1^{(i)} \exp\left(-2K_1^{(i)}W\right) \tag{47}$$

with $K_1^{(i)} := \frac{(2m^*(V^{(i)}-E_1^{(i)}))^{1/2}}{\hbar}$.

In conclusion the assumptions imply, that the net current can be regarded as being composed of two contributions, due to the origins:

- The barrier height is different for electrons approaching the barrier from opposite sides.
- Electrons can only tunnel through the barrier, if they can enter empty states on the other side of the barrier (unoccupied states in the conduction band).

Total current density In analogy to Eq. (43) follows:

$$J_\rightarrow \approx \nu \cdot 4\pi e m^* h^{-3} kT \exp(\frac{E_C - E_F}{kT}) \int_0^{+\infty} dE_1^{(1)} \exp(-\frac{E_1^{(1)}}{kT}) T^{(1)}(E_1^{(1)}).$$

In the process of tunnelling from the right to the left one has to take care with the limits of integration. Only electrons with kinetic energy $E_1^{(2)} \geq eU_b$ in x_1-direction can tunnel into empty states in the conduction band on the left side. Therefore the current density reads

$$J_\leftarrow \approx \nu \cdot 4\pi e m^* h^{-3} kT \exp(\frac{E_C - E_F}{kT}) \int_{eU_b}^{+\infty} dE_1^{(2)} \exp(-\frac{E_1^{(2)}}{kT}) T^{(2)}(E_1^{(2)}). \tag{48}$$

By superposition we yield a total current density

$$\begin{aligned} J &= J_\rightarrow - J_\leftarrow \\ &= \nu \cdot 4\pi e m^* h^{-3} kT \cdot \exp\left(-\frac{E_C - E_F}{kT}\right) \\ &\cdot \left(\int_0^{\infty} dE_1^{(1)} \exp\left(-\frac{E_1^{(1)}}{kT}\right) T^{(1)}(E_1^{(1)}) - \int_{eU_b}^{+\infty} dE_1^{(2)} \exp\left(-\frac{E_1^{(2)}}{kT}\right) T^{(2)}(E_1^{(2)}) \right) \end{aligned} \tag{49}$$

As already shown the integrand (44) is maximal at $E_1 = kT$, and similarly

$$g_\rightarrow(E_1^{(1)}) := \exp\left(-\frac{E_1^{(1)}}{kT}\right) T^{(1)}(E_1^{(1)})$$

will be maximal for $E_1^{(1)} = kT$. Therefore we approximate

$$J_{\rightarrow} \approx D \exp(-1) T^{(1)}(kT),$$

with $D := const \cdot kT \exp\left(-\frac{E_C - E_F}{kT}\right)$. We approximate the integral in (48) by the integrand

$$g_{\leftarrow}(E_1^{(1)}) := \exp(-\frac{E_1^{(2)}}{kT}) T^{(2)}(E_1^{(2)})$$

at the same energy $E = E_C^{(1)} + E_1^{(1)} = E_C^{(2)} + E_1^{(2)}$ as for $J_{\rightarrow}$, which amounts to $E_1^{(2)} = eU_b + kT$,

$$J_{\leftarrow} \approx D \cdot g_{\leftarrow}(eU_b + kT) = \exp(-1) \exp(-\frac{eU_b}{kT}) T^{(2)}(eU_b + kT),$$

and meet $J(U_b = 0) = 0$. Applying (40) we yield

$$\begin{aligned} J(U_b) &\approx D \exp(-1) \left[T^{(1)}(kT) - \exp(-\frac{eU_b}{kT}) T^{(2)}(eU_b + kT) \right] \\ &\approx C_1 \exp\left(-\chi W \left[V - \frac{1}{2} eU_b - kT \right]^{1/2} \right) \left(V - \frac{1}{2} eU_b - kT \right) \\ &\cdot \left[kT \left(V - \frac{1}{2} eU_b \right)^{-2} - \exp\left(-\frac{eU_b}{kT} \right) (eU_b + kT) \left(V + \frac{1}{2} eU_b \right)^{-2} \right] \end{aligned} \tag{50}$$

with

$$\chi := 2^{3/2} m^{*1/2} \hbar^{-1} \tag{51}$$

and

$$C_1 := 16 \exp(-1) D.$$

With the effective mass $m_e^* = 0.33 \cdot 9.1 \times 10^{-31}$ kg for electrons we yield

$$\chi_e = 1.48 \times 10^{19}\ \mathrm{J}^{-0.5}\mathrm{m}^{-1} = 5.9\ (\mathrm{eV})^{-1/2}\mathrm{nm}^{-1}$$

and with the effective mass $m_h^* = 0.50 \cdot 9.1 \times 10^{-31}$ kg for holes

$$\chi_h = 1.82 \times 10^{19}\ \mathrm{J}^{-0.5}\mathrm{m}^{-1} = 7.3\ (\mathrm{eV})^{-1/2}\mathrm{nm}^{-1}.$$

6.3.2 Experiments

Charge transport has been measured in interdigital and in sandwich contact configuration. For the measurements with interdigital contacts the same samples as for the *in situ* charge transport have been used (Tab. 11). The sandwich contacts consisted of a ZnO layer on a glass substrate and an upper gold contact with dot diameter 1 mm (measurement on one sample reported (GO_14), parameters Tab. 1). The dependence of dark current at constant voltage vs. time during exposure to ambient air has been measured. Voltage-current characteristics (UI_curves) have been recorded at RT for the samples with interdigital contacts and at temperature $T = 240$ K for the sample with sandwich contacts. (At higher temperature the UI-dependence was unstable and irreproducible for the sample with sandwich contacts.) For the coplanar contacted samples the voltage range was $U_{interd} = (0 \ldots 500)$ V, whereas the sandwich contacted sample was exposed to smaller voltages $U_{sandw} = (-1 \cdots +1)$ V. The corresponding extreme values of electric fields are

$$E_{interd} = 8.3 \times 10^4 \text{ Vcm}^{-1}$$

and

$$E_{sandw} \approx 3 \times 10^4 \text{ Vcm}^{-1}.$$

A severe deficit in reproducibility of UI-curves, recorded in ambient air, was observed. Probably gases or water vapour adsorb on the surfaces of the Si-nc layers and thereby evoke field effects. Concentration differences of gases or humidity can therefore lead to changes in charge transport. One has to imagine how tremendously large the surface to volume ration of layers consisting of agglomerated Si-nc with diameters $d \approx 5$ nm is. To enhance stability, I have recorded UI-curves only with the samples placed in vacuum.

6.3.3 Results

Fig. 53 shows the temporal development of the sample current I_{10V} with an applied voltage $U = 10$ V for sample GO_52 after breaking the vacuum. I_{10V} drops after an exposure time of almost 10^4 min almost an order of magnitude. UI-curves have been measured for sample GO_52 after successive grades of oxidation (Fig. 54 (a)). The first measurement on this sample

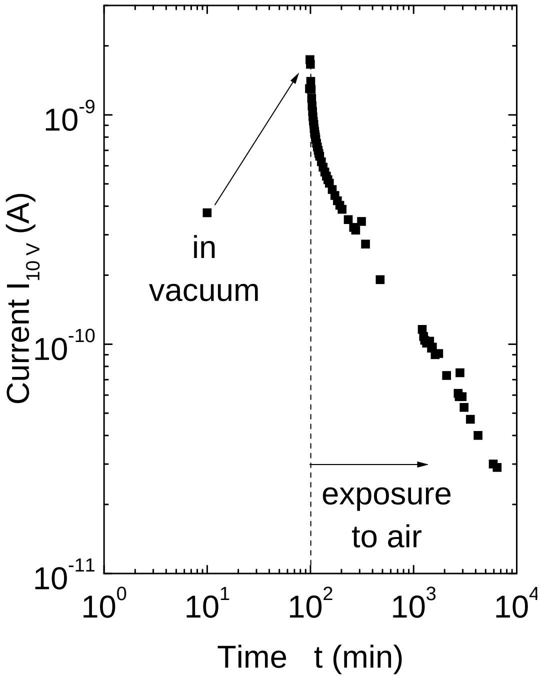

Figure 53: Current $I_{10\,V}$ in dependence on oxidation time t in ambient air (sample GO_52).

was performed in vacuum at pressure $p \approx 5 \times 10^{-5}$ mbar immediately after the deposition. After oxidizing for $10h$ at pre-vacuum pressure $p = 2 \times 10^{-2}$ mbar the second UI-curve has been

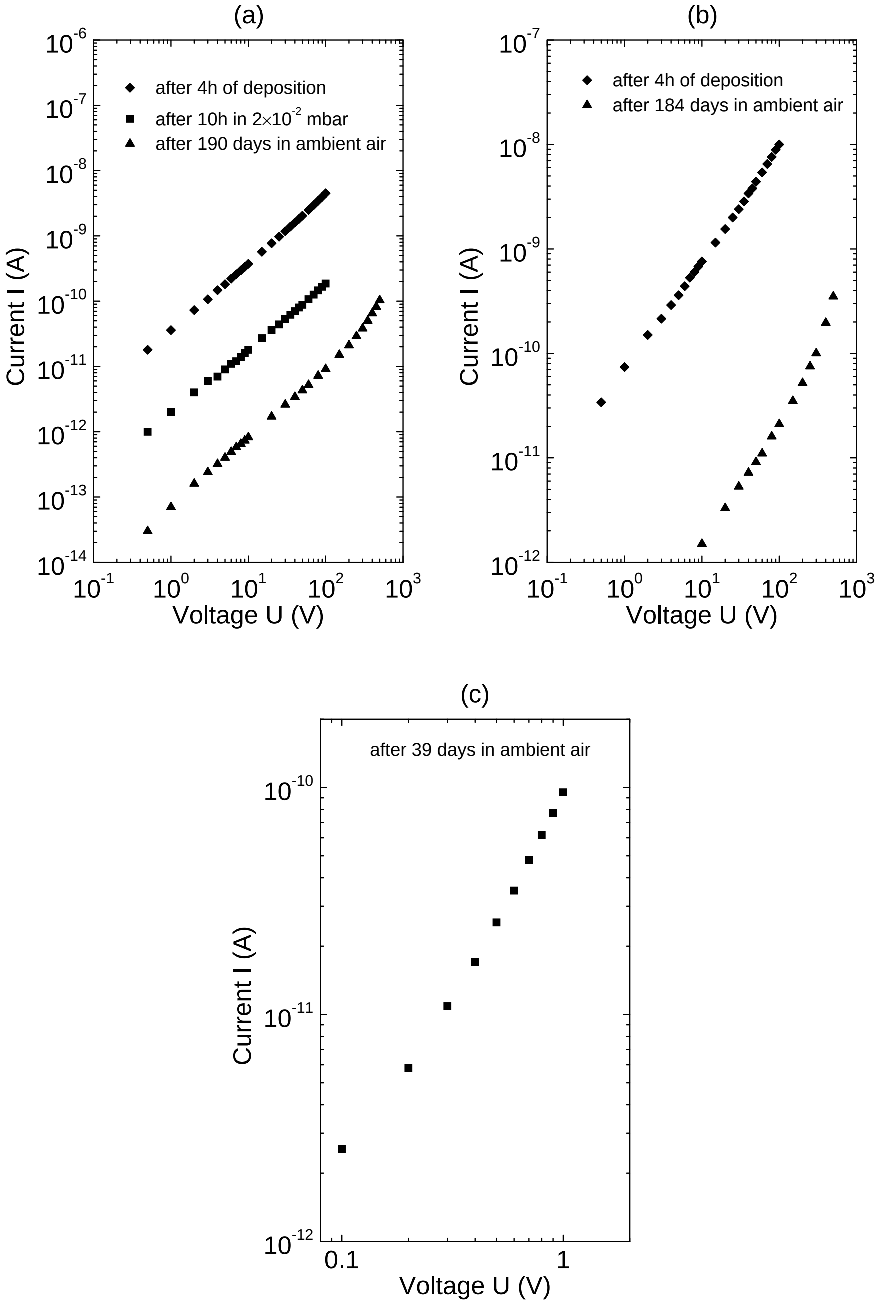

Figure 54: UI-curves for samples with interdigital and sandwich contacts under vacuum. Measurements after successively increasing grades of oxidation. Interdigital contacts, RT: (a) sample GO_52, (b) GO_54. Sandwich contacts, temperature $T = 240$ K: (c) GO_14.

recorded. Finally after oxidation for 190 days in ambient air the third curve was measured. Similar measurements have been performed on sample GO_54 (Fig. 54 (b)). The UI-curve on the sample with sandwich contacts has been recorded after exposing the sample to air for 39 days (Fig. 54 (c)). In the measurements on the samples with interdigital contacts the UI-curves recorded after long oxidation times show a curvature in the log-log plots for voltages $U > 100$ V. Also in the measurement on the sample with sandwich contacts the UI-curve is clearly non-linear (Fig. 54 (c)).

6.3.4 Model

In order to explain measured UI-curves and to reproduce them *via* Eqs. (49), (50), it has been assumed:

1. Charges tunnel in parallel paths through a defined number N of barriers between one contact and the other (Fig. 34, no percolation in the Si-nc layer).
2. The voltage (U_b) at each barrier is the applied voltage (U) divided by the number of barriers: $U_b = U/N$.
3. Tunnelling at the borders of the Si-nc layer (metal / Si-nc, ZnO / Si-nc) is neglected.

6.3.5 Results of numerical model

Fits to the measured data shown in Fig. 54 have been performed using Eq. (50). (Fit procedure with “Non-linear Curve Fit” from software “Origin 5.0” was chosen, which performs a least square fit according to a Levenberg-Marquardt algorithm [27, 30]. In the weighting method “Arbitrary Dataset” was activated and as weighting data the current I, which should be fitted, was specified, which results in weights $w = I^{-2}$. Fit parameters for all samples are listed in Tab. 13.)

First a fit to the measurement data on GO_52 after maximal oxidization was performed. The fixed values $\chi = 7.3$ (eV)$^{-1/2}$nm, $V = 4.5$ eV correspond to exclusive hole transport. Almost perfect agreement was achieved, if the three parameters C_1, W, N were varied, but the calculated *error* of N was of the order of its own value and the *errors* of C_1, W were much larger than their values. This hints to a mutual dependence among C_1, W, N. I have therefore fixed W to different values and observed the behaviour of C_1 and N. When W is increased from 0.01 nm to 5 nm, equally good fits are achieved (Fig. 55 (a)), the number N of barriers is constant, but the factor C_1 varies much (Tab. 13). Therefore the interdependence occurs only between C_1 and W and we obtain a reliable value of parameter N. On the other hand this means, that W cannot be determined from the measurements within our model. Therefore the oxide barrier thickness has been fixed to a reasonable value, $W = 1.0$ nm, and C_1 and N have been determined from the fitting procedure. The same interdependence between C_1 and W and stability of N is found for the fixed parameters $\chi = 5.9$ (eV)$^{-1/2}$nm, $V = 2.9$ eV (values expected for pure electron transport in the conduction bands). For electron transport only the result for $W = 1.0$ nm is given in the table and included in Fig. 55 (a). Also for measurements on the same but less oxidized sample fits have been performed. For these fits the parameters C_1, N were kept constant to the the values obtained for the maximal oxidized stage, and only W was obtained as a fitting parameter, in other words I have assumed that during oxidation the parameters C_1, N stay constant. For the number N of barriers this is evidently true, if the arrangement of the Si-nc does not change. Fit parameter C_1 is supposed to be proportional to the number of channels of Si-nc paths per area, which should also stay constant during oxidation. (Note that this idea was not included in the derivation of (50), because laterally infinitely extended barrier structures were assumed. But a more rigorous calculation would include the fraction of the area of conductive channels perpendicular to the direction of of current.) The smaller the times of exposure to air, the lower are the obtained oxide barrier widths W. The errors received by the fitting procedure of Origin 5.0 are smaller than 0.002 nm, which is much lower than the measurement accuracy for the oxide barrier widths of the sample, obtained by this method. Therefore these errors are left out in the table.

For sample GO_54 the results are similar (Fig. 55 (b)). Note that the determined oxide barriers thickness of the as deposited samples are the same for both samples: 0.60 nm (for hole transport), 0.38 nm (for electron transport).

Analogously (50) can be fitted to the measurements on the sample with sandwich contacts (Fig. 55 (c)). As before the parameters C_1, W show interdependence, when one of them is varied, but the number of barriers stays constant ($N = 521$). Results for $W = 1$ nm and the parameters χ, V fixed to the values either for electron or hole transport are listed in the table.

Sample	C_1 (A)	χ (eV)$^{-1/2}$nm^{-1}	V (eV)	W (nm)	N
GO_52					
190 days ox.	$(2.0 \pm 0.3) \times 10^{-5}$	7.3 (fix)	4.5 (fix)	0.01 (fix)	$(6.7 \pm 0.5) \times 10^5$
”	$(7.1 \pm 0.8) \times 10^{28}$	”	”	5 (fix)	”
”	105 ± 11	7.3 (fix)	4.5 (fix)	1.0 (fix)	”
”	0.12 ± 0.02	5.9 (fix)	2.9 (fix)	1.0 (fix)	$(4.3 \pm 0.5) \times 10^5$
10 h ox.	105 (fix)	7.3 (fix)	4.5 (fix)	0.80	6.7×10^5 (fix)
”	0.12 (fix)	5.9 (fix)	2.9 (fix)	0.69	4.3×10^5(fix)
as deposited	105 (fix)	7.3 (fix)	4.5 (fix)	0.60	6.7×10^5 (fix)
”	0.12 (fix)	5.9 (fix)	2.9 (fix)	0.38	4.3×10^5(fix)
GO_54					
184 days ox.	102 ± 20	7.3 (fix)	4.5 (fix)	1.0 (fix)	$(3.4 \pm 0.6) \times 10^5$
”	0.12 ± 0.03	5.9 (fix)	2.9 (fix)	”	$(2.2 \pm 0.4) \times 10^5$
as deposited	102 (fix)	7.3 (fix)	4.5 (fix)	0.60	3.4×10^5 (fix)
”	0.12 (fix)	5.9 (fix)	2.9 (fix)	0.38	2.2×10^5 (fix)
GO_14					
39 days ox.	20 ± 5	7.3 (fix)	4.5 (fix)	1.0 (fix)	521 ± 90
”	0.022 ± 0.007	5.9 (fix)	2.9 (fix)	1.0 (fix)	323 ± 60

Table 13: Fit parameters for fits to measurements on samples GO_52, GO_54, GO_14 shown in Fig. 55. Temperature $T = 290$ K was considered for samples GO_52, GO_54 and $T = 240$ K for sample GO_14.

The approximation in Eq. (50) is to some extent inappropriate, because the two integrals in (49) have been approximated by the values of the integrands at a single value of energy. In order to check the validity of fits performed with this approximation, I will compare the results of these fits with the results obtained with Eq. (49) instead of Eq. (50), but with the same fit parameters. (Eq. (49) is bare of the above described approximation.) Only the measurements after long time of oxidation have been simulated, because for these the tunnelling model is assumed to be best applicable.

As we are here not interested in the temperature dependence, we write (49) as

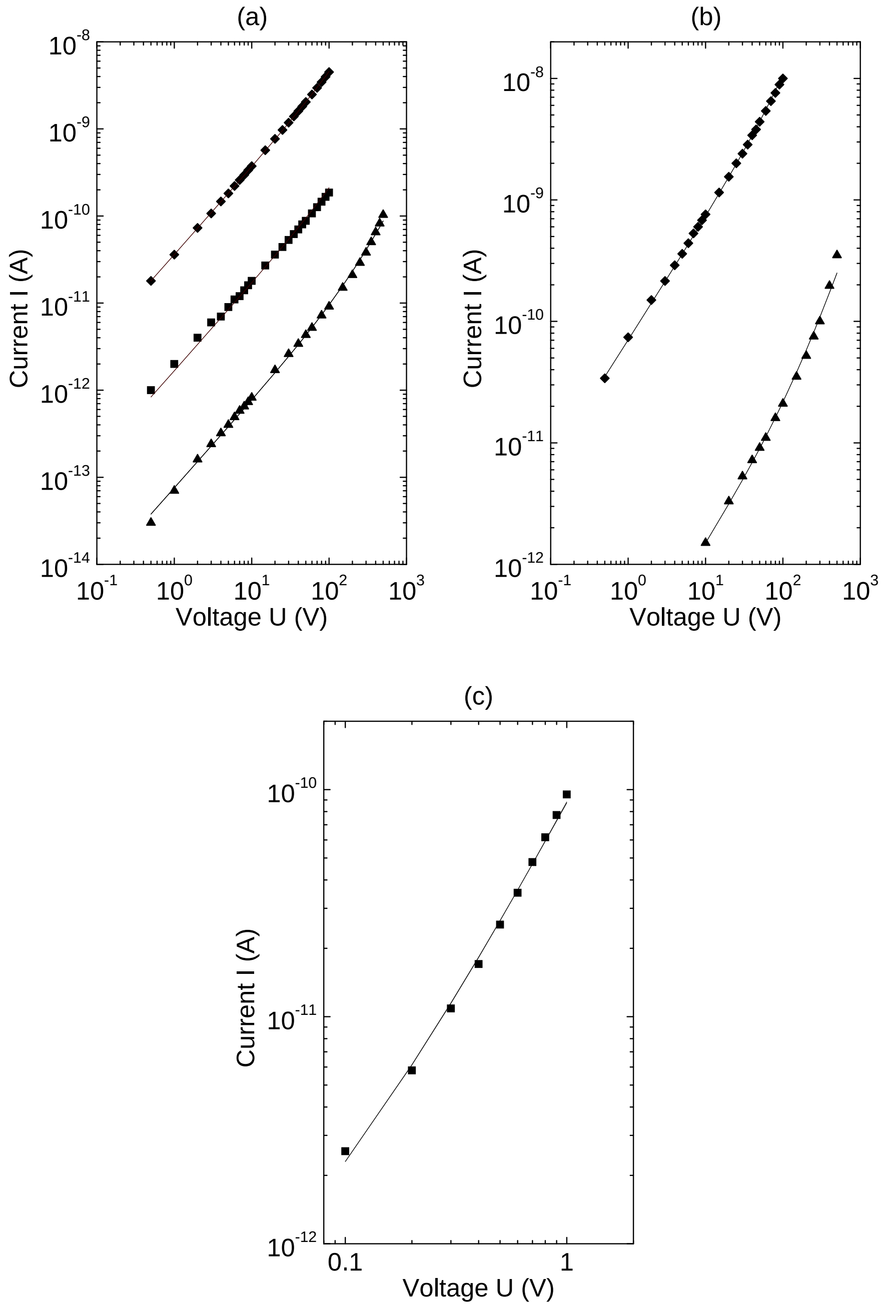

Figure 55: Fits of (50) to the measurements shown in Fig. 54. (a) Sample GO_52, (b) GO_54, (c) GO_14. All fits listed in Tab. 13 are included, where multiple fits are only visible as one solid line.

$$
\begin{aligned}
J &= C_2 \cdot (kT)^{-1} \cdot \left(\int_0^{\infty} dE_1^{(1)} \exp\left(-\frac{E_1^{(1)}}{kT} \right) T^{(1)}(E_1^{(1)}) \right. \\
&\quad \left. - \int_{eU_b}^{+\infty} dE_1^{(2)} \exp\left(-\frac{E_1^{(2)}}{kT} \right) T^{(2)}(E_1^{(2)}) \right), \qquad (52)
\end{aligned}
$$

where the factor $(kT)^{-1}$ has been included to yield constant C_2 in units of Ampere. With the above given abbreviation (51) introducing variable χ, the exponential factor in the approximated tunnelling probability (47) can be simplified as

$$
\exp\left(-\chi \left(V^{(i)} - E_1^{(i)} \right)^2 W \right).
$$

The integrals in (52) have been numerically approximated (function *quad8* of the software MATLAB 6.5) with a relative error of 10^{-6} and upper bounds 0.3 eV and $eU_b + 0.3$ eV respectively have been used (see Fig. 44). In the following the parameters χ, V, W have been taken as estimated by the fits according to (50), but constant C_2 and the number N of barriers have been readjusted. If N is taken as estimated by the fits according to (50), insufficient agreement is achieved between simulation and measurement (Fig. 56, dotted lines). Therfore a fitting procedure was implemented in MATLAB, which varied N. During the fit the measured current data $I_{dat,i}$ $(i = 1,2,3\ldots)$ were normalized such that $\sum I_{dat,i} = 1$. The same normalization was applied to the calculated values $I_{fit,i}$ $(i = 1,2,3\ldots)$ at each step of the fit. By this trick constant C_2 cancels out in the fitting algorithm. It was recalculated afterwards. Hence only parameter N was left free, which was determined by minimizing $\sum_i \left[\left(I_{dat,i} - I_{fit,i} \right) / I_{dat,i} \right]^2$ $(i = 1,2,3\ldots)$ by the MATLAB function “lsqnonlin”. (One also has to supply lower and upper bounds of N to “lsqnonlin” in order to succeed in fitting.) The resulting values are listed in Tab. 14 (2nd, 4th, 6th row) and the fits are included in Fig. 56, solid lines). For the samples with interdigital contacts (GO_52, GO_54) these fits agree well with the measurements. For the sample with sandwich contacts (GO_14) the double logarithmic slope of these fits corresponds better to the one of the measured data than for the above mentioned simulations (dotted lines), but the curvature in the plot does not very well represent the one of the measured data.

Sample	C_2 (A)	χ (eV)$^{-1/2}$nm^{-1}	V (eV)	N	N_{Si-nc}	N/N_{Si-nc}
GO_52	$1.5 / 2.5 \cdot 10^{-3}$	7.3 / 5.9 (fix)	4.5 / 2.9 (fix)	6.7×10^5 / 4.3×10^5 (fix)	1×10^4	67 / 43
”	$0.26 / 6.3 \times 10^{-4}$	”	”	1.20×10^5 / 1.12×10^5	”	12 / 11
GO_54	$1.5 / 2.5 \cdot 10^{-3}$	”	”	3.4×10^5 / 2.2×10^5 (fix)	”	34 / 22
”	$0.17 / 4.2 \times 10^{-4}$	”	”	4.55×10^4 / 4.24×10^4	”	4.6 / 4.3
GO_14	$0.43 / 6.6 \cdot 10^{-3}$	”	”	521 / 323 (fix)	43	12 / 7.5
”	$0.033 / 8.6 \times 10^{-5}$	”	”	66 / 64	”	1.5 / 1.5

Table 14: Parameters used for fits to measurements after long oxidization according to (52). Barrier thickness $W = 1$ nm was assumed for all fits. Listed are also the number N_{Si-nc} of Si-nc, which fit in a straight line between the contacts.

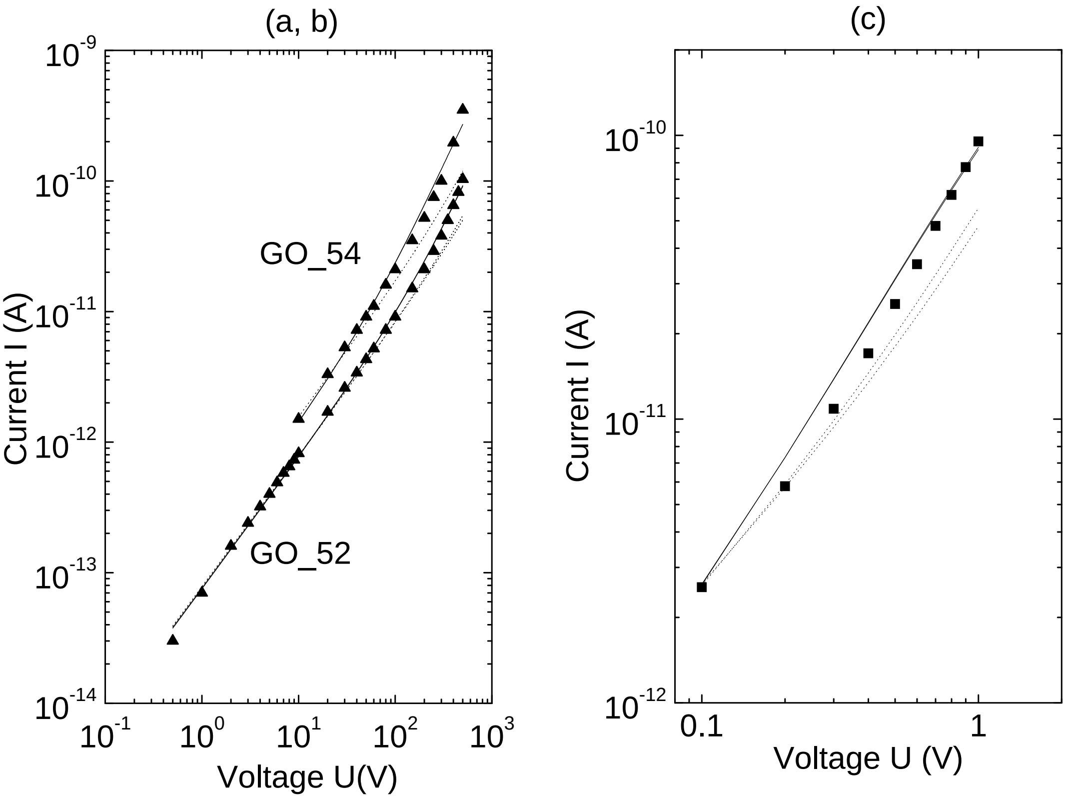

Figure 56: Simulated UI-curve according to (49). Dotted lines: Parameters χ, V, W, N chosen exactly as in Tab. 13, C_2 adjusted. Solid lines: MATLAB fits with N as the only fit parameter (see Tab. 14). (a, b) samples GO_52, GO_54, (c) sample GO_14.

6.3.6 Discussion

Both the fits with the approximate relation (50) and with the exact integral relation (52) nicely reproduce the measured data (with exclusion of fit in Fig. 56 (c)). The interdependence between parameters C_1 (C_2) and W prohibits an absolute determination of either of the two parameters. Thus the question arises, which fit parameters are meaningful. The only other free fit parameter left is the number N of barriers, which turned out to be stable with regards to changes in C_1 or W. Comparing N determined from fits with relations (50) and (52) one detects agreement within a factor of 10. This and the possibility to perform good fits with the approximation, supports the principal validity of approximation (50), but also states that evaluation might reasonably be approved by the more exact formula (52). N can be compared to the number N_{Si-nc} of Si-nc, which fit between the contacts in a straight line. If $d_{contact}$ denotes the distance between the metal contacts and d the Si-nc diameter, it is found

$$N = \frac{d_{contact}}{d}.$$

For the samples with interdigital contacts we have $d_{contact} = 60\ \mu$m and $d = (5.9 \pm 0.1)$ nm (Tab. 1), hence $N_{Si-nc} = (1.02 \pm 0.2) \times 10^4$. For the sample with coplanar contacts $d_{contact}$ corresponds to the Si-nc layer thickness $h_{Si-nc} = (320 \pm 8)$ nm and with $d = 7.4$ we yield $N_{Si-nc} = 43 \pm 2$. In Tab. 14 the ratios N/N_{Si-nc} are listed, they reach from 67 to 1.5. However, a ratio of 67 can hardly be explained by percolation with a path 67 times as long as the electrode gap and is not meaningful. By common sense one would regard ratios $N/N_{Si-nc} \leq 10$ as realistic for layers built from Si-nc. Fits obtained by exact integral relation (52) (2nd, 4th, 6th row in Tab. 14) yield lower values ($N/N_{Si-nc} = 1.5\ldots12$) for the quotient than the ones performed with relation (50) (1st, 3rd, 5th row, $N/N_{Si-nc} = 7.5\ldots67$). These lower values are more realistic, hence the more sophisticated fitting procedure according to Eq. (52) is recommended for evaluation and not the crude approximation (50).

The procedure, which finally led to Eq. (50) was considerably influenced by the model suggested in Ref. [36] for the tunnelling current through crystallites in PSi. In this paper a formula from Ref. [39] “Generalized Formula for the Electric Tunnel Effect between Similar Electrodes Separated by a Thin Insulating Film” was used:

$$J(U) = C_1 \left(V \exp\left(-\chi W V^{1/2}\right) - (V+U)\exp\left(-\chi W \left[V+U\right]^{1/2}\right)\right), \tag{53}$$

where the symbols designate the same quantities as in formula (50). Eq. (53) was derived in Ref. [39] under the assumption of metal electrodes on both sides of an insulator. An electron distribution corresponding to temperature $T = 0$ K was assumed in order to calculate the tunnelling transitions at given *bias* voltage. In my opinion this model can neither be applied to a system of Si-nc separated by oxide barriers nor to a series of oxide-surrounded crystallites in PSi as it was done in Ref. [36]. Si-nc (and similarly the crystallites in PSi) are not metal-like. One cannot suppose a $T = 0$ K electronic distribution in this system in order to determine the possible tunnelling transitions, because in this case the conduction bands of the Si-nc would be entirely empty and the valence bands completely filled by electrons. No charge transfer between the conduction bands (valence bands) of two neighbouring Si-nc would be possible. We have to account for the thermal electrons (holes) in the conduction (valence) bands of the Si-nc in order to correctly describe the tunnelling processes.

If the system of Si-nc was well ordered and well determined, one could surly observe the signature of interference in measurements. Coherent tunnelling through subsequent barriers would occur in such a system. This would demand a treatment according to the formalism developed in [9]. However, the disorder of the position of the Si-nc in the layer and the distribution of the Si-nc diameters seem to destroy any appearance of interference in the undertaken measurements.

6.3.7 Conclusions

UI-curves measured on Si-nc layers with contacts can be fairly well reproduced, both by a numerical model according to approximation (50) and the more exact relation (52). Non-linearity of the curves is successfully modelled by both kind of fits. Whether charge transport is dominated by electrons or holes cannot be distinguished from the fit results, as with both corresponding values for parameter χ and the band offset V equally good fits can be performed. Due to a mutual dependence between the parameter and C_1 (C_2) and the oxide barrier thickness W, both parameters cannot be determined uniquely from a fit. On the other hand the parameter N of the numbers of barriers is stable with regard to changes in $C_1(C_2)$ and W and is extracted as the only reliable fit parameter. The number N of oxide barriers determined from fits according to the more exact relation (52) is closer to the number $N_{Si-nc}$of Si-nc fitting in a straight line between the contacts and the values are more reasonable, which supports this more advanced calculation.

7 Electroluminescence

7.1 Introduction

Development of all-silicon optoelectronics is a challenging task, because it is said that microelectronics industry *will* build every device of silicon, which *can* be built of silicon. Over the years technological know-how about silicon and its easily controllable oxide SiO_2 has tremendously increased and there exist facilities all over the world to fabricate complex structures based on silicon. Nevertheless and in spite of intense research, light emitting electronically driven devices built from silicon are rarely seen in industrial applications.

This is mainly due to an optical disadvantage, inherent in the band structure of Si. Crystalline silicon has an indirect band gap, which means, every optical transition must be accompanied by the creation or annihilation of a phonon. As these three particle processes are unlikely, radiative recombination lifetime is extremely long for c-Si and thus are response times of optical devices built of c-Si. Another disadvantage is due to the low band gap value $E_{g,c\text{-}Si} = 1.12$ eV (at RT) corresponding to a wavelength $\lambda_{g,c\text{-}Si} = 1107$ nm: the radiation emitted by a light emitting diode (LED) built of c-Si is infrared and non-visible by the human eye.

By usage of nano-scaled Si structures the last mentioned disadvantage can be overcome. There are optical transitions in quantum confined states of Si nano-structures, which generate visible radiation. But the disadvantage of the indirect band gap still remains. Average PL decay times for Si-nc with diameters $d \approx 3.4$ nm are reported to be $\tau_{PL} \approx (100 \ldots 500)$ μs at RT [18], which is more than a factor 5000 larger than for CdSe nanocrystals of similar size (see introductory Chapter). This remaining dominant indirect character of the Si-nc band gap can also be deduced from the band diagram sketch shown in Fig. (11). By quantum confinement the distance in k-space between the highest occupied state in the valence band and the lowest unoccupied state in conduction band of Si-nc with diameters $d = 5$ nm is reduced only by a factor $\approx 8/10$ with regard to the value needed for c-Si. Thus for the corresponding transitions phonons with a factor $\approx 8/10$ smaller momenta are needed for radiative transitions, which is not much change with regard to c-Si.

Additionally there are problems to electronically inject carriers into the nano-structures, because they have to tunnel through SiO_2 layers in order to enter. According to [4] transport and photo-luminescence (PL) mutually exclude each other in nano-crystalline Si (also known as micro-crystalline Si). Experimental results in this reference show that PL is quenched, if electric conductivity is increased (by an increase of the Si to SiO_2 ratio). An increase of the silicon network connectivity implies a higher probability of the electrons and holes to tunnel between adjacent crystallites and thus get separated. The decrease in PL was attributed to this mechanism in the above mentioned reference. In this context the high PL yield of the Si-nc samples investigated in this thesis implies that the Si-nc are well separated by oxide barriers and a poor conductivity is expected, which is experimentally confirmed.

A lot of research has already been performed on EL in nano-structured Si. EL has been detected from devices built of porous Si (PSi) [24], Si / SiO_2 layer structures [20], annealed Si-ion implanted SiO_2 layers [25] and nano-crystalline Si [4]. EL has not yet been reported in literature from Si-nc deposited by laser-induced decomposition of SiH_4. In this sense the novel results presented in this chapter affirm the possibility of EL by structures incorporating Si-nc produced by this technique.

7.2 Theory

7.2.1 Band diagrams of p-n, p-i and p-i-n structures

The investigated EL structures consist mainly of three media: a semitransparent metal (Me), the Si-nc layer (Si-nc), which we assume to be intrinsic and a p-type c-Si wafer (p-Si). Therefore two junctions exist, a Me / Si-nc junction and a Si-nc / p-Si junction.

To develop an understanding of the Si-nc / p-Si heterojunction, we first recapitulate the properties of a *p-n* homojunction and then regard the limit of donor concentration $N_D \rightarrow 0$ in the *n*-type semiconductor, while the acceptor concentration N_A in the *p*-type semiconductor is held constant. We also show an exact solution for a *p-i* junction in thermal equilibrium and an approximate band diagram for a *p-i-n* diode. Finally we generalize the results found for a homojunction to a heterojunction. The second junction, Me / Si-nc, is a metal / semiconductor junction, also known as Schottky-contact, which will first be described with help of the simple electron affinity rule and secondly a hypothetical dipole layer between the Me and the Si-nc will be included.

In a *p-n* junction the *built-in voltage* U_{bi} is composed of a voltage drop U_p in the *p* region and a drop U_n in the *n* region. How the voltage is divided between the two regions is governed by the doping concentrations N_D of donors and N_A of acceptors (Appendix A):

$$\frac{U_p}{U_n} = \frac{N_D}{N_A}.$$

i.e., the higher the doping in one region compared to the other, the lower the voltage drop in this region.

A *p-i* junction can be understood as an extreme case of a *p-n* junction with $N_D = 0$. Although in this limit the formalism of a *p-n* junction in depletion approximation is no longer valid, the above described trend is. U_{bi} drops almost entirely on the *i*-side. The *p-i* junction will be described now in more detail. In an intrinsic semiconductor the Poisson-equation reads for a 1-dimensionally varying system

$$U''_{el}(x) = \varepsilon^{-1}\varepsilon_0^{-1}e(p-n), \tag{54}$$

where U_{el} is the electrostatic potential for an electron, p, n are the hole and electron concentrations, ε is the dielectric constant, ε_0 the permittivity of free space and e the elementary charge. By applying the rule that the Fermi-level is constant in thermal equilibrium, one can solve equation (54) in effective density of states approximation. Following [50], Chapter 9, one obtains the solution

$$U_{el}(x) = 4kTe^{-1}\tanh^{-1}\left\{\tanh\left(\frac{eU_{el}(0)}{4kT}\right)\exp\left(\frac{\pm x}{\lambda_i}\right)\right\} \tag{55}$$

with the intrinsic Debye-length $\lambda_i = \left(\frac{kT\varepsilon\varepsilon_0}{2e^2 n_i}\right)^{1/2}$, Boltzmann-constant k, temperature T and the intrinsic carrier concentration n_i. The +sign is valid for the boundary condition $U_{el}(-\infty) = 0$, whereas the $-$sign corresponds to $U_{el}(+\infty) = 0$. Note that for the +sign the solution diverges for $x \rightarrow \infty$ and for the $-$sign for $x \rightarrow -\infty$. As we want to describe a *p-i* junction with the intrinsic layer on the right side, we choose the $-$sign. The voltage drop in the *i*-layer hence is

$$U_i = U(0) - U(\infty) = U(0).$$

Note also that (55) is no general solution of (54); it does not contain the cases of non-vanishing electric field at $x = -\infty$ *and* $x = +\infty$. These cases occur practically, if there are charges at the borders of the layer under investigation. Fig. 57 shows U_{el} in dependence on the dimensionless variable $\xi := \frac{x}{\lambda_i}$ for a total voltage drop $U_i = 0.3$ V in the *i*-region. We extract that the voltage drops from $U_{el}(0) = 0.3$ V to the half value $U_{el} \approx 0.15$ V at a distance $x \approx \frac{1}{10}\lambda_i$. The nominal room temperature intrinsic Debye-length for c-Si is

$$\lambda_{i,c\text{-}Si} = 32\ \mu\text{m} \tag{56}$$

and for Si-nc

$$\lambda_{i,Si\text{-}nc} = 7.2\ \text{mm},$$

where the parameters $\varepsilon_{c\text{-}Si} = 12$, $\varepsilon_{Si\text{-}nc} = 3$, $n_{i,c\text{-}Si} = 8 \cdot 10^9\ \text{cm}^{-3}$, $n_{i,Si\text{-}nc} = 4 \cdot 10^4\ \text{cm}^{-3}$ have been used. Hence after a layer thickness of 1 μm the voltage will drop to $U_{el}(\frac{1}{32}) = 0.20$ V in c-Si and only to $U_{el}(1.4 \cdot 10^{-4}) = 0.2986$ V in Si-nc.

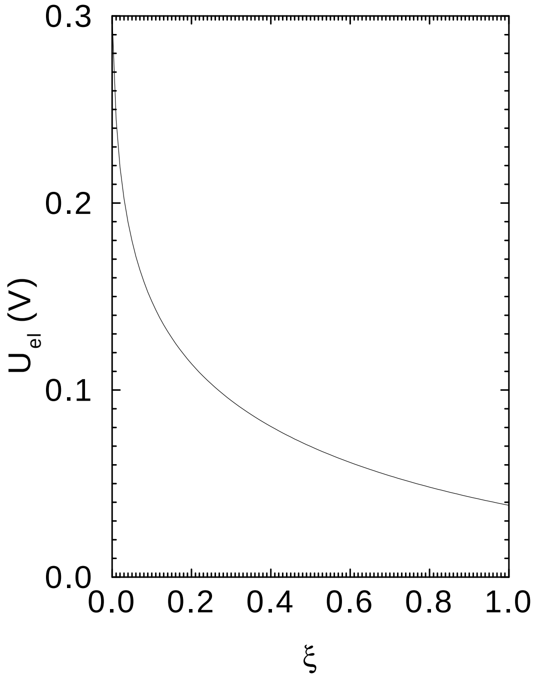

Figure 57: Solution for the potential U_{el} for an electron in an intrinsic semiconductor at room temperature satisfying the boundary conditions $U_{el}(+\infty) = 0$, $U_{el}(0) = 0.3$ V.

From the above exposed trend in p-n junctions, that the voltage mainly drops in the less doped layer, we extrapolate that in a *p*-*i* junction the voltage will almost solely drop in the intrinsic layer. We will assume here, that the voltage drop occurs exclusively in the *i*-layer, that means the built-in voltage equals the voltage drop U_i in the *i*-layer:

$$U_{bi} = U_i.$$

Adding the potential U_{el} from Fig. 57 to the bands in the *i*-layer and presuming that E_C, E_V are continuous at the junction leads to the band diagram in Fig. 58.

The validity of the assumption that the voltage drops only in the *i*-layer will be checked now. How the voltage drop in the SCR is divided between the *p*- and the *i*-layer is governed by the

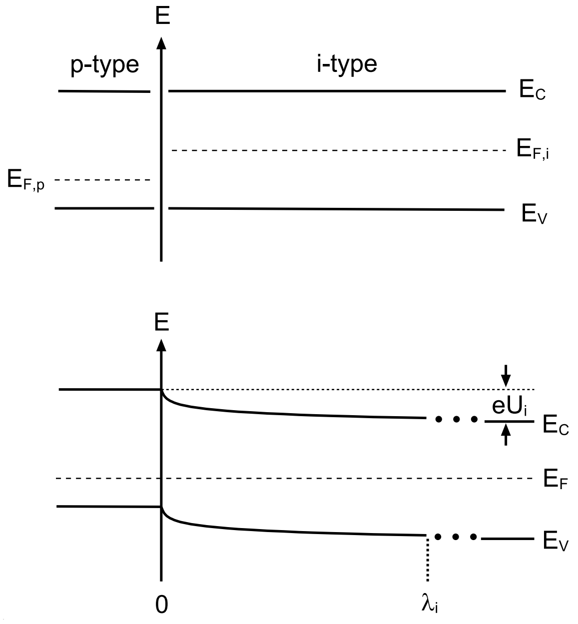

Figure 58: p-i junction. Top: *p* and *i* semiconductors separated from each other. Bottom: p-i junction in thermal equilibrium.

demand of charge neutrality. The sum of the charges Q_p in the *p*-layer and the charges Q_i in the *i*-layer is zero:

$$Q_p + Q_i = 0. \tag{57}$$

The charges in the *i*-layer are obtained by integration and application of the Poisson-equation (54)

$$\frac{Q_i}{A} = e\int_0^\infty (p-n)\,dx = \varepsilon\varepsilon_0 \int_0^\infty U''_{el}(x)dx = -\varepsilon\varepsilon_0 U'_{el}(0) = \frac{2\varepsilon\varepsilon_0 kT}{e\lambda_i}\sinh\left(\frac{eU_i}{2kT}\right). \tag{58}$$

In the *p*-layer the charges per area *A* can be calculated from the acceptor concentration N_A and the extension x_p of the space charges in depletion approximation as

$$\frac{Q_p}{A} = -eN_A x_p. \tag{59}$$

As the voltage in the SCR ($-x_p < x < 0$) of a p-type semiconductor is known in depletion approximation as

$$U(x) = -\frac{eN_A}{2\varepsilon\varepsilon_0}(x+x_p) + C,$$

with a constant *C*, the voltage drop U_p in the *p*-layer can be calculated as

$$U_p = U(-x_p) - U(0) = \frac{eN_A}{2\varepsilon\varepsilon_0}x_p. \tag{60}$$

Combining (57), (58), (59), (60) we yield

$$U_p = -\frac{2\varepsilon\varepsilon_0 k^2 T^2}{e^3 \lambda_i^2 N_A}\left[\sinh\left(\frac{eU_i}{2kT}\right)\right]^2.$$

We use the parameters for a c-Si *p*-*i* junction at room temperature with an acceptor concentration $N_A = 10^{15}$ cm^{-3} in the *p*-layer, i.e. $\varepsilon_{c\text{-}Si} = 12$, $n_i = 8 \cdot 10^9$ cm^{-3}, hence an intrinsic Debye-length (56) $\lambda_i = 32$ μm, $U_{bi} = 0.3$ V and a band gap $E_{g,c\text{-}Si} = 1.1$ eV. By assuming $U_i = U_{bi} = 0.3$ V we finally yield $U_p = 0.033$ V. By combination of (58) and (59) we calculate the extension of the SCR in the *p*-layer as $x_P = 0.21$ μm. The ratio $\frac{U_p}{U_i} = 0.11$ is low enough, that the approximation $U_{bi} = U_i$ is justified for a rough calculation. On the other hand it is high enough to indicate, that an inclusion of the voltage drop in the *p*-layer would significantly improve the above calculations.

In a *p*-*i*-*n* structure the solution of the Poisson-equation (54) in the intrinsic layer in thermal equilibrium is difficult, if its thickness d_i is not large enough to comprehend the SCRs which originate from the *p*-*i* and the *i*-*n* junction. The thicknesses $d_{i,Si\text{-}nc} \approx 1$ μm of the intrinsic Si-nc layers in the EL structure investigated here are much smaller than the corresponding intrinsic Debye-lengths $\lambda_{i,Si\text{-}nc} = 7.2$ mm. Therefore we focus on this case also while describing the *p*-*i*-*n* structures. Solution (55) applies only for boundary conditions $U_{el}(-\infty) = 0$ or $U_{el}(+\infty) = 0$; It cannot be applied in the case of an additional constant electric field, which is supplied by charges outside the *i* layer. For this kind of boundary conditions there does not exist an analytical solution, to my knowledge. The Poisson-equation (54) can be solved numerically by means of a computer, but this lies beyond the scope and intention of this thesis. Instead of this I apply an approximation; I assume that there are only SCRs in the *p* and the *n* layers. In the *n* layer there is a positive SCR and in the *p* layer the space charges are negative. The space charges in the *i* layer are neglected, because of low carrier concentration there, because of low layer thickness $d_i < \lambda_i$ and because of the above mentioned lack of an analytical solution. This implies, that due to the charges in the SCRs of the *p* and the *n* layer, there is a constant electric field in the *i* layer. By depletion approximation in the *p* and *n* layer the voltage drops in the *p*, *i*, *n* layers are calculated as

$$U_p = \tfrac{eN_A}{2\varepsilon\varepsilon_0} x_p^2, \quad U_i = E_{max} d_i, \quad U_n = \tfrac{eN_D}{2\varepsilon\varepsilon_0} x_n^2,$$

where x_p, x_n are the extensions of the SCRs in the *p* and *n* layer and E_{max} is the electric field in the *i* layer. It is convenient to introduce the variable

$$x_{pn} := x_p + x_n;$$

because of charge neutrality, $x_p N_A = x_n N_D$, it is related to x_p, x_n by

$$x_{pn} = \frac{N_A + N_D}{N_D} x_p = \frac{N_A + N_D}{N_A} x_n.$$

By integration of the Poisson-equation in the p or n layer we yield

$$E_{max} = \frac{e}{\varepsilon\varepsilon_0} \cdot \frac{N_A N_D}{N_A + N_D} x_{pn}$$

and hence a built-in voltage

$$U_{bi} := U_p + U_i + U_n = \frac{e}{\varepsilon\varepsilon_0} \cdot \frac{N_A N_D}{N_A + N_D} x_{pn} \left(d_i + \frac{1}{2} x_{pn} \right).$$

Solving for x_{pn} gives

$$x_{pn} = -d_i + \left(d_i^2 + \frac{2e}{\varepsilon\varepsilon_0} \cdot \frac{N_A + N_D}{N_A N_D} U_{bi} \right)^{1/2}.$$

Inserting the values for c-Si with doping concentrations $N_A = N_D = 10^{15}$ cm^{-3}, a band gap $E_{g,c\text{-}Si} = 1.1$ eV and $U_{bi} = 0.6$ V we obtain

$$x_{pn} = 508 \text{ nm}, \quad x_p = x_n = 254 \text{ nm} \ ,$$

$$U_i = 0.478 \text{ V}.$$

The fraction of the built-in voltage, which drops in the *i* layer is

$$\frac{U_i}{U_{bi}} = \frac{0.478}{0.6} = 0.78.$$

This means, approximately 10% of U_{bi} drop in the SCR of the *p* layer and another 10% in the *n* layer (Fig. 59).

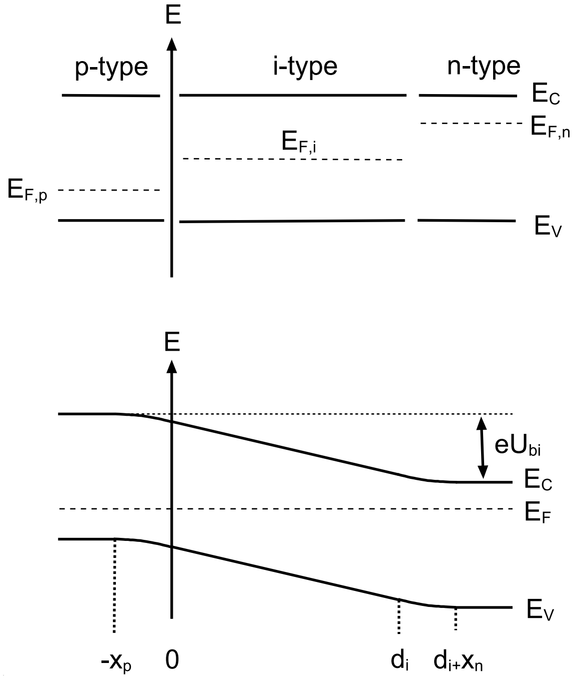

Figure 59: p-i-n structure. Top: *p*,*i* and *n* semiconductors separated from each other. Bottom: p-i-n junction in thermal equilibrium.

For comparison the results of the software “SC-Simul” are shown for the *p*-*i*-*n* structure with the same parameters as above (Fig. 60). The software proclaims a voltage drop $U_i = 0.44$ V in the *i* layer and a built-in voltage $U_{bi} = 0.62$ V, which leads to a fraction

$$\frac{U_i}{U_{bi}} = \frac{0.44}{0.62} = 0.71.$$

This result is approximately 10% lower than the one obtained by the above calculations. Hence the approximation of a constant electric field in the *i* layer - pursued in the above calculations - is supported, although it is not very exact.

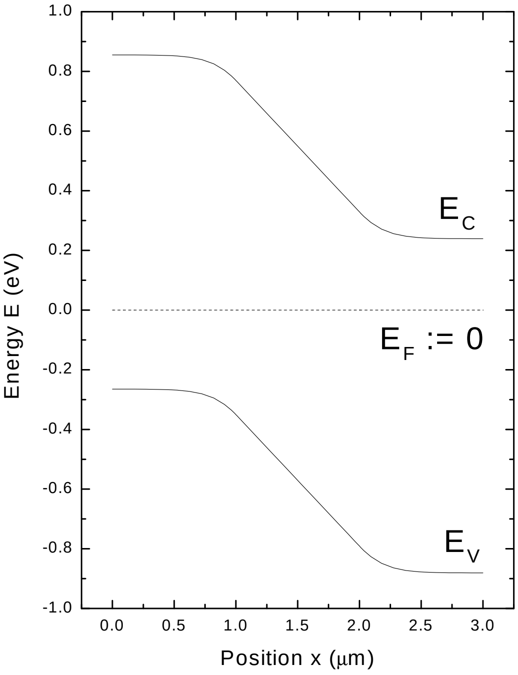

Figure 60: p-i-n junction in thermal equilibrium, result from software “SC-Simul”. Each layer is assumed to be 1 μm thick.

7.2.2 Band diagrams of the investigated EL structures

Electron affinity rule In heterojunctions, like the Si-nc/p-Si junction in the EL structures investigated here, arises the additional complexity to determine, how the valence and conduction bands are connected at the junction in energy scale. For two separated semiconductors, which we assume to be uncharged and have no dipole layers (DLs) or space charges at their boundaries, it is clear from definition of electron affinity, that it determines the absolute energy position of the bands in the semiconductors (Fig. 61 (a)). (The *electron affinity* is defined as the energy, which is released, when an electron transits from the vacuum level into the conduction band.) When the semiconductors are joined together, the energy of the bands in dependence on the position in the semiconductors is only changed by an electric field. The electric field can either be effected by space charges in the semiconductors or by external fields, e.g. generated by a voltage source. The electric field **E** is connected to an electric potential Φ_{el} for **electrons** (*electron potential*) *via*

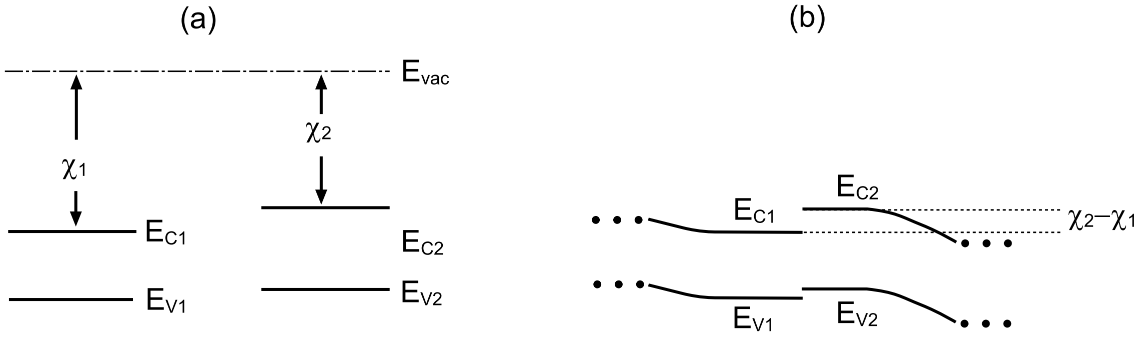

Figure 61: (a) Electron affinities χ_1, χ_2 determine the absolute energy positions of the conduction bands E_{c1}, E_{c2} of two separated semiconductors. (b) Electron affinity rule: The step in the conduction band in a semiconductor heterojunction is determined by the difference $\chi_2 - \chi_1$ of their electron affinities.

$$\Phi_{el}(x) = \Phi_{el}(x_0) + \int_{x_0}^{x} E(x)dx$$

in the 1-dimensional case, which gives the spatially varying energies $E_{C/V}(x)$ of the bands:

$$E_{C/V}(x) = E_{C/V}(x_0) + \Phi_{el}(x).$$

If we assume to be no DLs at the position of the interface, the electron potential is the same in both semiconductors in immediate vicinity of the junction. Thus the energy step in the conduction band at the heterojunction corresponds to the difference in the electron affinities of the two semiconductors (Fig. 61 (b)). This behaviour is called electron affinity rule.

A similar rule exists for metal semiconductor junctions. For a metal the work function W determines the absolute energy position of the Fermi-level (Fig. 62 (a)). (The work function is defined as the energy, which is needed to free an electron from the Fermi-level to the vacuum level.) If no DL is present at a metal semiconductor junction, the barrier for electrons from the metal into the conduction band of the semiconductor is determined by the difference $W - \chi$ of the work function W of the metal and the electron affinity χ of the semiconductor (Fig. 62 (b), Schottky-Mott model). This complies with the electron affinity rule in heterostructures.

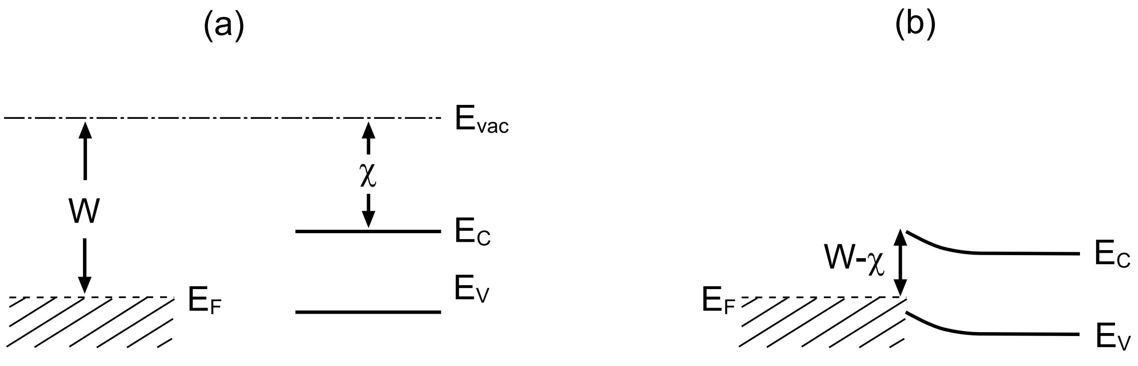

Figure 62: (a) Work function W and electron affinity χ determine the absolute energy positions of the bands of a separated metal and semiconductor. (b) Schottky-Mott model: The barrier between the metal Fermi-level E_F and the conduction band E_C of the semiconductor is determined by the difference $W-\chi$.

According to [38] DLs are built at almost every metal semiconductor interface and play a significant role in the band diagram; DLs are also formed at heterojunctions, but the voltage drop in the DL can often be neglected.

Thermal equilibrium In summary the following approximations and assumptions are made in order to find band diagrams of the EL structures:

1. The porous Si-nc layer, constituted of many attached Si-nc, is treated effectively as a semiconductor with the band gap $E_{g,Si\text{-}nc} = 1.6$ eV of a single Si-nc. (This corresponds to Si-nc with diameter $D_{Si\text{-}nc} = 5$ nm.) The oxide shells around the Si-nc and the pores in between are neglected.

2. a) As first attempt the electron affinity rule and Schottky-Mott model are assumed. Dipole layers (DLs) at the interfaces are neglected.
   b) As second attempt a DL at the Pt / SiO_2 interface is taken into account.

3. The electron potential Φ_{el} is assumed to depend linearly on the position in the Si-nc layer. Because of the Poisson-equation this is equivalent to a constant electric field in the Si-nc layer and also to the absence of space charges there. *All* voltage corresponding to the Fermi-level difference $E_{F,p\text{-}Si} - E_{F,Pt} = 0.65$ eV of the extreme layers Pt and p-Si in the separate state (Fig. 63 , top) is assumed to drop in the Si-nc layer.

In the upper graph in Fig. 63 all energies are given with respect to the vacuum level, which is chosen as zero point. After combining the layers (middle graph), a state is formed in thermal equilibrium, such that the Fermi-level is constant throughout the structure. Therefore the Fermi-level E_F is chosen as reference energy, $E_F := 0$. Space charge regions are present in the equilibrium state, and the electron potential varies in space. This is reflected in the electron potential modified vacuum level $E'_{vac} := E_{vac} + \Phi_{el}$, which is included in the figure.

The electron affinity of c-Si $\chi_{Si} = 4.01\text{ eV} \approx 4.0$ eV according to literature [40]. The electron affinity of the Si-nc follows from the assumption of a band gap $E_{g,Si\text{-}nc} = 1.6$ eV and symmetrical shift of the edges of the valence and the conduction band with respect to c-Si: $\chi_{Si\text{-}nc} = \chi_{c\text{-}Si} - 0.5(E_{g,Si\text{-}nc} - E_{g,c\text{-}Si}) = 3.75$ eV with $E_{g,c\text{-}Si} = 1.1$ eV. The work function of the

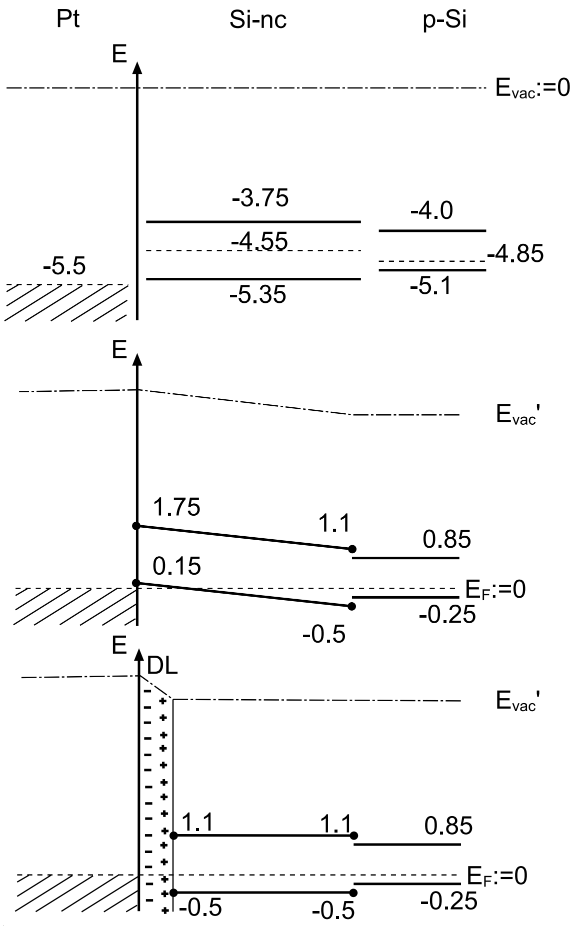

Figure 63: EL structure. Top: State before joining the layers, reference energy is the vacuum energy. Middle: Thermal equilibrium, reference energy is the Fermi-level. Bottom: Additionally a dipole layer (DL) is assumed, which effects a voltage drop $U_{DL} = 0.65$ V. Numbers are energies in eV.

Material	W, χ (eV)	E_g (eV)
Pt	5.5	-
c-Si	4.0	1.1
Si-nc	3.75	1.6
SiO_2	0.85	9

Table 15: Work function W, electron affinity χ and band gap E_g values used in this thesis.

metal platinum is $W_{Pt} = 5.5$ eV according to [37]. Tab. 15 lists values of all work functions, electron affinities and band gaps, which have been used in this thesis.

The distance between the Fermi-level and the valence band $E_{F,p\text{-}Si} - E_{V,p\text{-}Si} = 0.25$ eV of the p-type c-Si wafer follows from its specific resistance $\rho = (10 \pm 2.5)\,\Omega$cm which corresponds to a room temperature hole concentration $p = 1.25 \times 10^{15}$ cm^{-3}. At the borders of the Si-nc layer the energies of the bands have been included in Fig. 63 (middle). These points are marked by circles. The two other numbers denote the energy of the bands of p-Si, which are assumed to be constant.

The degeneracy in the valence band of the Si-nc layer near the Pt / Si-nc interface cannot occur the way it is shown in Fig. 63 (middle). It would effect a huge hole density and thus an enormous amount of space charges, which would alter the electric potential significantly. The assumption of a linear dependence of the electric potential on the position in the Si-nc layer, which is equivalent to the assumption of *no* space charges in the Si-nc layer, would not be tenable in this case. If a DL is assumed at the Pt / Si-nc interface, this degeneracy vanishes (Fig. 63, bottom). The voltage step, generated by the DL, is assumed to be the same as the voltage step U_{DL} in a DL at a Pt / c-Si interface. The Pt / c-Si junction is known to have a barrier height $\Phi_{Pt,c\text{-}Si} = 0.83$ eV ([37], p. 55, for etched c-Si), which is 0.67 eV lower than the value $W_{Pt} - \chi_{c\text{-}Si} = (5.5 - 4.0)$ eV $= 1.5$ eV, predicted by the Schottky-Mott model. I assume that the difference drops in a DL at the Pt / c-Si interface:

$$U_{DL} = 0.67 \text{ V} \approx 0.65 \text{ eV}.$$

The electron potential modified vacuum level E'_{vac} illustrates the voltage drop in the DL (Fig. 63, bottom). No band energies are drawn in the region of the DL, because it is located in an interfacial region.

By taking into account the SiO$_2$ layer on the p-Si substrates and the SiO$_2$ layer between the Si-nc layer and the Pt contact, the band diagram is modified (Fig. 64). For SiO$_2$ a band gap $E_{g,SiO2} = 9$ eV has been assumed and for the off-set between the conduction band $E_{C,SiO2}$ of SiO$_2$ and the conduction band $E_{C,p\text{-}Si}$ a value $E_{C,SiO2} - E_{C,p\text{-}Si} = 3.15$ eV has was chosen [19]. With a band gap $E_{g,p\text{-}Si} = 1.1$ eV we yield an off-set $E_{C,p\text{-}Si} - E_{C,SiO2} = 4.75$ eV of the valence bands. Further we still assume that the bands in the Si-nc layer due to dimensional reduction are symmetrically shifted up / down with respect to c-Si. This leads to band off-sets $E_{C,SiO2} - E_{C,Si\text{-}nc} = 2.9$ eV and $E_{V,Si\text{-}nc} - E_{V,SiO2} = 4.5$ eV between the Si-nc and the SiO$_2$. Note that because of the values $E_{C,SiO2} - E_{C,p\text{-}Si} = 3.15$ eV, $E_{g,SiO2} = 9$ and the electron affinity $\chi_{c\text{-}Si} = 4.0$ eV the electron affinity of SiO$_2$ is determined to $\chi_{SiO2} = \chi_{c\text{-}Si} - \left(E_{C,SiO2} - E_{C,p\text{-}Si}\right) = 0.85$ eV (Tab. 15). A DL is assumed to be established at the Pt / SiO$_2$ interface, which we assume to generate the same voltage step $U_{DL} = 0.65$ eV as mentioned before.

Since SiO$_2$ has been deposited between the Si-nc and the Pt only on two of the three investigated EL samples, the band diagram shown in Fig. 64 can only be considered for these samples.

With bias If a bias-voltage U_{sample} is applied, the band diagram in Fig. 63 (middle) is modified qualitatively to the diagram shown in Fig. 65.

Additionally to the 3 assumptions listed in the previous paragraph we assume that

- 4. a) All bias voltage drops linearly in the *i*-layer.

For bias voltages $U_{sample} = \pm 5$ V one can hardly imagine that the electrons (holes) tunnel from the Pt (p-Si) into the conduction (valence) band of the Si-nc. The distance they would have to

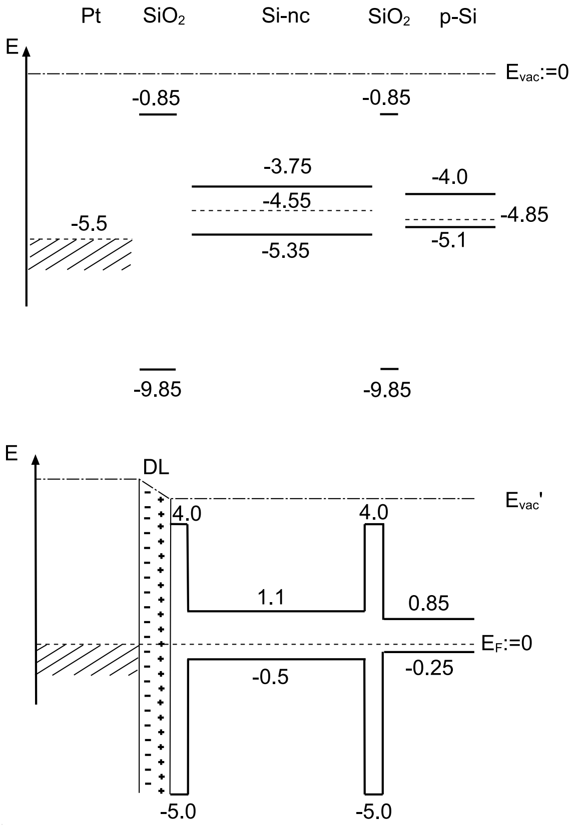

Figure 64: Band diagram of EL structures including SiO_2 layers at the ends of the Si-nc layer and a DL at the Pt / SiO_2 interface. Top: State before joining the layers. Bottom: Thermal equilibrium. Numbers are energies in eV.

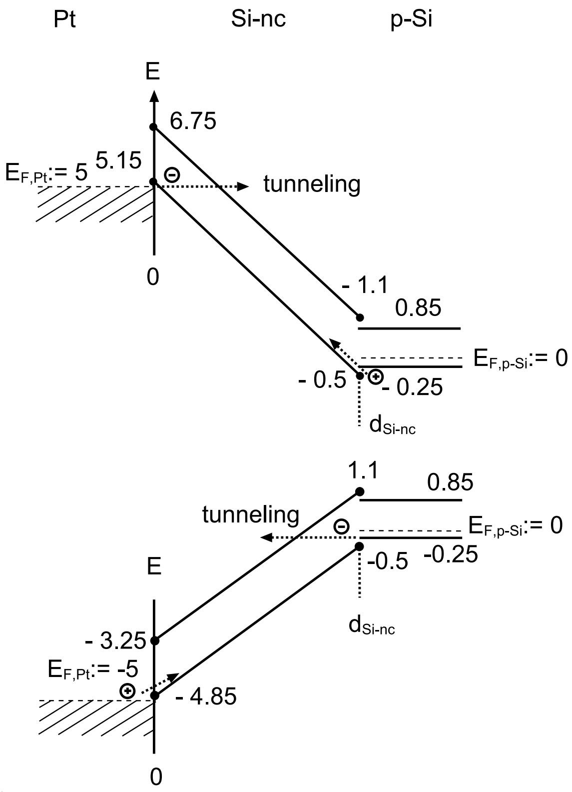

Figure 65: EL structures with positive (upper figure, $U_{sample} = +5$ V) and negative (lower figure, $U_{sample} = -5$ V) bias voltage.

tunnel would be approximately a quarter of the Si-nc layer thickness $d_{Si\text{-}nc}$. It would be 25 nm for a Si-nc layer with $d_{Si\text{-}nc} = 100$ nm. That is too much to yield a sufficient tunnel rate.

If we take into account the SiO_2 layers between the p-Si and the Si-nc and between the Si-nc and the Pt, the injection of the charge carriers into the conduction and valence band of the Si-nc can be explained consistently (Fig. 66 (a), (b)). A large part of the applied voltage U_{sample} is assumed to drop in these SiO_2 layers, such that the the carriers only have to tunnel the short distance through the SiO_2 layers in order to reach the bands in the Si-nc. How the bias voltage is distributed on the different layers of these EL structure, will be answered by a modified assumption:

- 4. b) U_{sample} drops in the SiO_2 layers to such an extend, that the charge carriers are just able to tunnel through the oxide into the corresponding bands. The rest of U_{sample} drops linearly in the Si-nc layer and its magnitude determines the current I_{sample}.

In other words, the applied bias voltage U_{sample} drops at the SiO_2 barriers, just until the emitting and the receiving levels align. For positive bias, the corresponding tunnel levels are ($E_{F,Pt}$ and the conduction band $E_{C,Si\text{-}nc}$ of the Si-nc) and ($E_{F,p\text{-}Si}$ and the valence band $E_{V,Si\text{-}nc}$ of the Si-nc). In case of negative bias they are ($E_{F,Pt}$ and $E_{V,Si\text{-}nc}$) and ($E_{F,p\text{-}Si}$ and $E_{C,Si\text{-}nc}$). The voltage drop in the Si-nc layer is $U_{Si\text{-}nc} = 3.65$ V, $U_{Si\text{-}nc} = -3.15$ V respectively. Thus I_{sample} is expected to be larger for positive bias voltage than for the same negative voltage, which means a diode-like current voltage characteristic (IU-curve) emerges. If no DL was assumed, the situation for positive and negative bias would be inverted. A larger voltage drop $|U_{Si\text{-}nc}| = 3.65$ V would be expected for *negative* than $|U_{Si\text{-}nc}| = 3.0$ V for positive bias. Hence the validity of the model with or without DL can be verified by measurements of IU-curves.

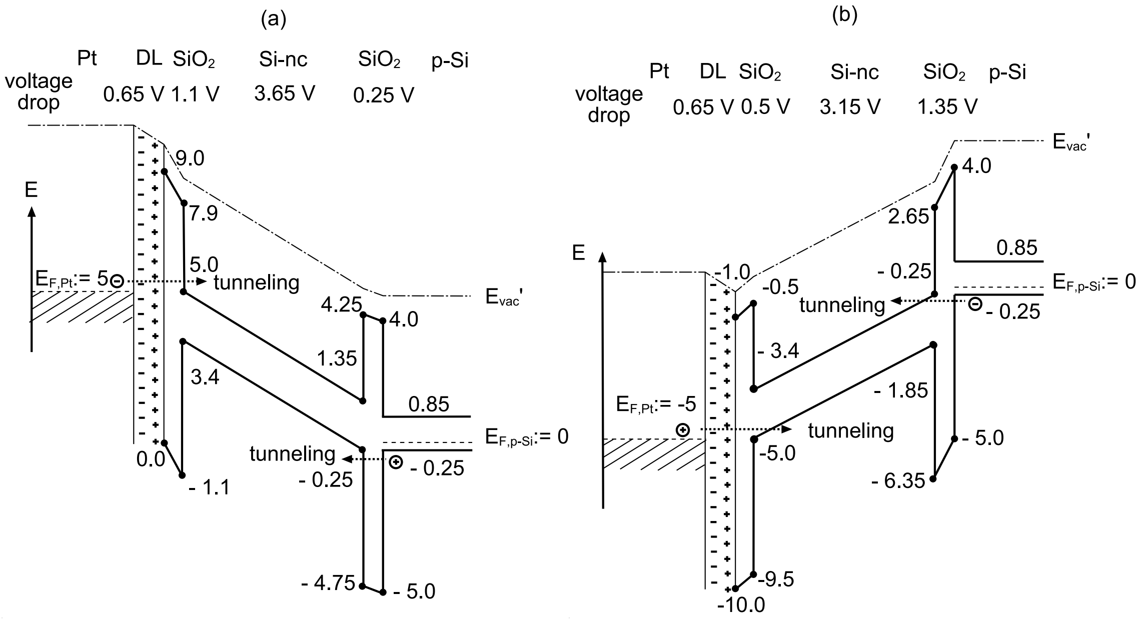

Figure 66: EL structure including SiO_2 layers and a DL at the Pt / SiO_2 interface. (a) Positive bias $U_{sample} = +5$ V, (b) negative bias $U_{sample} = -5$ V.

One general remark about EL is worthwhile to be mentioned: It is impossible to increase the concentration of only one type of carriers in the Si-nc layer bands by injection. Otherwise the total device would be quickly charged and the energy needed to inject more carriers of this type would prohibit a further increase of their concentration. Hence a two band transport model is needed to explain the generation of EL in the Si-nc layer.

7.3 Experimental set-up

The EL yield of the Pt/Si-nc/p-Si samples is so low, that a PL set-up with a monochromator between the sample and the detector was not sensitive enough to record the spectral distribution of the EL. A simple but especially sensitive set-up has been built, where the EL of the sample is focused directly on the sensitive area of a Photomultiplier Tube (PMT) *via* a system of two lenses (Fig. 67), for which the positions were optimized to yield maximal response. The sample can be moved in 3 independent directions in space by means of micrometer screws, so that the optimal position of a new sample can be found by maximizing the EL signal while moving the sample.

Integral EL yields can be measured with this set-up in dependence of the measurement time or while varying the bias voltage on the sample. By introduction of various low-pass transmission filters in a filter holder cut-off yields *versus* cut-off wavelengths have been measured. Subsequent evaluation provides the spectral distribution of the EL.

A computer is used to record the measured values. To reduce the noise of the measured PMT current, each time 100 values of the current are stored in the buffer of the Keithley 617 electrometer, by which the current is measured. Only the mean value is stored by the computer program. The current through the sample is measured by a Keithley 195A digital multimeter (Picoammeter Keithley 480 for small currents) at the same time only once.

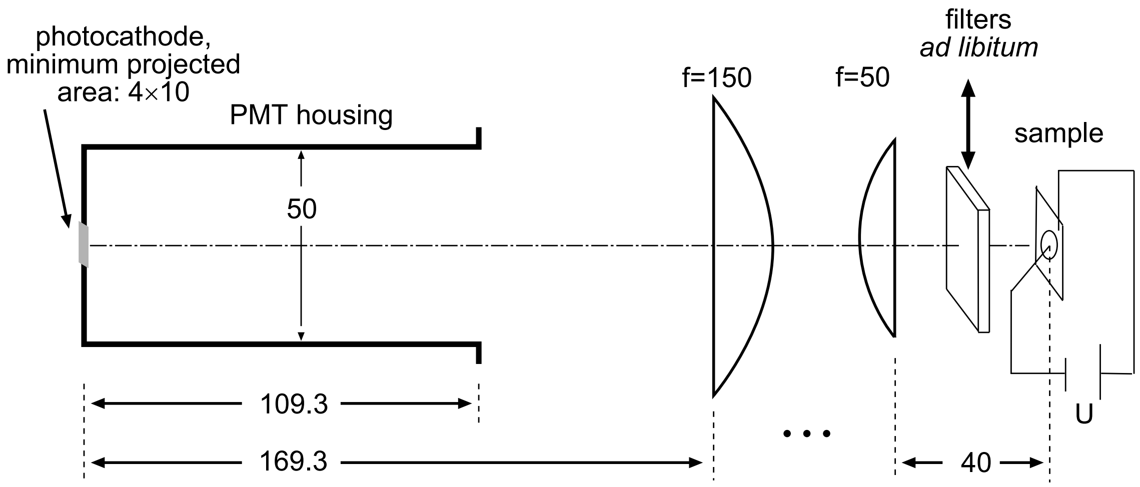

Figure 67: Set-up for EL measurements. All measures are in mm.

7.4 Samples

The EL structures consist of layers of the following materials (see Fig. 68):

p-Si/Si-nc/(SiO_2)/Pt	(GO_36B, GO_11B),
p-Si/Si-nc/Pt	(GO_11A).

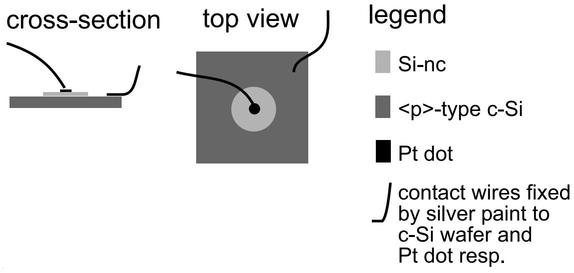

Figure 68: Architecture of EL samples.

SiO_2 has been deposited on top of the Si-nc layers by Plasma Enhanced Chemical Vapour Deposition (PECVD) for samples GO_36B, GO_11B. Depositions took place after sufficient time for the Si-nc layer to oxidize and such passivate the surface. The idea behind depositing SiO_2 was to protect the large surface of the porous Si-nc layer from changes of adsorbates due to ambient air. On the p-Si wafers natural oxide (2 nm according to [21], GO_11A, GO_11B) and thermally grown tunnel oxide (3.5 nm, GO_36B) was present. (See Tab. 16 for parameters of all EL structures).

Samples GO_11A and GO_11B stem from the same sample, which was split into two pieces. The only difference is that on GO_11A *no* SiO_2 was deposited on top of the Si-nc spot in contrast to sample GO_11B SiO_2. The electrical contacts to the p-Si wafers were managed by attaching thin wires with silver paint while scratching with a scalpel at the edge of the wafers in the area covered by silver paint in order to destroy the oxide and contact directly to the p-Si wafer. On top of the Si-nc (and SiO_2) layers Pt dots were evaporated with 10 nm thickness.

Sample	N_A(cm^{-3})	$h_{p\text{-}Si}$ (μm)	$h_{SiO2,p\text{-}Si}$ (nm)	$h_{Si\text{-}nc}$ (nm)	h_{SiO2} (nm)	$\emptyset_{\text{Pt}}$ (mm)
GO_36B	1.25×10^{15}	525 ± 20	3.5	324 ± 12	4	2
GO_11A	1.25×10^{16}	200 ± 20	2	372 ± 15	0	1
GO_11B	“	“	2	“	4	1

Table 16: Parameters of the EL structures. Acceptor concentrations N_A and thickness h_{p-Si} of p-Si wafer, oxide thickness $h_{SiO2,p\text{-}Si}$ on the p-Si wafers, layer thicknesses $h_{Si\text{-}nc}$, h_{SiO2} of the Si-nc and SiO$_2$ layers and Pt dot diameters $\emptyset_{\text{Pt}}$.

These metal contacts are semitransparent with transmittances $T_{Pt}\approx 0.30\pm0.03$ for wavelengths $\lambda = 400\ldots1000$ nm. On top of the Pt dots thin metal wires were fixed by silver paint with the help of a binocular microscope. The resistances of the p-Si wafer can be estimated to 1900 Ω (GO_36B), 500 Ω (GO_11A, GO_11B), if a channel of 10 mm length and 1 mm width and the height of the wafer thickness is taken into account. These resistances are low compared to the measured total resistances of the EL structures at any applied voltages and thus are negligible.

7.5 Procedures of evaluation

7.5.1 Spectral distribution of EL

Low-pass filters with particular cut-off energies have been used to estimate the spectral distribution of the EL emitted from the samples. The cut-off wavelength λ_c is defined as the wavelength, at which the transmittance $T(\lambda_c) = 0.5$ (Tab. 17, Fig 69).

Name	λ_c(nm)	Name	λ_c(nm)	Name	λ_c (nm)	Name	λ_c (nm)
OG495	501	OG590	585	RG695	695	RG800	797
OG515	522	RG610	608	RG715	713	RG830	838
OG530	529	RG630	632	RG9	729	RG850	845
OG550	548	RG645	646	RG780 (1 mm)	758	RG1000	987
OG570	574	RG665	671	RG780 (3 mm)	774		

Table 17: Cut-off wavelengths λ_c of the used low-pass filters.

For the EL signal a Gaussian spectral distribution

$$f(\lambda) = f_0 \exp\left(\frac{-(\lambda-\lambda_0)^2}{2\sigma}\right)$$

is assumed. The function f describes, how many photons arrive at the PMT sensitive area per second and per wavelength interval. We measure cut-off EL yields

$$Y_{c,EL}(\lambda_c) := I_{PMT}(\lambda_c) - I_{PMT,0},$$

where I_{PMT} is the PMT anode current and $I_{PMT,0}$ its dark current. Apart from the distribution f the cut-off yields $Y_{c,EL}(\lambda_c)$ are influenced by two contributions, the PMT quantum efficiency $QE(\lambda)$ (Fig. 70) and the transmittances $T_{\lambda_c}(\lambda)$ of the filters (Fig. 69).

We calculate

$$Y_{c,EL}(\lambda_c) = e\cdot g\cdot s\cdot h(\lambda_c),$$

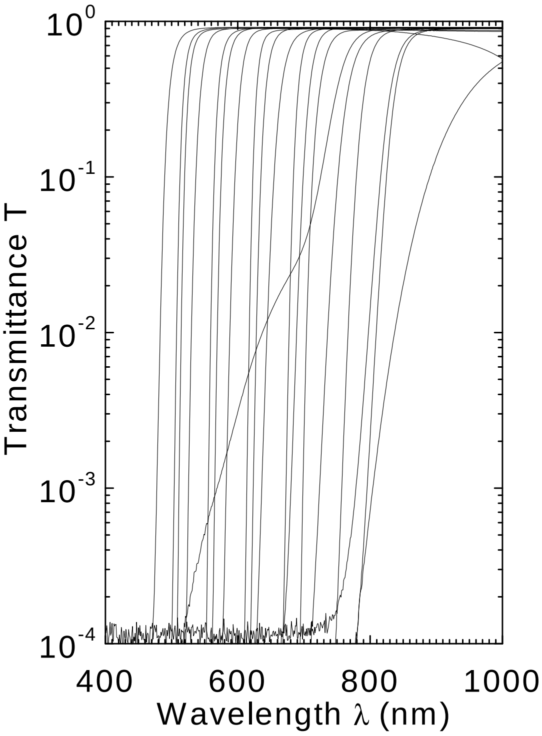

Figure 69: Transmittance of the low-pass filters as measured by a Cary 5E spectrometer.

where e is the elementary charge, g the PMT gain, s the fraction of emitted EL photons reaching the PMT sensitive area and $h(\lambda_c)$ the integral

$$h(\lambda_c) = \int_0^\infty f(\lambda) \cdot QE(\lambda) T_{\lambda_c}(\lambda) d\lambda. \tag{61}$$

We fit the function $h(\lambda_c)$ to the experimental cut-off yields $Y_{c,EL}(\lambda_c)$ by adjusting the parameters f_0, λ_0, σ of the Gauss function f. As a sufficiently good approximation an upper wavelength limit of $\lambda = 1200$ nm has been used instead of ∞.(Fit procedure was performed with a Levenberg-Marquardt algorithm [27, 30] in programming language MATLAB.) From the fit parameters the original spectral distribution function f was reconstructed.

7.5.2 Efficiency of EL

In the ideal case every charge, being injected to a EL structure, will evoke the emission of a photon. Because of non-radiative recombination this limit can hardly be reached. The magnitude, which describes how far injected electron-hole pairs are transformed to emitted photons, is the (internal) EL efficiency η_{EL}. It is defined as the ratio of the number of photons N_P being emitted and the number of injected charges N_Q

$$\eta_{EL} = \frac{N_P}{N_Q}.$$

We measured the emitted photon flux with a PMT, configured to show up a gain $g \approx 10^7$. The Pt dot has an optical transmittance $T_{Pt} = 0.30 \pm 0.03$. If we assume, that the photons are isotropically emitted from the active layer under the Pt dot in the structure, a fraction $s =$

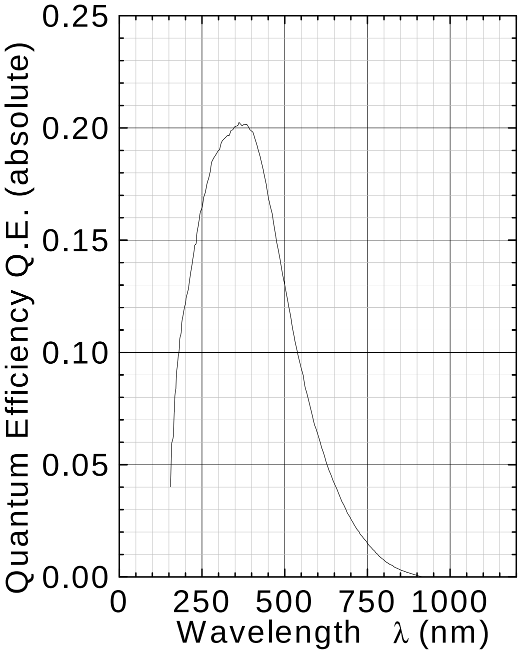

Figure 70: Quantum Efficiency of Photomultiplier Tube (Philips 56TUVP) according to supplier's specifications. (Values for $\lambda > 870$ nm were obtained by extrapolation.)

0.076 of the photons will be collected by the first lens and will therefore reach the PMT. The assumption of isotropical emission in all space directions is justified here, because the Pt dot can be approximated as a point compared to the distance of 40 mm to the lens. Absorption of photons by the two lenses is neglected. With the detected anode current ΔI_{PMT} of the PMT (dark current is subtracted) and the current I_{sample} through the EL structure we yield the internal quantum efficiency

$$\eta_{EL} = \frac{\Delta I_{PMT}}{I_{sample}} \cdot \frac{1}{T_{Pt} \cdot s \cdot g} = 4.4 \times 10^{-6} \cdot \frac{\Delta I_{PMT}}{I_{sample}}. \tag{62}$$

7.6 Results

7.6.1 Current voltage characteristics

All current voltage characteristics show a diode-like behaviour (Fig. 71) with the current density J_{sample} larger for positive bias voltages than for negative ones. (For the EL structures the voltage was defined as positive, if the + pole of the source was attached to the p-Si wafer.) Current density vs. voltage characteristics (JU-curves) were reproducible only to some extent; The JU-curves show up fluctuations versus operation time (see Fig. 71 (c)), which are not referred to here in more detail.

The current densities of the samples GO_11A and GO_36B show up a large difference:

$$J_{sample}^{GO\_11A}(5\text{ V}) \approx 10^{-3} \cdot J_{sample}^{GO\_36B}(5\text{ V}).$$

After splitting the sample GO_11A into two (GO_11A, GO_11B) and the deposition of SiO_2 and the evaporation of a new Pt contact on one (GO_11B) of them, the current density dropped a factor 5 to 50 down to $J_{sample}^{GO\_11B}(5\text{ V}) \approx 2 \cdot 10^{-8} \ldots 2 \cdot 10^{-7}\text{ Acm}^{-2}$(Fig. 71 (c)).

Discussion

The diode character of the JU-curves can be understood by the model presented in subsection 7.2.2. In forward bias a larger part $U_{Si\text{-}nc}$ of the bias voltage U_{sample} drops in the Si-nc layer than for reverse bias. The larger voltage U_{sample} invokes a larger current I_{sample}. By the forward behaviour for positive voltage U_{sample}, the presumption of a DL between the Pt and the SiO_2 layer in the model is affirmed. In conclusion we state, that while the band diagram *without* DL at the Pt / SiO_2 interface cannot explain the diode behaviour of the measured JU-curves, the model with the DL (Fig. 66) qualitatively complies with the experimental results.

The lower current densities for sample GO_11A, GO_11B than for GO_36B can result from their thicker Si-nc layers.

7.6.2 Integral EL yield

The integral EL yield was recorded in terms of the net PMT anode current

$$\Delta I_{PMT} = I_{PMT} - I_{PMT,0},$$

where I_{PMT} denotes the PMT total current and $I_{PMT,0}$ the PMT dark current.

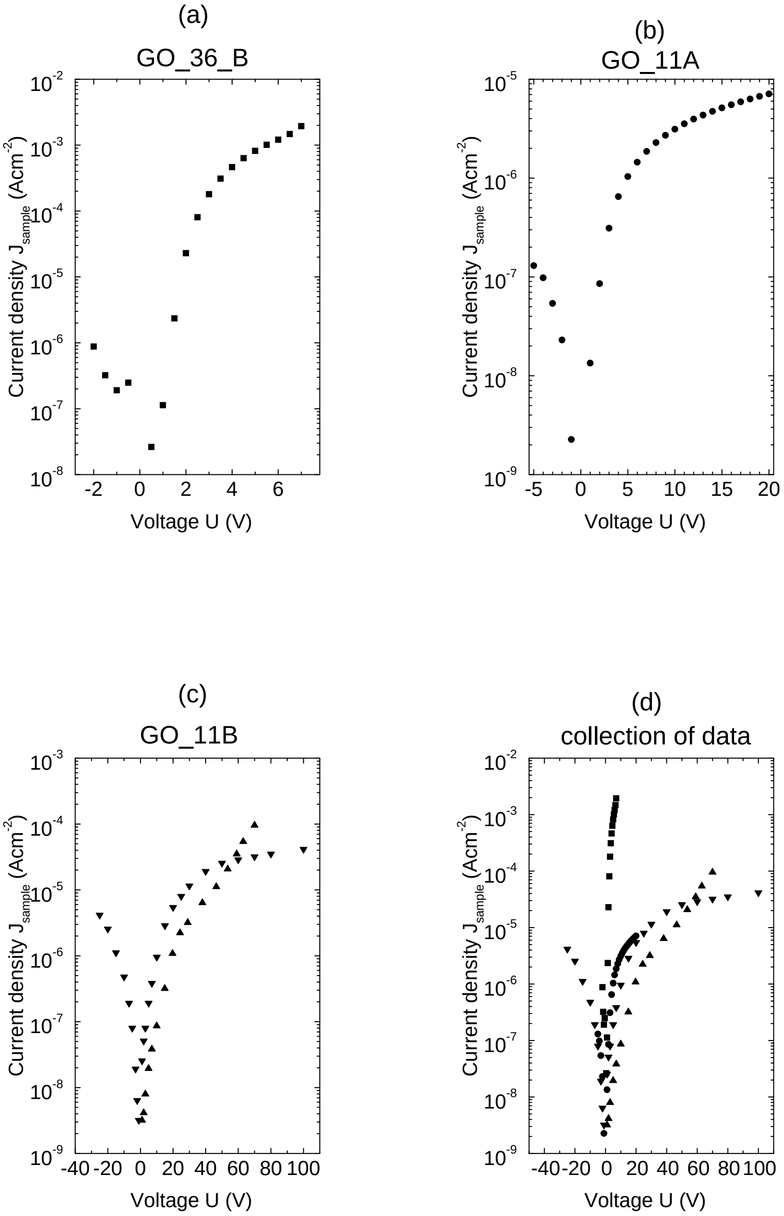

Figure 71: Sample current density J_{sample} vs. voltage U. (a), (b), (c) Diagrams for individual samples. (d) All measurements combined, symbols as in the individual graphs.

Efficiency of EL

Integral EL efficiency η_{EL} has been calculated according to (62) in dependence on the bias voltages U_{sample}. The results shown in Fig. 72 refer to the same measurements as the ones shown in Fig. 71. Sample GO_11A is the same as GO_11B with the difference that *no* SiO_2 has been deposited on top of the Si-nc spot. Astounding is the comparably high efficiency for sample GO_11A at negative voltages. This will be treated in detail in the discussion in subsection 7.6.3.

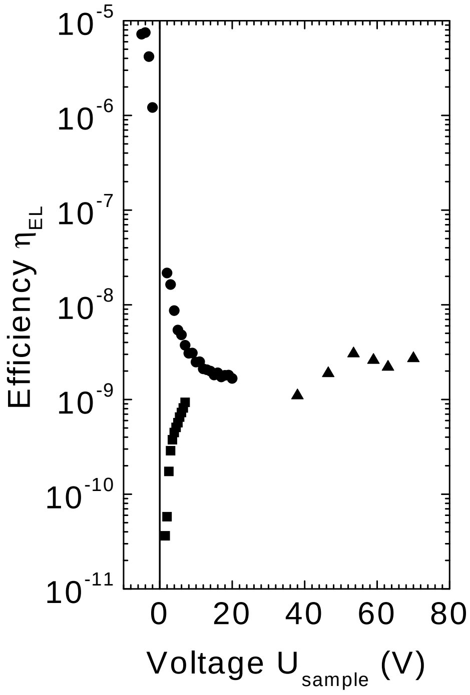

Figure 72: EL efficiency of 3 samples: GO_36B (squares), GO_11A (circles), GO_11B (triangles).

Dependence of EL on sample current

Fig. 73 shows room temperature EL yields vs. sample current for the 3 EL structures. For sample GO_36B the EL yield increases almost linearly for currents $I_{sample} \gtrsim 1.3 \times 10^{-4}$ A, whereas for smaller currents the increase is super-linear. Samples GO_11A, GO_11B show a linear increase in the whole measurement range. Note that the highest measured currents for sample GO_36B ($I_{sample} \approx 2.5 \times 10^{-4}$ A) are much larger than those of samples GO_11A, GO_11B ($I_{sample} \approx 2 \times 10^{-7}$ A, $I_{sample} \approx 3 \times 10^{-6}$ A), Fig. 73 (d). Hence the current region, where the EL signal increases linearly for sample GO_36B is not existent in the measurements on samples GO_11A, GO_11B. Sample GO_36B could also have a second linear increase for currents $I_{sample} < 10^{-5}$ A, but this cannot be distinguished from Figs. 73 (a) and (d). In the measurement of sample GO_11A an additional current $I_{PMT,1} = 3.5 \times 10^{-11}$ A has been subtracted from the signal $\Delta I_{PMT} = I_{PMT} - I_{PMT,0}$ (solid circles) to obtain a twice corrected signal $\Delta I_{PMT,corr} = \Delta I_{PMT} - I_{PMT,1}$ (open circles). (The dark current amounted to $I_{PMT,0} = 7.41 \times 10^{-11}$ A.) In double logarithmic representation (Fig. 73 (d)) the experimental

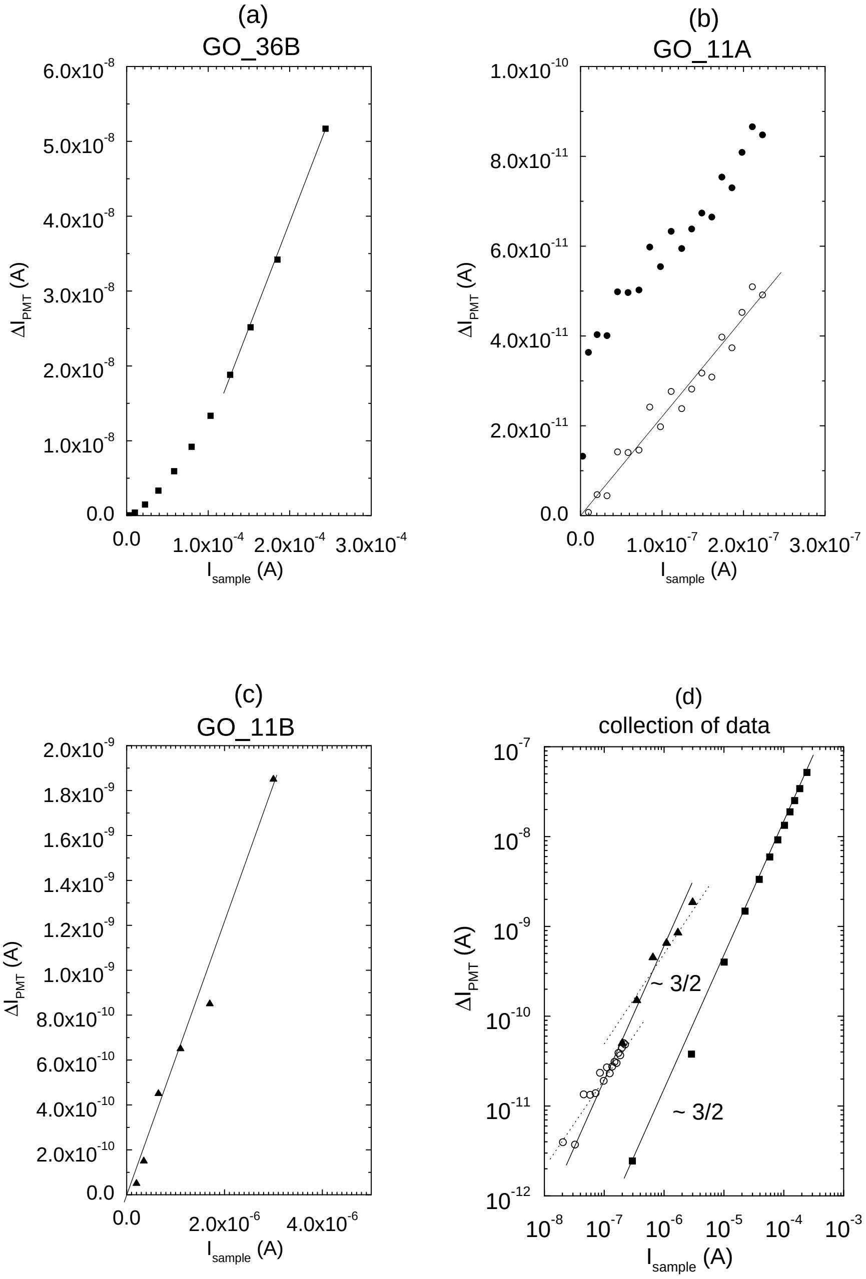

Figure 73: Integral EL yield ΔI_{PMT} vs. sample current I_{sample}. (a), (b), (c) Diagrams for individual samples. (d) All measurements combined in double logarithmic representation (symbols as in the individual graphs). Solid lines represent fits with slope 3/2, dashed lines fits with slope 1.

results of sample GO_36B can be described by a line with slope 3/2. The measurements of samples GO_11A, GO_11B can be fitted separately by lines with slope 1, which corresponds to the linear increases visible in Figs. 73 (b), (c). But also one line of slope 3/2 describes the data of both samples fairly well.

Model

The dependences of ΔI_{PMT} on I_{sample} can be interpreted in the framework of Shockley-Read-Hall recombination. A competition between radiative band-band recombination (R_{CV}) with recombination *via* defects (R_{CD}) takes place. The radiative recombination rate R_{CV} between the conduction band and the valence band of Si-nc has been simulated in dependence of a generation rate G (here injection rate) by a computer program ([22], in MATLAB). Hereby the EL yield ΔI_{PMT} is identified with the radiative recombination rate R_{CV} and the sample current I_{sample} with the generation G. The defects are assumed to be located at mid-gap position and have a density N_D (Fig. 74). Similar to donor levels two possibilities of occupation are assumed for the defects: vacant (positively charged), occupied by 1 electron (neutral). Seven rates are included in the simulation program (see Fig. 74). The arrows indicate the transitions of electrons, which correspond to the respective rate. Besides the external generation G, there are the recombination rates

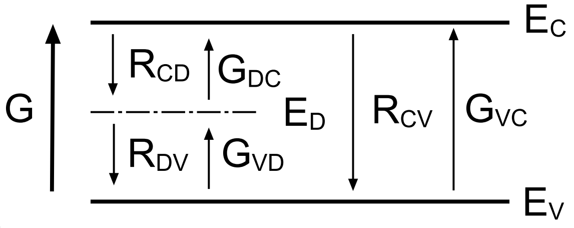

Figure 74: Band diagram of Si-nc with all rates between conduction band (E_C), valence band (E_V) and defects (E_D).

$$\begin{aligned} R_{CV} &= \beta_{CV} \cdot np, \\ R_{CD} &= \beta_{CD} \cdot np_D, \\ R_{DV} &= \beta_{DV} \cdot n_D p, \end{aligned}$$

and the thermal generation rates

$$\begin{aligned} G_{VC} &= \beta_{CV} \exp\left(-\frac{E_g}{kT}\right) \cdot (N_V - p)(N_C - n), \\ G_{DC} &= \beta_{CD} \exp\left(-\frac{E_C - E_D}{kT}\right) \cdot n_D (N_C - n), \\ G_{VD} &= \beta_{DV} \exp\left(-\frac{E_D - E_V}{kT}\right) \cdot (N_V - p)\, p_D. \end{aligned}$$

Here n (p) denotes the electron (hole) concentration in the conduction (valence) band, n_D (p_D) the electron (hole) concentration in the defect level and β_{CV}, β_{CD}, β_{DV} are the recombination coefficients for electrons from conduction band to valence band, conduction band to defect level and from defect level to valence band. A band gap of $E_g = 1.6$ eV, which corresponds to Si-nc with 5 nm diameter, densities of conduction and valence band $N_C = N_V = 3 \cdot 10^{19}$ cm^{-3}, a defect density $N_D = 10^{20}$ cm^{-3} and recombination coefficients $\beta_{CV} = 3 \cdot 10^{-15}$ s^{-1}cm^3 ([14], for c-Si), $\beta_{CD} = \beta_{DV} = 10^{-9}$ s^{-1}cm^3 have been chosen.

The dependence of R_{CV} on G shows 5 regions with different slopes in the log-log plot (Fig. 75 (a), Tab. 18). These slopes can be understood by approximations, obtained by investigation of the following items:

- Which rates prevail for recombination?
- Which are the relations between n, p, n_D and p_D (Fig. 75 (b))?
- Demand of charge neutrality.

In the following we will assume stationarity and zero divergence of the current density, requiring the incoming and outgoing rates to compensate for each of the levels E_V, E_D, E_C.

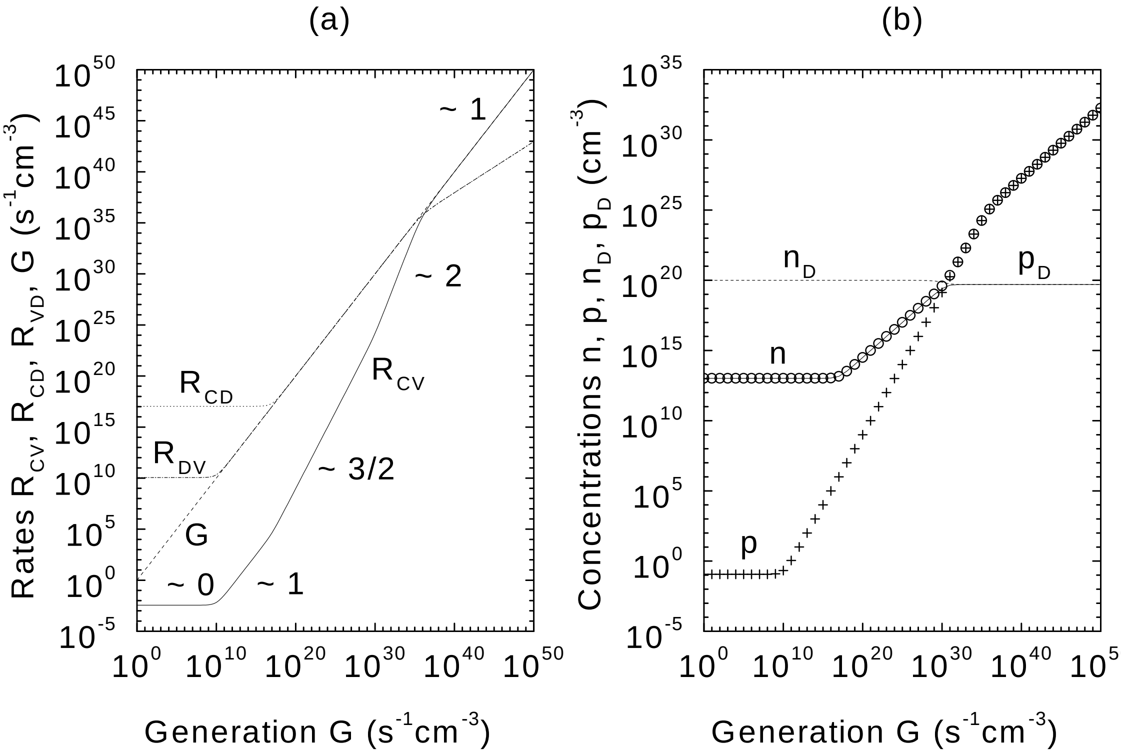

Figure 75: (a) Recombination rates R_{CV} (solid) and R_{CD} (dotted), R_{DV} (dash dotted) in dependence on generation rate G. Generation G is also included (dashed). Slopes of $R_{CV}(G)$ are indicated in this double logarithmic plot by $\sim$. (b) Concentrations n (circles), p (+), n_D (dashed), p_D(solid line).

Slope 0 For small generation rates $G = 10^0 \ldots 10^8$ cm^{-3} the band-band recombination R_{CV} is determined by the thermal generation rate $G_{VC} = \beta_{CV} \cdot (N_V - p)\,(N_C - n)$, which means

$$R_{CD} = G_{VC} = const.$$

slopes in double logarithmic plot	G ($\mathrm{s}^{-1}\mathrm{cm}^{-3}$)
0	$0 \ldots 10^8$
1	$10^{11} \ldots 10^{17}$
3/2	$10^{17} \ldots 10^{30}$
2	$10^{30} \ldots 10^{35}$
1	$> 10^{37}$

Table 18: Regions of constant slope in Fig. 75 (a).

Slope 1 (low generation) The slope of 1 in double logarithmic representation can be understood by investigating, which approximations for the rates (Fig. 75 (a)) and concentrations (Fig. 75 (b)) are valid in this regime. The electron concentration stays constant,

$$n = const., \tag{63}$$

because the generation $G < G_{DC}$. For the holes the situation is entirely different, because the defects are almost fully occupied by electrons:

$$n_D \gg p_D.$$

This effects a much lower thermal generation rate

$$\begin{aligned} G_{VD} &= \beta_{DV} \cdot (N_V - p)\, p_D \exp\left(-\frac{E_D - E_V}{kT}\right) \\ \ll G_{DC} &= \beta_{CD} \cdot n_D\, (N_C - n) \exp\left(-\frac{E_C - E_D}{kT}\right). \end{aligned}$$

(For small generation rates $G = 10^0 \ldots 10^{16}\ \mathrm{cm}^{-3}$, the recombination from E_C to E_D corresponds to the generation from $E_D$to E_C: $R_{CD} \approx G_{DC}$. The same is true at generation rates $G = 10^0 \ldots 10^8\ \mathrm{cm}^{-3}$ for the rates between E_D and E_V: $R_{DV} \approx G_{VD}$. Although generation rates G_{DC}, G_{VD} are not included in Fig. 75 (a), they reveal themselves in the regions, where the recombination rates R_{CD}, R_{DV} do not depend on G.) At generation $G = 10^8\ \mathrm{s}^{-1}\mathrm{cm}^{-3}$ the external generation G and the thermal generation $G_{VD} \approx R_{DV}$ become equal and throughout the region with slope 1 ($G = 10^{11} \ldots 10^{17}\ \mathrm{s}^{-1}\mathrm{cm}^{-3}$) the approximation

$$G \approx R_{DV}$$

is valid. Hence $G \approx \beta_{DV} \cdot n_D p$, which means

$$p \sim G, \tag{64}$$

because $n_D = const.$ (Fig. 75 (b)). The conditions (63) and (64) lead to

$$R_{CV} = \beta_{CV} \cdot np \sim G,$$

which means a slope 1 in double logarithmic representation of R_{CV} vs. G.

Slope 3/2 In the region with slope 3/2 in double logarithmic representation the approximation

$$G \approx R_{CD} \approx R_{DV}$$

is valid. On the other hand

$$n \gg p \tag{65}$$

holds. The the occupation of the defect levels can be calculated by equating the electron capture rate $R_{CD} = \beta_{CD} \cdot np_D$ with the rate $R_{DV} = \beta_{DV} \cdot pn_D$, which is true in stationary state, if the thermal emission rates are negligible:

$$\frac{p_D}{n_D} = \frac{\beta_{VD}}{\beta_{CD}} \cdot \frac{p}{n}. \tag{66}$$

Together with (65) this leads to $n_D \gg p_D$. Therefore we approximate $n_D \approx N_D$ and yield $G \approx R_{DV} \approx \beta_{DV} \cdot N_D p$, such that

$$p \sim G.$$

Charge neutrality means $n = p + p_D$. Because of (65) this implies

$$p_D \approx n.$$

Hence $G \approx R_{CD} = \beta_{CD} \cdot np_D \approx \beta_{CD} n^2$, such that

$$n \sim G^{1/2}.$$

Finally the rate of radiative recombination is

$$R_{CV} = \beta_{CV} \cdot np \sim G^{3/2}.$$

Slope 2 For generations $G = 10^{30} \ldots 10^{35}$ cm^{-3} recombination still takes place mainly *via* defects:

$$G \approx R_{CD} = \beta_{CD} \cdot np_D.$$

Hence, if the hole concentration p_D in the defects is constant, the electron concentration n in the conduction band is proportional to the generation G:

$$n = \frac{1}{\beta_{CD} p_D} \cdot G.$$

In fact (66) implies, that for high generations $G > 10^{30}$s^{-1} cm^{-3}, where

$$p = n \tag{67}$$

holds, the occupation of the defect levels stays constant (Fig. 75 (b)). The constant value of p_D and (67) effect a radiative recombination R_{CV} proportional to the square of the generation rate:

$$R_{CV} = \beta_{CV} \cdot n \cdot p = \frac{\beta_{CV}}{\beta_{CD}^2 p_D^2} \cdot G^2.$$

Slope 1 (high generation) For high generation rates $G > 10^{37} \mathrm{s}^{-1}\ \mathrm{cm}^{-3}$, radiative recombination R_{CV} prevails in comparison to recombination R_{CD} *via* defects. This is due to the quadratic dependence of $R_{CV} = \beta_{CV} \cdot n \cdot p \approx \beta_{CV} \cdot n^2$ on the electron concentration n, whereas the recombination $R_{CD} = \beta_{CD} \cdot n \cdot p_D$ depends on n only linearly. Therefore

$$R_{CV} \approx G$$

holds, which means a slope of 1 in double logarithmic representation.

Discussion

By computer simulation [22] the dependence of ΔI_{PMT} on I_{sample} could be reproduced for the measurements shown in Fig. 73. In order to relate the measured quantities I_{sample}, ΔI_{PMT} and the simulated quantities G, R_{CV}, I have assumed that:

- All injected carriers recombine in the Si-nc layer.
- Recombination takes place in a volume $V_{rec} = \pi\,(\emptyset_{Pt}/2)^2\, d_{rec}$, which is determined by the Pt dot area $\pi\,(\emptyset_{Pt}/2)^2$ and the length d_{rec}, across which recombination in the Si-nc layer occurs (Fig. 76).

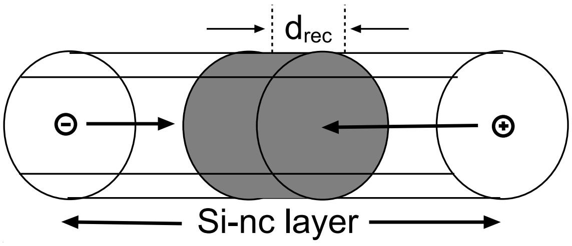

Figure 76: Volume V_{rec} (gray) in Si-nc layer, where recombination takes place.

Hence the sample current and PMT current can be expressed as

$$\begin{aligned} I_{sample} &= GV_{rec}e = 1.3 \cdot 10^{-26}\ \mathrm{Ascm}^3 \left(\frac{\emptyset_{Pt}}{1\ \mathrm{mm}}\right)^2 \cdot G, \qquad (68) \\ \Delta I_{PMT} &= T_{Pt} s g R_{CV} V_{rec} e = 2.9 \cdot 10^{-21}\ \mathrm{Ascm}^3 \left(\frac{\emptyset_{Pt}}{1\ \mathrm{mm}}\right)^2 \cdot R_{CV}, \end{aligned}$$

where e denotes the elementary charge, $T_{Pt} = 0.3 \pm 0.03$ the optical transmittance of the Pt dot, $s = 0.076$ the fraction of the photons emitted from the Si-nc under the Pt dot being collected by the lens system of the set-up (see Subsection 72), $g = 10^7$ the PMT gain and layer thicknesses $d_{rec} = 100$ nm have been assumed. By (68) the measured quantities I_{sample}, ΔI_{PMT} have been translated into the simulated quantities G, R_{CV} for sample GO_36B and they have been included in a computer simulation (Fig. 77 (a)). The measured values are located in the regime, where the simulation shows a slope 3/2 in the double logarithmic plot. For the simulation the following parameters have been used: $E_g = 1.6$ eV, $\beta_{CV} = 3 \cdot 10^{-15}\ \mathrm{s}^{-1}\mathrm{cm}^3$, $\beta_{CD} = \beta_{VD} = 10^{-9}\ \mathrm{s}^{-1}\mathrm{cm}^3$, $N_C = N_V = 3 \cdot 10^{19}\ \mathrm{cm}^{-3}$. Only the concentration N_D of defects was varied, to perform the fit, and $N_D = (6 \pm 2) \times 10^{18}\ \mathrm{cm}^{-3}$ was obtained. Also for samples GO_11A, GO_11B a fit

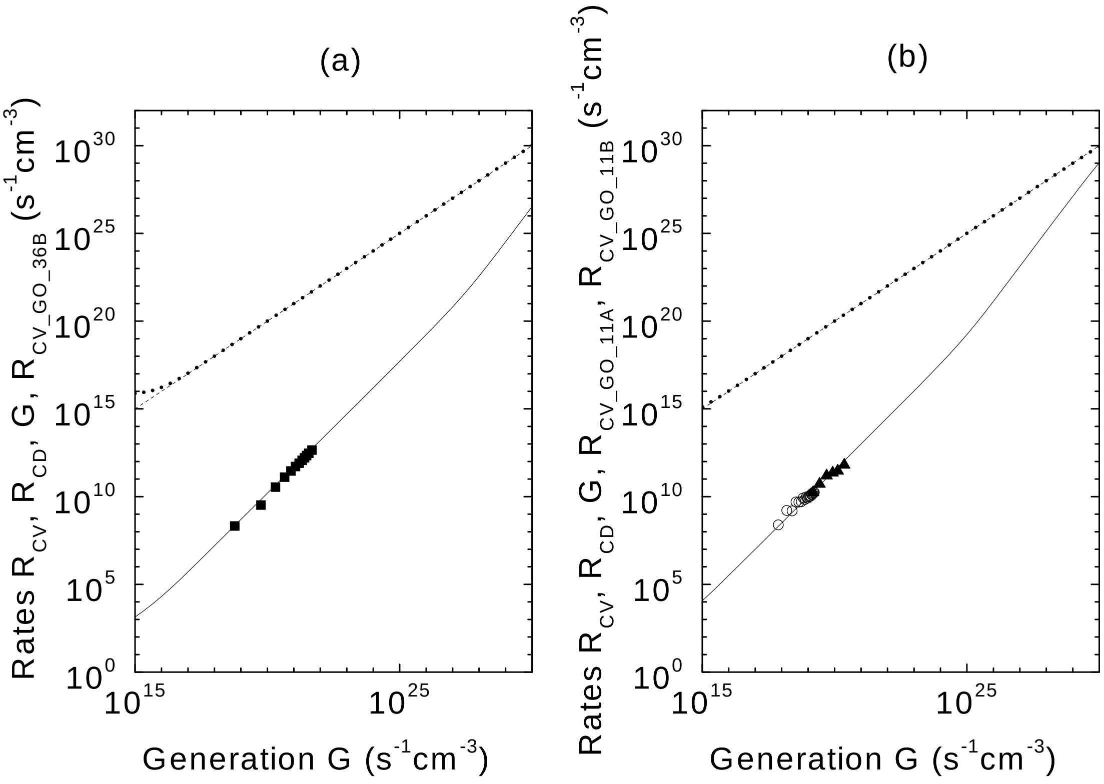

Figure 77: (a) Fit of simulated rate R_{CV} (solid line) to the measured quantity $R_{CV\_GO\_36B}$ (squares), sample GO_36B. (b) Fit of rate R_{CV} (solid line) to $R_{CV\_GO\_11A}$, $R_{CV\_GO\_11B}$ (open circles, triangles), samples GO_11AB, GO_11B. Simulated rates R_{CD} (dots) and generation G (dashed) are also included.

could be achieved (Fig. 77(b)). Here the region is also one of slope $3/2$. A defect concentration $N_D = (3 \pm 2) \times 10^{17}$ cm^{-3} was determined. The rest of the parameters has been chosen identical as above. In order to provide better comparison of the fits and the measured data, the simulated quantities G, R_{CV} have been translated according to (68) into currents $I_{sample,sim}$ and EL yields $\Delta I_{PMT,sim}$ and have been included in Fig. 78.

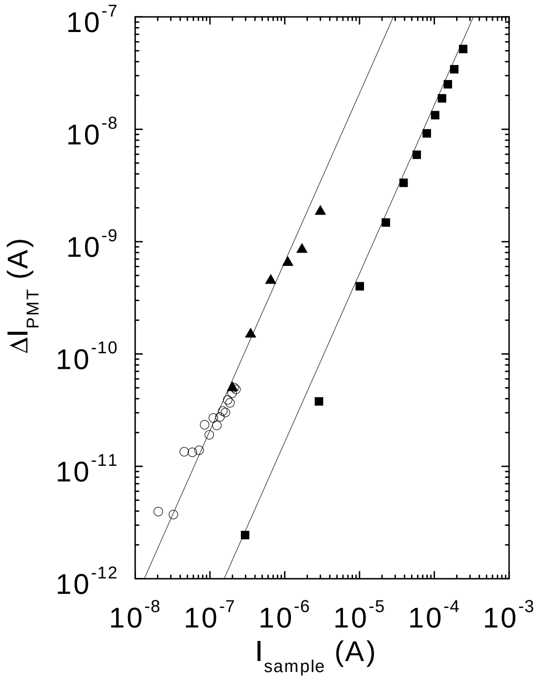

Figure 78: Computer simulation has been used to reproduce the measurements shown in Fig. 73 (d). Solid lines represent the recombination rate R_{CV} translated into an EL yield ΔI_{PMT} *via* (68).

The question about the nature of the defect states remains open. They could be situated at the interfaces between two adjacent Si-nc.

Time-dependent fluctuation of EL

While the EL signal ΔI_{PMT} vs. time stays almost constant for measurements on GO_36B, GO_11A ($U_{sample} = -5$ V), GO_11B ($U_{sample} = 100$ V), it considerably varies for GO_11A ($U_{sample} = 15$ V), GO_11B ($U_{sample} = 15$ V) up to the end of the measurements at $t \approx 8000$ s (Fig. 79 (a)). In contrast the EL efficiency η_{EL}, determined by (62), stays almost constant for all samples for times $t > 2000$ s (Fig. 79 (b)). (The EL efficiency η_{EL} is proportional to the quotient $\Delta I_{PMT}/I_{sample}$.) Thus the decrease in ΔI_{PMT} and the decrease of I_{sample} in the above mentioned measurements partially compensate in the efficiency η_{EL}.

7.6.3 Spectrally resolved EL

Before every spectral EL measurement, time-dependent integral EL measurements have been performed, in order to check, if the integral EL was constant versus time. For sample GO_11B, however, the sample current I_{sample} was changing during the spectral EL measurements (Fig.

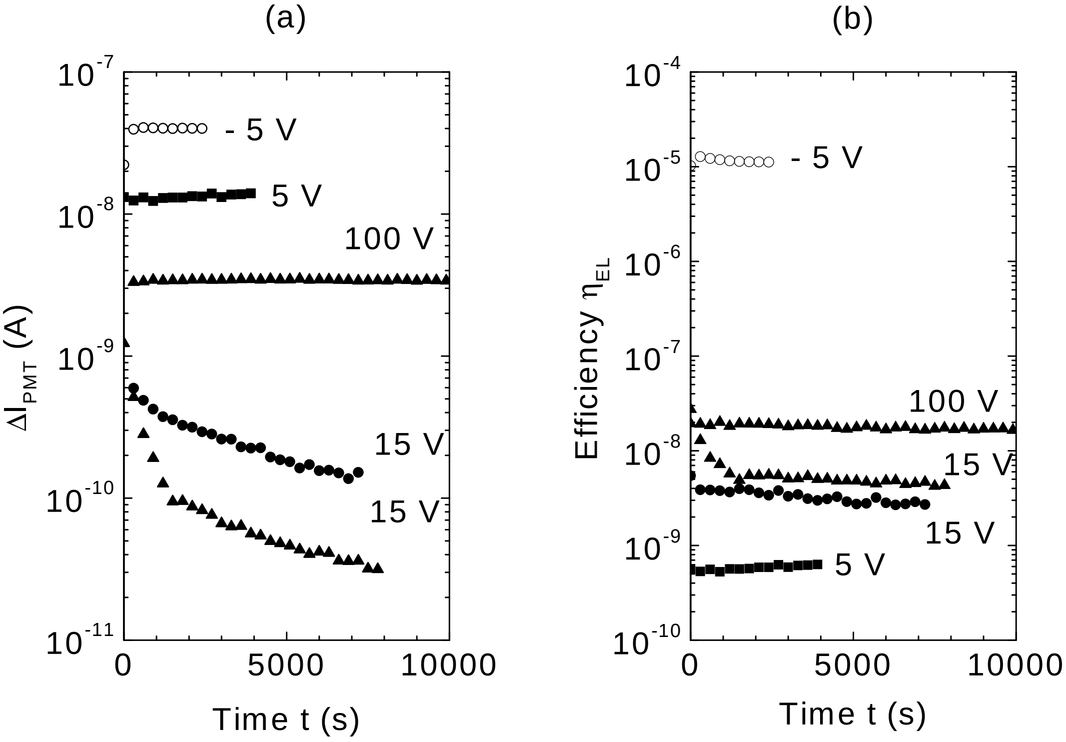

Figure 79: EL signal ΔI_{PMT} and efficiency η vs. operation time. Samples GO_36B (squares), GO_11A (circles), GO_11B (triangles).

80). As reported earlier, the EL efficiency η_{EL}, determined by (62), stayed almost constant for

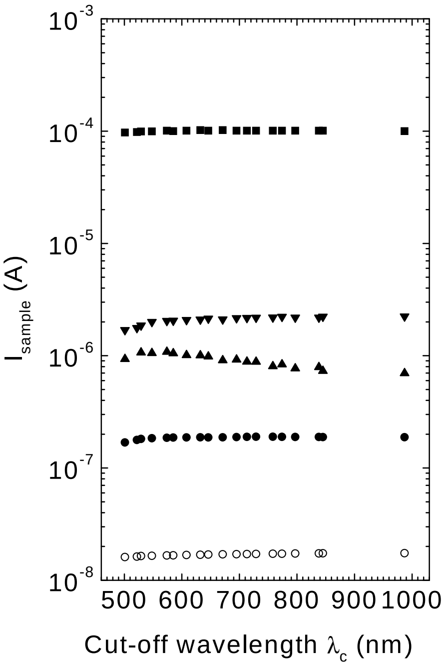

Figure 80: Sample currents I_{sample} during spectral EL measurements. One data point consumed 1.5 min, such that all 19 measurement points took 28.5 min. Squares GO_36B, solid circles GO_11A $+15$ V, open circles GO_11A -5 V, triangles GO_11B.

all samples for times $t > 2000$ s (Fig. 79), even when I_{sample} still varied. Therefore the quotient $Y_{c,EL}(\lambda_c)/I_{sample}$, which for $\lambda_c = 0$ nm is proportional to η_{EL}, is better suited to determine the spectrally resolved EL distribution than $Y_{c,EL}(\lambda_c)$ in this case. Hence for sample GO_11B the function $h(\lambda_c)$ was not fitted to the EL yield $Y_{c,EL}(\lambda_c)$, but to the quotient $Y_{c,EL}(\lambda_c)/I_{sample}$.

In order to determine the spectral distribution of EL, the function $h(\lambda_c)$, Eq. (61), was fitted to the measured cut-off yields $Y_{c,EL}(\lambda_c)$ (quotient $Y_{c,EL}(\lambda_c)/I_{sample}$ for GO_11B) of the samples for different bias-voltages U_{sample} (Fig. 81). Spectral EL has been measured for sample GO_11A twice, once with positive $U = +15$ V and once with negative bias voltage $U = -5$ V. For none of the other samples EL was detected with negative bias voltage. The EL yields f are reconstructed from the fits in Fig. 81 and compared to the PL yields Y_{PL} (Fig. 82). On sample GO_11B two spectral measurements have been performed, of which only one is shown in Fig. 81 (d), but the reconstructed EL yields f are shown for both measurements (Fig. 82 (d)). The peak wavelengths $\lambda_{max,EL}$ for the EL and $\lambda_{max,PL}$ for the PL coincide fairly well within an accuracy ± 60 nm for samples GO_36B, GO_11A. Only the measurements on sample GO_11B show up a large difference $\Delta\lambda_{max} \approx 185$ nm. The differences $\Delta\lambda_{max} := \lambda_{max,EL} - \lambda_{max,PL}$ are listed in Tab. 19.

On sample GO_11B SiO_2 has been deposited on top of the Si-nc spot by PECVD. SiO_2 has also been deposited on top of the Si-nc spot of sample GO_36B, but one has to keep in mind that the current density through sample GO_11B was much lower than for sample GO_36B (Fig . 71).

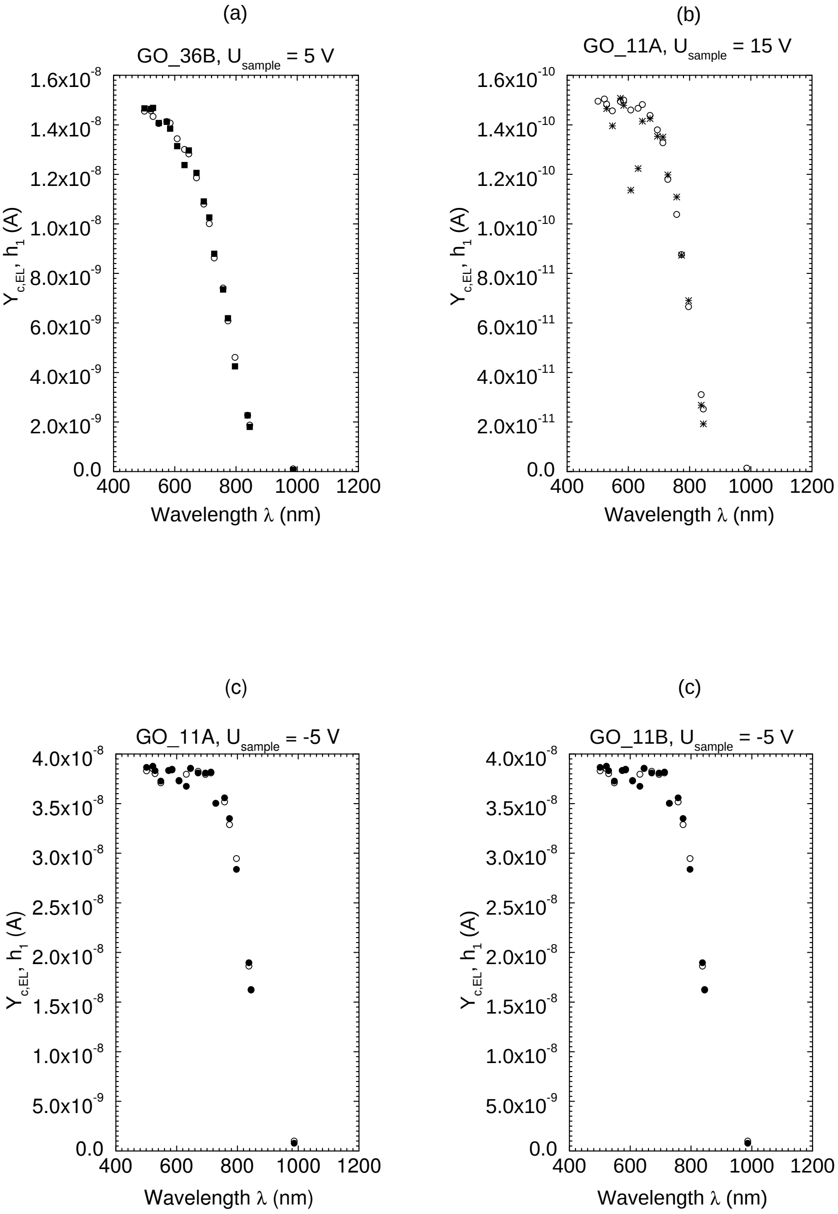

Figure 81: Measured cut-off yields $Y_{c,PL}$ (bias-voltages U_{sample} noted on top of the graphs). Fitted functions h_1 are indicated by open circles.

Sample	$\Delta\lambda_{max}$ (nm)
GO_36B	-23.3
GO_11A ($U_{sample} = +15$ V)	-19.8
“ ($U_{sample} = -5$ V)	60.2
GO_11B	-184.6

Table 19: Differences between EL and PL peak positions.

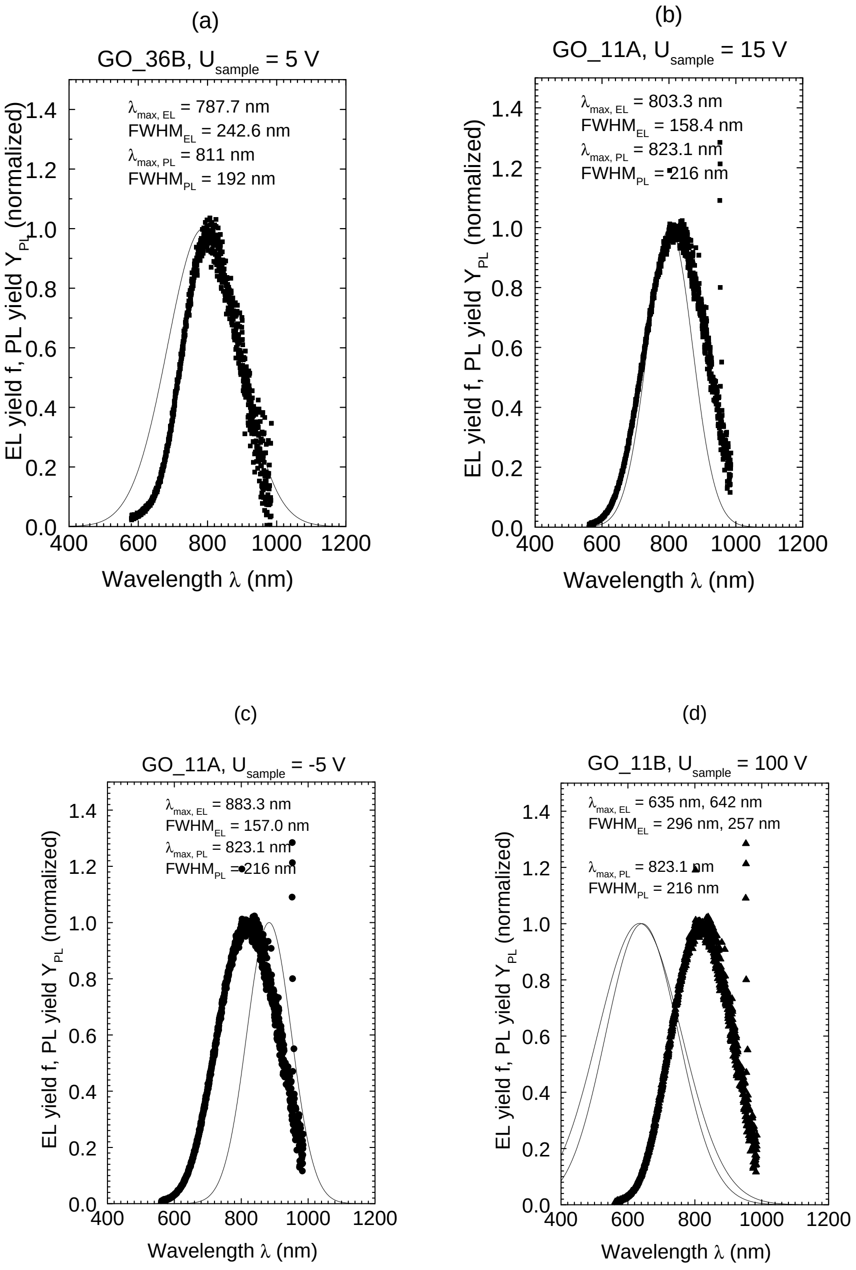

Figure 82: Spectral EL yields (solid lines) extracted from cut-off yield analysis and PL yields (symbols). Bias-voltages U_{sample} are noted on top of the graphs.

In order to compare the spectral EL measurements, all results are shown in one graph (Fig. 83). In Figs. 81 (a), (b) (c) the quantity $Y_{c,EL}(\lambda_c)$ has been fitted with the function h_1, whereas in Fig. 81 (d) the quotient $Y_{c,EL}(\lambda_c)/I_{sample}$ was fitted. To compare the absolute values of EL yield, the estimated EL yields f have been divided by I_{sample} for the measurements shown in Figs. 81 (a), (b) (c). Thus the unit of the estimated EL yield f becomes nm^{-1} for all measurements. The sample currents were $I_{sample} = (1.00 \pm 0.03) \times 10^{-4}$ A (GO_36B), $(1.8 \pm 0.1) \times 10^{-7}$ A (GO_11A, $+15$ V), $(1.7 \pm 0.1) \times 10^{-8}$ A (GO_11A,-5 V). Remarkably in Fig. 83 the maximal EL yield values coincide within approximately 1 order of magnitude, except for the measurement on sample GO_11A at bias $I_{sample} = -5$ V, which shows a maximum about a factor 10^4 larger. Furthermore the EL yields are similar for all samples in forward bias in the high wavelength region ($\lambda > 800$ nm), whereas there are large differences for low wavelengths ($\lambda < 800$ nm).

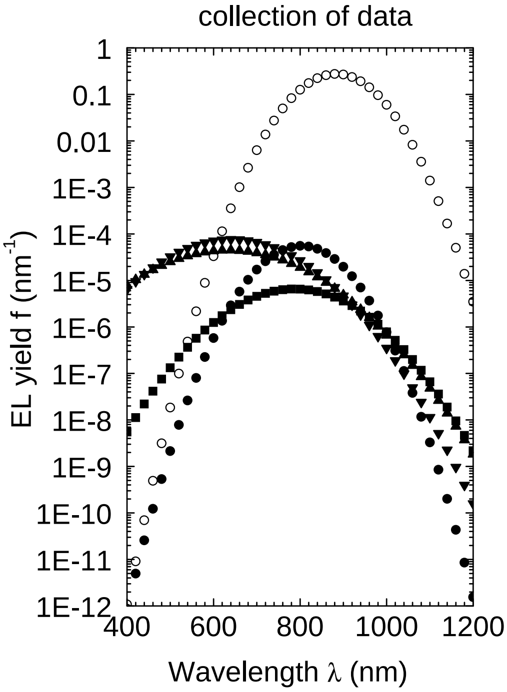

Figure 83: Spectral EL yields f for samples GO_36B (squares), GO_11A ($+15$ V solid circles, -5 V open circles), GO_11B (triangles).

Discussion

The correspondence between the EL and PL peak positions for samples GO_36B, GO_11A ($U_{sample} = +15$ V) (Tab. 19) is a hint, that the transitions, which generate the EL and PL are the similar. The similarity of PL and EL might be due to transitions in the quantum confined states of the Si-nc for both kinds of luminescence: During the process of EL electrons and holes tunnel from opposite sides of the structures through the SiO_2 barriers into the conduction band $E_{C,Si-nc}$ and the valence band $E_{V,Si-nc}$ of the Si-nc layer and recombine in the region, where they meet (Fig. 84). The main part of the carriers recombines non-radiatively *via* inter-band

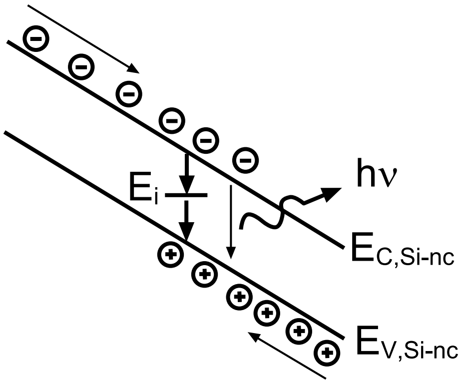

Figure 84: Electrons and holes recombine in the Si-nc layer *via* inter-band states E_i or radiatively.

states E_i, only a small fraction undergoes band-band recombination and generates EL.

For sample GO_36B the band diagrams in Fig. 66 can explain the mechanism. These band diagrams cannot be applied to sample GO_11A, because *no* SiO_2 has been deposited between the Si-nc and the Pt contact for this sample. Fig. 85 shows similar band diagrams *without* SiO_2 layers. The DLs are now assumed to be at the Pt / Si-nc interface. Electrons can tunnel only with very low probability from the Pt into the conduction band of the Si-nc for forward bias and similarly holes can tunnel with very low probability from the Pt into the valence band of the Si-nc for reverse bias, due to the large tunnel distance in the Si-nc layer. If the bias voltage is sufficiently large, space charges could accumulate in the Si-nc layer, such that the voltage does not drop linearly in the Si-nc layer, but the way shown in Fig. 85 (c). This would enable electrons to tunnel from the Pt into the Si-nc layer and can explain the EL detected in forward bias for sample GO_11A.

For reverse bias EL was detected, which is red-shifted $\Delta\lambda_{max} \approx 60$ nm with respect to PL. Hence it is likely that the EL does not originate from band-band recombination in the Si-nc, but rather from a tunnelling transition through the DL between conduction band of the Si-nc and the Pt electrode. The expected photon energy $E_{EL,expected}$ will correspond to the difference of the energies of the conduction band $E_{C,Si\text{-}nc}$ in the Si-nc and the Pt Fermi-level $E_{F,Pt}$:

$$E_{EL,expected} = E_{C,Si\text{-}nc} - E_{F,Pt} = -3.90 \text{ eV} - (-5 \text{ eV}) = 1.1 \text{ eV}.$$

The measured EL, however, showed a peak wavelength $\lambda_{max,EL} = 883$ nm, which corresponds to an energy

$$E_{EL,meas} := \frac{1240 \text{ nm eV}}{\lambda_{max,EL}} = 1.40 \text{ eV}.$$

As the voltage drop in the DL is not known exactly and might be changed by the bias voltage, the the difference $E_{EL,meas} - E_{EL,expected} = 0.30$ eV can be attributed to this uncertainty. Furthermore we can calculate the voltage drop U_{DL} in the DL from the measured EL energy $E_{EL,meas}$ in the framework of this model: From

$$E_{EL} = (W_{Pt} - \chi_{Si\text{-}nc}) - eU_{DL}$$

follows

$$eU_{DL} = (W_{Pt} - \chi_{Si\text{-}nc}) - E_{EL,meas} = (5.5 - 3.75) \text{ eV} - 1.40 \text{ eV} = 0.35 \text{ eV}.$$

Fig. 85 (d) shows the band diagram obtained by assumption of $U_{DL} = 0.35$ V.

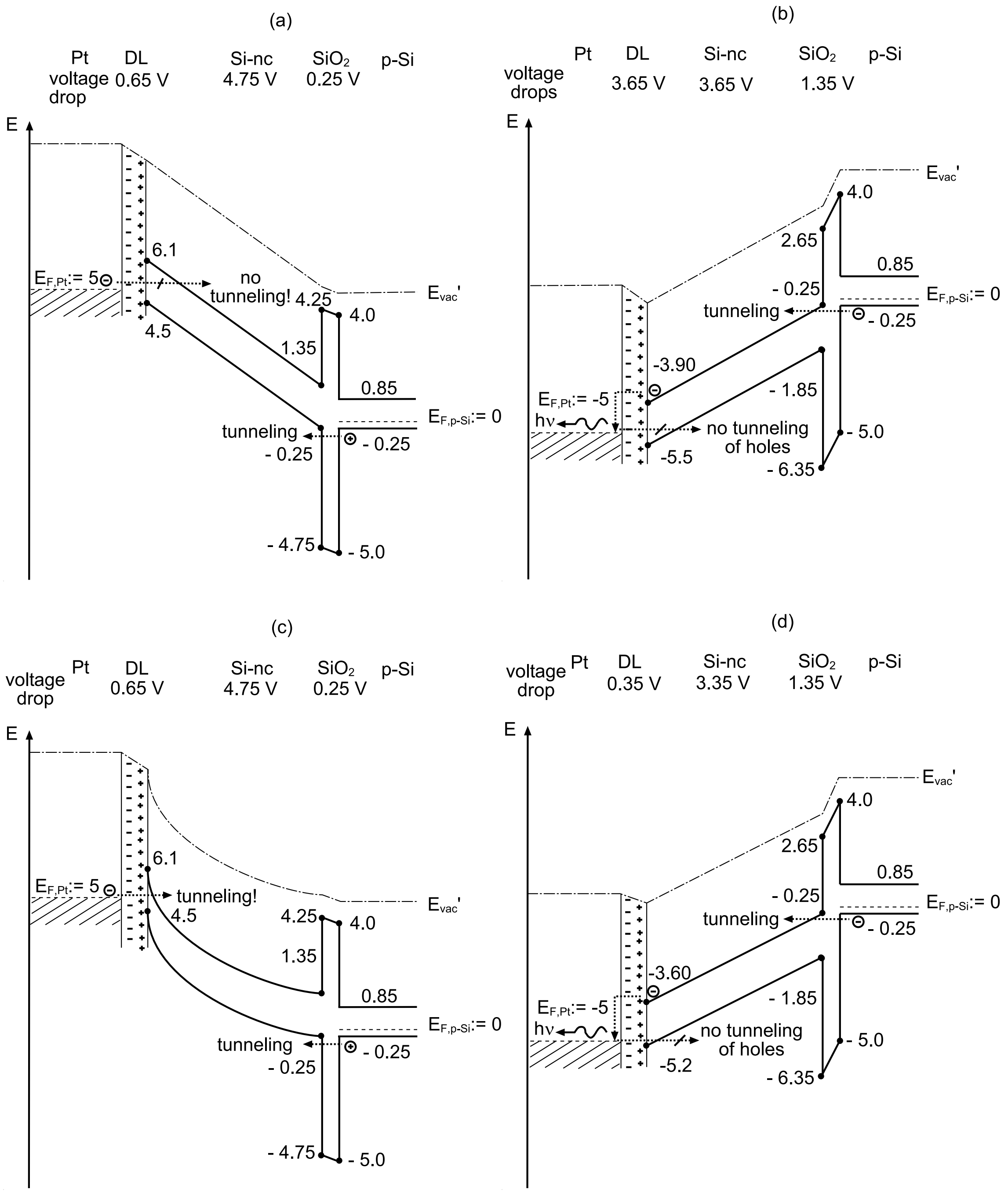

Figure 85: Band diagram for the sample without SiO_2 at Pt / Si-nc junction (GO_11A). (a) $U_{sample} = +5$ V, (b) $U_{sample} = -5$ V (c) $U_{sample} = +5$ V, hypothetical space charges in the Si-nc layer enable tunnelling of electrons into Si-nc layer, (d) $U_{sample} = -5$ V, assumption of smaller voltage drop $U_{DL} = 0.35$ V in DL according to experimental results.

The higher efficiency of this device in reverse bias can be explained, when electrons are the dominant current carriers. We assume, that holes do hardly tunnel from the Pt into the valence band of the Si-nc, and therefore almost solely electrons are the carriers of the current. Hence electrons in the Si-nc layer do rarely recombine with holes, because the hole concentration in the Si-nc layer valence band is similar to the one in thermal equilibrium. The efficiency being of the order 10^{-5} can be explained by predominant non-radiative recombination at the Si-nc / Pt interface.

The EL of sample GO_11B is blue-shifted 185 nm with respect to its PL. Therefore we conclude that the energy levels involved in the recombination process are not the same for the other samples. My hypothesis is, that the EL generated in sample GO_11B at 100 V forward bias originates from recombination in states connected to the SiO_2 layers or to the oxide shells of the Si-nc. According to [35] there are defects in SiO_2, which luminesce at wavelengths

$$\lambda_{max,PL}^{SiO2} \approx 600 \ldots 670 \text{ nm},$$

and the observed EL peak

$$\lambda_{max,EL}^{GO\_11B} = (638.5 \pm 4) \text{ nm}$$

for sample GO_11B matches well in this range. The defects are called non-bridging-oxygen-hole-centres (NBOHCs). The two most investigated NBOHCs consist of localized centres with a trapped hole on a Si-$O^{\bullet}$ complex or Si-$O^{\bullet} \cdots$ H-O complex and show transition energies $\Delta E_{NBOHC} = 1.9$ eV, $\Delta E_{NBOHC} = 2.0$ eV respectively [33].

I propose an EL model for sample GO_11B, where NBOHCs in a SiO_2 layer between two adjacent Si-nc in the Si-nc layer are luminescent centres with $\Delta E_{NBOHC} \approx 2.0$ eV. I assume that the upper level $E_{NBOHC,2}$ of the NBOHC is higher than the conduction band of the Si-nc and the NBOHC lower level $E_{NBOHC,1}$ is lower in energy than the valence band of the Si-nc (Fig. 86). Because the exact position of the NBOHC levels in the SiO_2 band gap is not known [33], I assume that they are symmetrically shifted 0.2 eV up and down with respect to the bands of the Si-nc with band gap $E_{g,Si-nc} = 1.6$ eV.

For zero bias voltage $U_{SiO2} = 0$ at the SiO_2 layer electrons and holes cannot be injected in the NBOHC levels. They just tunnel through the oxide. Only if the voltage drop $U_{SiO2} > 0.4$ eV, injection can occur *via* tunnelling (Fig. 86 (b)). If an electron and a hole is injected in the upper and lower level of a NBOHC, they can recombine and generate a photon, which is generation of EL. In principle this mechanism cannot only occur in the Si-nc oxide shell layers, but also in the "boundary SiO_2 layers" present at the ends of the Si-nc layer. It is even more likely that this is the dominant mechanism, because for reverse bias *no* EL was detected for sample GO_11B even for a voltage $U_{sample} = -100$ V. Because the above explained EL generation in the oxide shell layers of the Si-nc is symmetric with regard to the bias voltage, there has to be some other asymmetry which makes EL appear in forward bias and dissappear in reverse bias. In [20] a similar mechanism for the generation of EL in Si / SiO_2 layer structures has been proposed: EL is only generated in structures containing a c-Si / SiO_2 interface, a hint, that in our EL structure GO_11B the EL might rather be generated in the SiO_2 layer adjacent to the p-Si substrate than in the SiO_2 between the Si-nc cores.

The good coincidence of the scaled spectral EL yield (Fig. 83) for $\lambda > 800$ nm of all samples except GO_11A with $U_{sample} = -5$ V can be understood the way, that in *all* these samples EL emission takes place in the Si-nc, but for some samples additional EL is generated by recombination *via* states in the SiO_2. This interpretation also explains, why the full width of half maximum (FWHM) of the EL in the measurements of sample GO_11A is smaller than for the

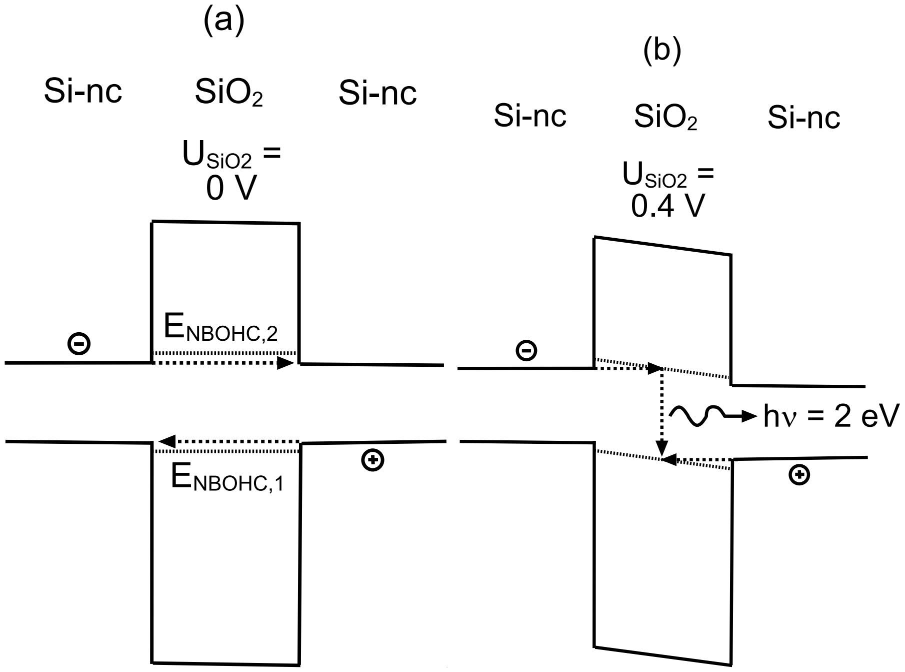

Figure 86: NBOHCs in SiO_2 generate EL with energy $h\nu = 2$ eV. (a) No EL without bias at the SiO_2. (b) EL, if the bias $U_{SiO2} > 0.4$ eV.

other samples: In sample GO_11A the SiO_2 layer between the Pt and the Si-nc is missing. (For samples GO_36B, GO_11B EL in this layer would contributes to the total EL , which effects apparently increased FWHMs. In detail the EL should consist here of two peaks.).

7.7 Outlook

A detailed band diagram model to explain the EL should include two more items, so far neglected.

1. The electrons in Pt and the holes in the valence band of p-Si are distributed according to some statistics (approximately Fermi-statistics).
2. The Si-nc layer, which has been treated effectively as *one* semiconductor, consists of many c-Si cores of Si-nc separated by their oxide shells.

These two items imply modifications to the so far assumed models and the importance of the induced effects shall be examined here

As a consequence of 1. electrons can also tunnel from the Pt into the conduction band of the Si-nc layer, when the energy of the Fermi-level in Pt is lower than the energy of the Si-nc conduction band edge (Fig. 87).). As the Fermi-distribution for electrons is

$$f(E) = \frac{1}{exp(\frac{E-E_F}{kT}) + 1},$$

where E is the electron energy, E_F the Fermi-level, k the Boltzmann-constant and T the temperature, the probability of a state $kT \approx 0.025$ eV (at RT) above the Fermi-level to be occupied by an electron is $(\exp(1)+1)^{-1} \approx 0.27$, which is rather high. A state 0.2 eV above the Fermi-level will by occupied with the probability $(\exp(8)+1)^{-1} \approx \exp(-8) \approx 3.4 \times 10^{-4}$. (Thus it

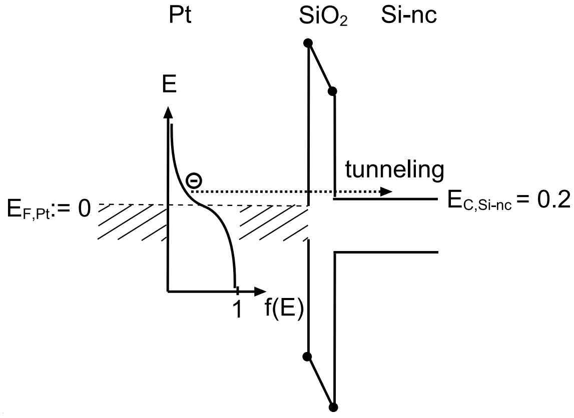

Figure 87: Thermally excited electrons in Pt tunnel through a barrier into the conduction band $E_{C,Si-nc}$ of the Si-nc. Inset shows Fermi-distribution $f(E)$.

is clear, that the Fermi-distribution shown in Fig. 87 is not scaled properly.) Hence if the Si-nc conduction band $E_{C,Si\text{-}nc}$is situated an energy ΔE above the Fermi-level $E_{F,Pt}$ of Pt, an amount of electrons corresponding to the fraction $\int_{E_{F,Pt}+\Delta E}^{\infty} f(E)dE$ of the electron density $D_{Pt}(E)$ of Pt in this energy range can tunnel into $E_{C,Si\text{-}nc}$. The same argumentation is true for holes, which tunnel from the valence band of the p-Si wafer into the valence band of the Si-nc. Theoretical calculations in Subsection 6.3.1 have shown, that the maximal tunnelling current from a semiconductor in thermal equilibrium in Boltzmann-approximation through a square barrier occurs at an energy $E_{max} \approx kT$, where zero energy is defined as the conduction band edge of the semiconductor. Thus the modifications to the above assumed model, implied by item 1, are expected to be not severe, because at RT $kT = 0.025$ eV, which is much smaller than the barrier heights of some eV. (The maximal tunnelling current from a metal through a square barrier should similarly occur at energies of the range of kT above the Fermi-level. The Fermi-distribution of the electrons in the metal can be approximated by a Boltzmann-distribution for energies sufficiently high above the Fermi-level.)

The second item implies a band structure, where the charge carriers have to tunnel through many SiO_2 oxide shells in the Si-nc layer. If we assume the transport of the carriers in the Si-nc cores to be ballistic, the bias voltage U_{sample} will drop in the Si-nc layer only at the oxide shells. The way, U_{sample} is distributed on the two outer SiO_2 layers and on the SiO_2 shell layers should be governed mainly by one demand: continuity of the sum of electron and hole current densities. This means, that the product of the tunnelling probability $P_{tunnel}(E)$ and the occupation density $f(E)D_{Pt}(E)$ is constant at every tunnelling barrier in regions, where transport is dominated by carriers of on kind:

$$P_{tunnel}(E) \cdot f(E)D_{Pt}(E) = const. \tag{69}$$

By E we denote the energy of the electrons in the initial state before tunnelling through the barrier. As the electrons do not all have the same energy in a state before the tunnelling, but there is a distribution in dependence on energy, only the integral over (69) will be constant.

The effects of the two items are illustrated in Fig. 88. Just as an example the Fermi-level $E_{F,Pt}$ has been assumed to have a 0.2 eV lower energy than the conduction band of the Si-nc, where the electrons tunnel. The same difference has been assumed for the valence band of the p-Si wafer and the valence band of the Si-nc, where the holes tunnel. A path *via* 10 Si-nc is assumed to connect the Pt contact with the p-Si wafer. The number 10 has only been chosen for convenience of drawing the band diagram. For a layer thickness $d_{Si\text{-}nc} = 100$ nma path *via* ≥ 20 Si-nc with diameter $D_{Si\text{-}nc} = 5$ nm would be present and for $d_{Si\text{-}nc} = 1000$ nm more than 200 Si-nc would be necessary. One also has to keep in mind that the real situation is much more complicated, because there is a network of interconnected Si-nc between the Pt and the p-Si. There are much more possibilities to go from the Pt contact to the p-Si wafer than *via* one path. To evaluate this complex model quantitatively is left out in this thesis. It lies out of the scope of an experimental PhD lifetime.

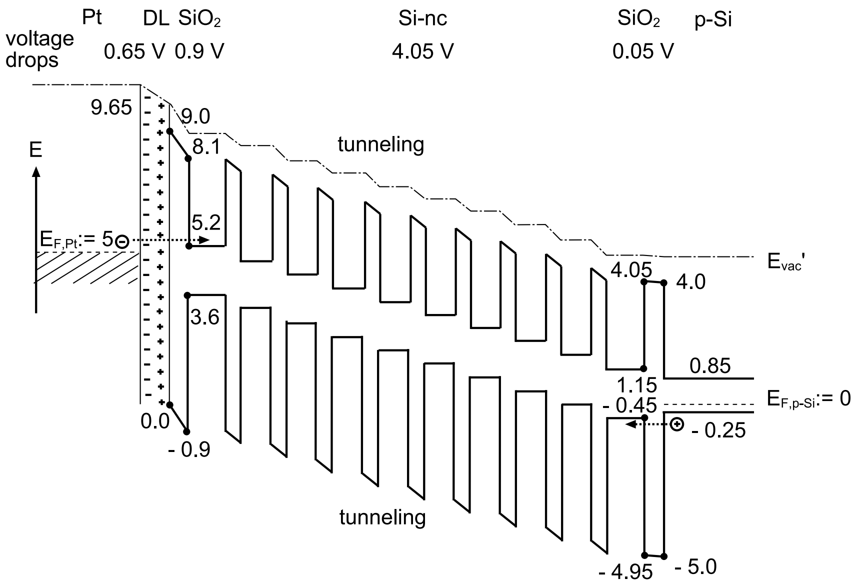

Figure 88: Sketch of detailed band diagram for EL structures with SiO_2 at the Pt / Si-nc junction in forward bias.

Another point is the low overall estimated EL efficiency. It is partly due to unoptimized EL structures, which could be improved e.g. by variation of the contact metal. Furthermore good transport and high PL yield seem to mutually exclude each other for standard layers including Si-nc [4]. But more inherently the low efficiency is caused by the indirect nature of the silicon band gap. The implicated large PL and EL lifetime effect cause that easily more than one electron-hole pair per Si-nc is excited, which results in non-radiative recombination of the more than 1 surplus pairs. It has been argued that as an effect of carrier confinement in the nm-range the indirect band gap of silicon can become partially direct. Actually the band gap of nano crystals still stays predominantly indirect, which has been affirmed by the long PL lifetimes determined for porous silicon and the increase of the lifetime for lower temperatures [2]. Hence to my opinion it will not be possible to built efficient or even fast responding light emitting electronically driven devices by Si-nc, unless an up to now unknown trick is invented.

7.8 Summary and Conclusions

Diode-like JU-curves of the EL structures can be qualitatively understood with help of a band diagram, including a dipole layer at the Pt / Si-nc interface. Low EL yield can be explained by non-radiative Shockley-Read-Hall-recombination *via* defects. Higher efficiency of EL for sample GO_11A is due to a dominating electron current in the Si-nc layer, which recombines at the Pt / Si-nc interface. El and PL agree fairly well for samples GO_36B, GO_11A in forward bias, which we interprete in the sense, that quantum confined states are the origin of luminescence in both cases.

The following open questions remain:

1. Which is the nature of the defects, proposed in subsection 7.6.2 as centres of non-radiative recombination?
2. Why is *no* EL detectable at reverse bias for the EL structures with SiO_2 at both sides of the Si-nc layer?
3. Is it true, that electrons tunnel in forward bias into the Si-nc, but holes do not in reverse bias for the sample, where no SiO_2 has been deposited between the Si-nc and the Pt contact (GO_11A)? In case it is true, which are the reasons in detail?

A The p-n junction

We will investigate, how the voltage in the space charge region (SCR) of a *p*-*n* junction is distributed on the *p*- and *n*-side. According to [44], ch. 2, Eq. (14) the total voltage drop in the junction U_{bi} is related to the width $x_p + x_n$ of the SCR by

$$U_{bi} = \frac{1}{2} E(0) \cdot (x_p + x_n), \tag{70}$$

where $E(0)$ is the maximum electric field exactly at the point of junction and x_p, x_n designate the extension of the SCR in the *p*- and *n*-side. Result (70) has been obtained in the frequently applied depletion approximation. The *built in voltage* U_{bi} is composed of two voltage drops U_p, U_n one in the *p*- and one in the *n*-side (Fig. 89):

$$U_{p/n} = \frac{1}{2} E(0) \cdot x_{p/n}.$$

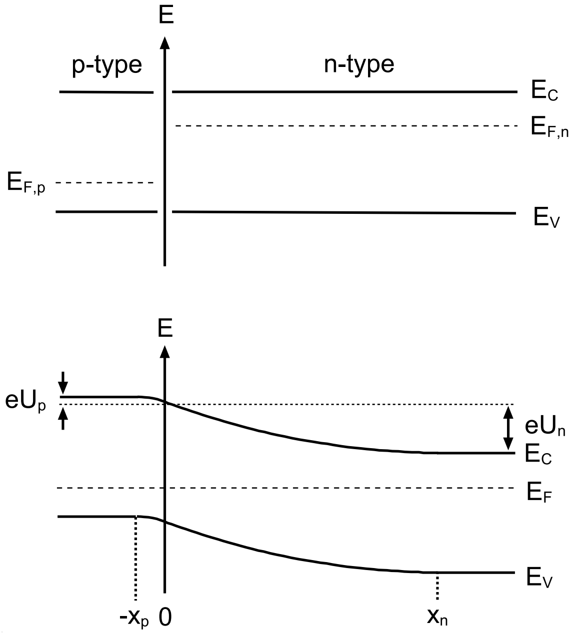

Figure 89: Discrete p-n junction with asymmetric doping, $N_A = 10 \cdot N_D$. Top: *p* and *n* semiconductors separated from each other. Bottom: *p*-*n* junction in thermal equilibrium.

The conduction band E_C and the valence band E_V are bended because of charges present in the SCR. In steady state without bias voltage the Fermi-level E_F is constant. The *built in* voltage corresponds to the difference of the Fermi-levels $E_{F,p}$, $E_{F,n}$ in the unjoined semiconductors: $U_{bi} = E_{F,n} - E_{F,p}$. From total charge neutrality in the device, $x_p N_A = x_n N_D$, follows that the ratio of the voltage drops equals the reciprocal of the ratio of the doping concentrations

$$\frac{U_p}{U_n} = \frac{x_p}{x_n} = \frac{N_D}{N_A}.$$

As $N_A = 10 \cdot N_D$ is assumed in Fig. 89, this effects $x_n = 10 \cdot x_p$ and $U_n = 10 \cdot U_p$. In the case $N_D \ll N_A$ the voltage drops almost entirely in the *n*-type side. Simultaneously the SCR in the *n*-type semiconductor grows larger and larger.

B Maths

Symbol	Name	definition / mathematical relation
j_l	spherical Bessel-function	$j_l(\xi) = (-\xi)^l(\frac{1}{\xi}\frac{\partial}{\partial\xi})^l \frac{sin(\xi)}{\xi}$
n_l	spherical Neumann-function	$n_l(\xi) = -(-\xi)^l(\frac{1}{\xi}\frac{\partial}{\partial\xi})^l \frac{cos(\xi)}{\xi}$
$h_l^{(1)}$	spherical Hankel-function of 1. kind	$h_l^{(1)} = j_l + in_l$
$\mathbf{L}$	angular momentum operator	$\mathbf{L} = \mathbf{r} \times \mathbf{p}$

The expressions for j_l, n_l are the Rayleigh formulas and $\mathbf{r}$, $\mathbf{p}$ denote the operators of place and momentum.

Laplace-operator in spherical coordinates

$$\Delta_{r\theta\phi} = \frac{\partial^2}{\partial r^2} + \frac{2}{r}\frac{\partial}{\partial r} - \frac{(\mathbf{L}/\hbar)^2}{r^2},$$

where

$$\mathbf{L}^2 = -\hbar^2(\frac{1}{sin\theta}\frac{\partial}{\partial\theta}sin\theta\frac{\partial}{\partial\theta} + \frac{1}{sin^2\theta}\frac{\partial^2}{\partial\phi^2}).$$

C Appendices in German

Lebenslauf

Geboren am 2. 6. 1973 in München.

Eltern: Jürgen Voigt, Prof. für Mathematik
Marianne Voigt, Diplom-Sozialpädagogin und Hausfrau

1980–1984	Grundschule in Ottobrunn (Landkreis München)
1984–1986	Gymnasium in Neubiberg (Landkreis München)
1986	Umzug nach Bad Zwischenahn
1986–1992	Liebfrauenschule in Oldenburg
Mai 1992	Abitur an der Liebfrauenschule
August 1992–Juni 1993	Zivildienst in der Stiftung Pfennigparade in München, einem Rehabilitationsheim für Behinderte
Oktober 1993–Februar 1997	**Studium der Physik in Göttingen**
19. 10. 1995	Vordiplom in Physik
März 1997–Juli 1997	**Erasmus-Auslandsaufenthalt an der Rijksuniversiteit Groningen**
Oktober 1997	**Wechsel an die Carl von Ossietzky Universität Oldenburg**
1. 11. 1997–31. 3. 1998	studentische Hilfskraft bei Prof. K. Floret zur Betreuung der Übungen zur Vorlesung “Analysis I”
1. 4. 1998–15. 8. 1998	studentische Hilfskraft bei Prof. G.H. Bauer zur Betreuung der Übungen zur Vorlesung “Physikalische und elektrotechnische Grundlagen für Studierende der Informatik”
September 98–Januar 99	Studienarbeit “Überlegungen und Demonstrationen zu Möglichkeiten des Schwebens von Körpern in elektromagnetischen Feldern” bei Prof. K. Hinsch
1. 4. 2000–15. 8. 2000	erneut studentische Hilfskraft wie im Jahr 1998
Juni 99–Juli 2000	Diplomarbeit “Hall-Effekt und Rekombination in mikrokristallinen Silizium-Germanium-Dünnschichten” bei Dr. T. Unold in Zusammenarbeit mit dem Forschungszentrum Jülich, Institut für Schicht- und Ionentechnik, Abteilung Photovoltaik
22. 8. 2000	Erlangung des Diploms im Studiengang Physik
1. 12. 2000–31. 3. 2005	Stelle eines wissenschaftlichen Mitarbeiters bei Prof. G. H. Bauer an der Universität Oldenburg mit der Möglichkeit zur Promotion
1. 4. 2005–31. 7. 2005	Lehrauftrag, Betreuung der Übungen zur Vorlesung “Thermodynamik” von Dr. R. Reuter
21. 10. 2005	Disputation

Zusammenfassung

Silizium-Nanokristalle (Si-nc) wurden durch laserinduzierte Pyrolyse von SiH_4 hergestellt und auf verschiedenen Substraten in Form von dünnen Schichten abgeschieden. An diesen porösen Schichten wurden das Schichtwachstum, die optischen Eigenschaften, Ladungstransport, Photolumineszenz (PL) und Elektrolumineszenz (EL) untersucht.

Ein Modell, das die Si-nc als Kugeln behandelt, die bei Berührung mit anderen Si-nc oder dem Substrat sofort haften bleiben, wurde entwickelt und in Form von Monte-Carlo-Computersimulationen implementiert. Aus den Simulationen ergab sich ein Wert $P(\infty) = 0.86$ für die Porosität der Schichten im Grenzfall für unendlich großes Volumen.

Der Ladungstransport während des Schichtwachstums konnte qualitativ durch perkolativen Transport erklärt werden, der einerseits nahe den Grenzschichten und andererseits im Volumen stattfindet. Der gemessene elektrische Leitwert der Si-nc-Schichten folgt in Abhängigkeit von der Si-nc Flächendichte einem Potenzgesetz mit dem Exponenten $\overline{B_{exp}} \approx 1.5$. Dieser Exponent wurde durch weitere Monte-Carlo-Simulationen, die auf dem oben erwähnten Modell basierten, hinreichend gut reproduziert.

Ein Modell, das von Tunnelprozessen der Ladungsträger durch die Oxidbarrieren von benachbarten Si-nc ausgeht, wurde benutzt, um gemessene Strom-Spannungs-Kennlinien von oxidierten Si-nc-Schichten zu beschreiben. Aus den Anpassungen der theoretisch hergeleiteten Strom-Spannungs-Abhängigkeit an die experimentellen Messdaten wurden Werte für die Anzahl der Barrieren zwischen den Kontakten auf der Probe ermittelt, die einen Faktor $1.5 \ldots 12$ größer waren als die Zahl der Si-nc, die auf eine Linie in kürzester Verbindung zwischen den Kontakten passen. Dieses Ergebnis kann durch die Existenz von gewundenen Perkolationspfaden erklärt werden. Bei Messungen des Ladungstransports wurden erhebliche Instabilitäten festgestellt, die ich hauptsächlich auf das riesigen Verhältnis der Oberflächen zum Volumen der Si-nc zurückführe. Dieses bedingt eine extrem starke Empfindlichkeit des Ladungstransports in den Schichten gegenüber Veränderungen der Zusammensetzung und Dichte der umgebenden Gase und Wasserdampf.

Aus der optischen Transmission der Schichten wurde deren Absorptionskoeffizient ausgewertet. Durch Annahme eines 1-Oszillator-Modells für den Realteil der ausgewerteten Brechungsindex-Kurven wurden optische Bandlücken $E_{g,opt} \approx E_0/2$ als die Hälfte der Resonanzenergie E_0 angenähert. Diese Werte stimmen gut mit den Bandlücken überein, die sich aus Messungen der PL ergaben.

Durch den Bau von Systemen mit spezieller Schichtenfolge, kristallines Silizium (p-Typ) / Si-nc / Metall, konnte Elektrolumineszenz erzeugt werden. Die Abhängigkeit der EL-Intensität vom elektrischen Strom konnte durch ein Modell reproduziert werden, das auf nichtstrahlender Shockley-Read-Hall-Rekombination in Konkurrenz zu strahlender Rekombination beruht. Bei den meisten Messungen stimmen die spektralen Verteilungen von EL und PL überein. Die EL wird bei diesen Messungen vermutlich durch Rekombination zwischen quanteneingeschränkten Zuständen erzeugt. Bei manchen Messungen ist die EL jedoch in Relation zur PL signifikant blauverschoben. Dies erkläre ich dadurch, das die Rekombination bei der EL über Zustände stattfindet, die mit Siliziumdioxid in Beziehung stehen, wohingegen die PL durch Übergänge zwischen quanteneingeschränkten Zuständen entsteht.

Danksagung

Gottfried Bauer, meinem Erstgutachter, danke ich für sein ausgeprägtes Talent, Leute für Physik zu begeistern. Er hat mich durch sein Beispiel zur Aktivität und Kreativität inspiriert. Ich bin überzeugt, mich durch seine Bemerkungen und Ansichten mehr vom “Haben” zum “Sein” entwickelt zu haben. Viele Ideen, wie die Messung der spektralen Verteilung der EL mit Filtern, wurden von ihm inspiriert. Womöglich werden andere oder ich einige der während meiner Zeit als Doktorand nicht verwirklichten Ideen - wie die EL-Anregung durch einen Elektronenstrahl anstelle eines Metallkontakts - noch umsetzen. Auch die Idee zu dem wunderschön suggestiven, näherungsweise richtigen Modell für die elektronische Bandstruktur von Si-nc, dargestellt in Abb. 11 stammte von ihm. Einige Male sah er Fehler in meinen Überlegungen, die ich übersehen hatte (z. B. bei den Integrationsgrenzen für die Berechnung des Tunnelstromes bei Annahme einer 3-dimensionalen Zustandsdichte). Danke auch für seine finanzielle Fürsorge. Dadurch hatte ich den Kopf frei für die faszinierende Welt der Physik. Überrascht wurde ich durch seine Wandlungsfähigkeit. Ich bin dankbar dafür, dass er mir am Ende konsequent, uneingeschränkt und kompromisslos Freiheit gewährte.

An Herrn Huisken schätze ich besonders seinen Blick für das Wesentliche. Er hat mir nachdrücklich geholfen, meine Arbeit zu strukturieren und hat dazu beigetragen, den Forschungsaktivitäten einen roten Faden zu geben. Auch ihm danke ich für finanzielle Unterstützung. Außerdem danke ich für seinen Einsatz, mit dem er mir bei Experimenten half, indem er etwa direkt im Labor kompetente Ratschläge gab, oder indirekt, z. B. indem er sich um die Verwirklichung von Verbesserungen an der Depositionsapparatur kümmerte.

Die lockere Arbeitsatmosphäre in der Gruppe GRECO war besonders angenehm. Thomas Unold danke ich für die Initiierung der Idee zu *in-situ* Leitfähigkeitsmessungen und für viele andere intuitiv richtungweisende Anregungen und Tipps. Wesentliche Anregungen und Hinweise zu Schwerpunkten der Arbeit stammen von Rudi Brüggemann. Ich danke ihm für grundlegende experimentelle und konzeptionelle Hinweise beim Artikelschreiben. Außerdem ist er ein lebendes Beispiel dafür, dass es nicht darum geht, in Kleinigkeiten Recht zu haben, die für das Vorankommen der Arbeit irrelevant sind, sondern dass es darum gehen muss, die Sache bestmöglich voran zu bringen. Er hat mir bei vielen Gelegenheiten weiterführende Literatur gezeigt. Außerdem vielen Dank für zahlreiches Korrekturlesen und wichtige wissenschaftliche Hinweise und Korrekturen. Bis zuletzt hat er immer wieder - auch auf eigene Anfrage - Kapitel korrigiert und dabei einige größere Unstimmigkeiten verhindert. Vielen Dank für das liebenswerte Engagement!

Saioa setzte Maßstäbe für die soziale außeruniversitäre Komponente der Arbeitsgruppe. Ihre Nachfragen, ob wir denn nicht Gruppentreffen machen wollen, führte dazu, dass wir viele sehr nette GRECO-Abende bei “internationalem Essen” erlebten. Ja, wie Einstein (oder auch andere) schon sagte(n), ist Leistung im wissenschaftlichen Bereich mehr als allgemein angenommen mit sozialen Verhalten und Ethik verbunden. (Dabei muss ich an das vorletzte Treffen denken, bei dem Oliver Kunz, Tim und ich ein bisschen aus Kants “Kritik der reinen Vernunft” gelesen haben, und Oliver mir zu dem Verständnis verhalf, warum das Buch “Kritik der reinen Vernunft” heißt: Weil man mit bloßer, reiner Vernunft zu solch genial abstrus widersprüchlichen Schlussfolgerungen gelangt, wie sie in den Antinomien zu lesen sind.) Saioa hat mir außerdem durch Korrekturlesen mehrerer Kapitel geholfen. Max war eine auffrischende Erinnerung an meine bayerische Heimat, gab mir Computertipps und überließ mir netterweise ein Programm zur Auswertung des Fortgeschrittenenpraktikumversuchs. Nacera danke ich vielmals für ihre sehr nützliche und förderliche Hilfe bei Ermittlung des Absorptionskoeffizienten aus Messungen der optischen Transmission. Sie vermittelte mir ihre Prozedur zur Bestimmung des Absorptionskoeffizienten über eine Extrapolation des Brechungsindexrealteils. Sie war eine nette Mitbewohnerin unserer Uni-Büro-WG. Karsten Bothe danke ich für das Aufwachsen eines Tunnel-Oxids auf c-Si-*wafer* und deren Bereitstellung und Peter Reinig für die Herstellung von TCO-Substraten und das Senden von Infos dazu. Richard danke ich für Computertipps und das Schreiben des ersten Programms zu EL Messung. Ich danke Quasi-GRECO Tharanga Jinasundera für wunderbare Freundschaft und “FBI-Hilfe” (“How many pages have you written today, Felix?”), meine Doktorarbeit fertig zu schreiben. Er hatte DIE relevante Idee, die dazu führte, dass das Shockley-Read-Hall-Computerprogramm sich weiter entwickelte, das in numerischen Problemen stecken geblieben war. Dieses Programm berechnet die Besetzungsdichten in einem Halbleiter mit Defekt-Niveaus im stationären Zustand in Abhängigkeit von der optischen Elektronen-Loch-Generation und wurde in der Dissertation im Kapitel “Electroluminescence” zur Interpretation von Messergebnissen verwendet. Dank auch herzlich an ihn und Levent Gütay, dass sie ein Graphical User Interface (GUI) für dieses Programm implementiert haben. Levent danke ich außerdem ganz herzlich für viele Spaßigkeiten, Hilfen zu Entscheidungsselbsthilfen und unknackbare Koans. Und Peter Pargmann sei 1000 Dank gesagt für viele unentbehrliche Hilfeleistungen und Aufmunterungen!

Stefan Bleil sei Dank für viele kompetente Hinweise zu erfolgreichen Rettungsaktionen des Linux-Systems, das ich benutzte. Dirk Otteken danke ich für mehrere großzügige Leihgaben und intelligente Hinweise zu experimentellen Fragen.

Den Kolleginnen und Kollegen Felice Friedrich und Christoph Böhme vom HMI danke ich für Herstellung von interdigitalen Kontakten.

Malte danke ich für sehr gute Freundschaft, viele spannende Diskussionen und seine Idee den Farbfüll-Algorithmus für die Monte-Carlo-Simulationen zu verwenden.

Prof. Wittstock danke ich für die Möglichkeit, AFM-Messungen in seiner Arbeitsgruppe durchzuführen, und Ernie Schneider-Hassel für große Hilfeleistungen, Freundlichkeit und fruchtbare Diskussionen darüber, wie man AFM-Messungen macht. In Erinnerung bleiben wird mir ihr Ausspruch “Probieren geht über studieren” ...

Es folgen die Namen von Personen, denen ich außerdem Dank aussprechen will: Leonid Govor, Marco Munzel, Ingo Riedel, Jens, Martin, Dana, Achim Kittel, Vladimir Dyakonov, Verena, der EHF allgemein. Gilles, Alban, Gael, Sergej, Herrn Stieler, Olivier Guillois, Olivier Debieu, Fabrice Gourbilleau, Frederic Houze, Jean-Paul Kleider, Christophe Longeau, Marie, Ouafa, Jose ... Martin Holthaus.

Franz Bögershausen danke ich für Kraft spendende, aufbauende, die Sicht weitende Worte und für die Idee und Ermöglichung, den Abschluss meiner Doktorarbeit im Gemeindesaal von St. Stephanus zu feiern. Auch vielen anderen Mitgliedern der Stephanus-Gemeinde danke ich für Unterstützung.

Zuguterletzt danke ich meiner Familie, Mutter, Vater, und meinen Brüdern Andreas und Michael für nachhaltigen Beistand. Andreas hat das Kapitel über Tunnelvorgänge in einer Rohfassung Korrektur gelesen und Michael hat mir Computertipps zu Netzwerkalgorithmen und zur Programmiersprache C^{++} gegeben. Mein Vater stand mir mit mathematischen Tricks zur Lösung von Quantentöpfen mit geeignet gestalteten Potentialen zur Seite und meine Mutter hat mich rundum liebevoll unterstützt.

D Videos supplement

Attached to the back cover of the paper version of this PhD thesis is a CD inlay. The supplied CD on one hand contains a file named ”voiopt06.pdf”, which is an electronic version of this thesis. Furthermore there are located 3 videos in an extra folder. These videos exemplarily show runs of the computer simulations described in Chapters 5 and 6 of the thesis. (Videos are more suitable to illustrate the ideas of the simulations than the final screenshots, which are presented as figures in the above mentioned Chapters of this thesis.) The files and the purposes of the simulations, which the videos have been generated from, are described in the following table:

Filename	Purpose
por.avi	Simulation for calculation of porosity (see Chapter 5).
cont.avi	First contact simulation (see Section 6.2.4).
connect.avi	Simulation of connections (see Section 6.2.4).

The electronic version of this PhD thesis and the videos can also be downloaded from
”http://docserver.bis.uni-oldenburg.de/publikationen/dissertation/fak05.html”.

References

[1] D. Amans, S. Callard, A. Gagnaire, J. Joseph, G. Ledoux, F. Huisken, J. Appl. Phys. **93** (2003) 4173.

[2] D. Amans, O. Guillois, G. Ledoux, D. Porterat, C. Reynaud, J. Appl. Phys. **91** (2002) 5334.

[3] D. E. Aspnes, A. A. Studna, Phys. Rev. B **27** (1983) 985.

[4] I. Balberg, E. Savir, J. Jedrzejewski, J. Non-Cryst. Solids **338-340** (2004) 102.

[5] L. Banyai, S. W. Koch, *Semiconductor quantum dots* (World Scientific Publishing Co., Singapore, 1993).

[6] X. Brokmann, L. Coolen, M. Dahan, J. P. Hermier, Phys. Rev. Lett. **93** (2004) 107403.

[7] D. A. G. Bruggeman, Annanlen der Physik **24** (1935) 636.

[8] R. Brüggemann, *private communication* (2003).

[9] M. Büttiker, Y. Imry, R. Landauer, S. Pinhas, Phys. Rev. B **31** (1985) 6207.

[10] C. Delerue, G. Allan, M. Lannoo, Phys. Rev. B **48** (1993) 11024.

[11] A. L. Efros, A. L. Efros, Sov. Phys. Semicond. **16** (1982) 772.

[12] M. Ehbrecht, F. Huisken, Phys. Rev. B **59** (1999) 2975.

[13] R. P. Feynman, *There's Plenty of Room at the Bottom, www.zyvex.com/nanotech/feynman.html* (1959).

[14] A. T. Fiory, N. M. Ravindra, Journal of Electronic Materials **32** (2003) 1043.

[15] A. Fontcuberta, P. Roca, C. Clerc, Phys. Rev. B **69** (2004) 125307.

[16] M. A. Green, J. Appl. Phys. **67** (1990) 2944.

[17] M. A. Green, *Silicon solar cells; advanced principles & practice* (Centre for Photovoltaic Devices and Systems, University of New South Wales, Sydney, 1995).

[18] O. Guillois, N. Herlin-Boime, C. Reynaud, G. Ledoux, F. Huisken, J. Appl. Phys. **95** (2004) 3677.

[19] Hackel, *Transport und Injektion von Ladungsträgern in MOS-Strukturen mit der Monte-Carlo Methode, www.iue.tuwien.ac.at/phd/hackel/node40.html* (Institut für Mikroelektronik, TU Wien, 1995).

[20] L. Heikkilä, T. Kuusela, H.-P. Hedman, J. Appl. Phys. **89** (2001) 2179.

[21] S.-T. Ho, Y.-H. Chang, H.-N. Lin, J. Appl. Phys. **96** (2004) 3562.

[22] T. Jinasundera, L. Gütay, S. Tardon, F. Voigt, R. Brüggemann, G. H. Bauer, SRH, MATLAB computer program, to be made available under Gnu General Public Licence for download, not yet published (2005).

[23] M. J. Kelly, *Low-Dimensional Semiconductors* (Clarendon Press, Oxford, 1995).

[24] N. Koshida, H. Koyama, Appl. Phys. Lett. **60** (1992) 347.

[25] N. Lalic, J. Linnros, J. Lumin. **80** (1999) 263.

[26] G. Ledoux, O. Guillois, D. Porterat, C. Reynaud, F. Huisken, B. Kohn, V. Paillard, Phys. Rev. B **62** (2000) 15942.

[27] K. Levenberg, Quart. Appl. Math. **2** (1944) 164.

[28] E. Lotter, *Diplot 4.3, A program for evaluation of optical thin film spectra, www.erwin-lotter.de* (2005).

[29] O. Madelung(Ed.), *Semiconductors - Basic Data* (Springer, Berlin, 1996).

[30] D. Marquardt, SIAM J. Appl. Math. **11** (1963) 431.

[31] E. Marquez, A. M. B.-O. J. M. Gonzalez-Leal, R. Pricto-Alcon, A. Ledesma, R. Jimenez-Garay, I. Martil, Mater. Chem. Phys. **60** (1999) 231.

[32] J. P. McKelvey, *Solid state physics for engineering and materials science* (Krieger Publishing Company, Malabar (Florida), 1993).

[33] S. Munekuni, T. Yamanaka, Y. Shimogaichi, R. Tohmon, Y. Ohki, K. Nagasawa, Y. Hama, J. Appl. Phys. **68** (1990) 1212.

[34] L. Pavesi, L. D. Negro, C. Mazzoleni, G. Franzò, F. Priolo, Nature **408** (2000) 440.

[35] S. M. Prokes, J. Mater. Res. **11** (1996) 305.

[36] M. R. Reshotko, A. Sa’ar, I. Balberg, phys. stat. sol. (a) **197** (2003) 113.

[37] E. H. Rhoderick, R. H. Williams, *Metal-semiconductor contacts* (Clarendon Press, Oxford, 1988).

[38] E. F. Schubert, *www.ecse.rpi.edu/ schubert, Course-ECSE-6960, Ch17 Heterostructures.pdf.*

[39] J. G. Simmons, J. Appl. Phys. **34** (1963) 1793.

[40] J. Singh, *Semiconductor Devices: Basic Principles* (Wiley, New York, 2001).

[41] N. Souffi, *Effet de la metastabilite photoinduite sur les proprietes optoelectroniques du silicium amorphe hydrogene* (Universite des Sciences et de la Technologie d’Oran, Mohamed Boudiaf, 1999).

[42] O. Stenzel, *Das Duennschichtspektrum* (Akademie Verlag, Berlin, 1996).

[43] R. Swanepoel, J. Phys. E **12** (1983) 1214.

[44] S. M. Sze, *Physics of Semiconductor Devices* (Wiley, Murray Hill, 1981).

[45] K. Tanaka, Thin Solid Films **66** (1980) 271.

[46] J. Valenta, I. Pelant, K. Luterova, R. Tomasiunas, S. Cheylan, R. G. Elliman, J. Linnros, B. Hönerlage, Appl. Phys. Lett. **82** (2003) 955.

[47] F. Voigt, R. Brüggemann, T. Unold, F. Huisken, G. H. Bauer, Materials Science & Engineering C **25** (2005) 584.

[48] J. Voigt, *Thanks to my father for this wonderful hint!*

[49] S. H. Wemple, M. DiDomenico, Phys. Rev. B **3** (1971) 1338.

[50] C. M. Wolfe, N. Holonyak, G. E. Stillman, *Physical Properties of Semiconductors* (Prentice-Hall, Englewood Cliffs, 1989).